ICQNM 2012

The Sixth International Conference on Quantum, Nano and Micro Technologies

ISBN: 978-1-61208-214-1

August 19-24, 2012

Rome, Italy

ICQNM 2012 Editors

Victor Ovchinnikov, Aalto University, Finland

Petre Dini, Concordia University, Canada / China Space Agency Center - Beijing, China

ICQNM 2012

Foreword

The Sixth International Conference on Quantum, Nano and Micro Technologies [ICQNM 2012], held between August 19-24, 2012 in Rome, Italy, continued a series of events covering particularly promising theories and technologies. The conference covered fundamentals on designing, implementing, testing, validating and maintaining various kinds of materials, systems, techniques and mechanisms related to quantum-, nano- and micro-technologies.

Quantum technologies and nano technologies have a great potential to transform communications telecommunications infrastructure and communication protocols, and computers and networking devices. Nanotechnologies and micro-technologies already made their mark on smart materials, nano-medicine, nano-devices, molecular manufacturing, biotechnology, metrology, airspace.

The advancements in material science and computer science have allowed the building, launching and deploying of space exploration systems that continually do more and more as they become smaller and lighter. As an example, carbon nano-tubes have been created that are 250 times stronger than steel, 10 times lighter, and transparent. Similar advances are occurring in glass, plastics and concrete. Spacecraft are being launched, with hulls that are composed of carbon fibers, a light weight high strength material.

Electronic devices, medicine, environment, metrology, aerospace programs, clothes and materials, telecommunications, cryptography, semiconductors, manufacturing, and other domains are impacted by the progress on the areas mentioned above. Particularly, micro imaging, nano-medicine: (drug delivery; nano-particles i.e. viruses; proteins.), bio-nanostructures: (nano-tubes, nano-particles), microsystems, micro fluidics: (including nano-fluidics, modeling; fabrication and application), micro instrumentation / implantable microdevices (miniaturized bio-electronic systems, etc.) and micro sensors benefits from the progress on quantum, nano and micro technologies.

Developing nanoscale-manufactured robots presents fabrication and control challenges. The evolution of mechatronics system and robotic system requires advanced functions for control. Special methods and technologies have been developed to design, analyze, build, controls, and apply micro/nano-robotic systems for biotechnology, medical, information technology, materials, etc. A particular application of nano-robots would be in carrying out projects in hostile environments, utilizing local materials and local energy. Ultra-miniature robotic systems and nano-mechanical devices will be the biomolecular electro-mechanical hardware of future manufacturing and biomedical industry.

Nowadays, there are tremendous attempts to develop new bio-molecular machines, components that can be assembled in nano-devices. Bio-robotics entities are able to manipulate the nano-world components, convey information from the nano/nano to the nano/macro world and navigate at the nano-environment level. Additionally, they are able to self replicate, leading to the bio-robot factory. Protein-based nano-motors and nano-robots, as well as biomolecular components interfaces.

Quantum cryptography uses the uncertainty principle of quantum physics to provide a safe but public means for transmitting vital, secret information. A quantum public key distribution system depends on the uncertainty principle to ensure secrecy. Special protocols correlations and composability algorithms ensure similar functionality as in non-quantum systems. The security related tracks cover a series of events focusing on quantum security aspects. On the quantum protocol side, automated proofs of security and probabilistic model-checking methods have been suggested. Research teams focus on quantum key distribution and aspects related to key composability and correlations. Limitations are mainly related to physical devices and polarization control.

We take here the opportunity to warmly thank all the members of the ICQNM 2012 Technical Program Committee, as well as the numerous reviewers. The creation of such a high quality conference program would not have been possible without their involvement. We also kindly thank all the authors who dedicated much of their time and efforts to contribute to ICQNM 2012. We truly believe that, thanks to all these efforts, the final conference program consisted of top quality contributions.

Also, this event could not have been a reality without the support of many individuals, organizations, and sponsors. We are grateful to the members of the ICQNM 2012 organizing committee for their help in handling the logistics and for their work to make this professional meeting a success.

We hope that ICQNM 2012 was a successful international forum for the exchange of ideas and results between academia and industry and for the promotion of progress in quantum, nano and micro technologies.

We are convinced that the participants found the event useful and communications very open. We also hope the attendees enjoyed the historic charm Rome, Italy.

ICQNM 2012 Chairs:

Alireza Azarbadegan, University College London (UCL), UK
Daoyi Dong, University of New South Wales, Australia
Marco Genovese, Italian Metrological Institute (INRIM) -Torino, Italy
Masahito Hayashi, Tohoku University, Japan
Christian Kollmitzer, AIT Austrian Institute of Technology GmbH, Austria
Francois Le Gall, The University of Tokyo, Japan
Keiji Matsumoto, National Institute of Informatics, Japan
Victor Ovchinnikov, Aalto University, Finland
Vladimir Privman, Clarkson University - Potsdam, USA
Wen-Ran Zhang, Georgia Southern University, USA

ICQNM 2012

Committee

ICQNM Advisory Chairs

Vladimir Privman, Clarkson University - Potsdam, USA
Christian Kollmitzer, AIT Austrian Institute of Technology GmbH, Austria
Wen-Ran Zhang, Georgia Southern University, USA
Victor Ovchinnikov, Aalto University, Finland

ICQNM 2012 Research/Industry Chairs

Marco Genovese, Italian Metrological Institute (INRIM) -Torino, Italy
Keiji Matsumoto, National Institute of Informatics, Japan

ICQNM 2012 Special Area Chairs

QSEC
Masahito Hayashi, Tohoku University, Japan

Fluidics
Alireza Azarbadegan, University College London (UCL), UK

Quantum algorithms and quantum complexity
Francois Le Gall, The University of Tokyo, Japan

Quatum control
Daoyi Dong, University of New South Wales, Australia

ICQNM 2012 Technical Program Committee

Gerardo Adesso, Quantum Theory Group/Università di Salerno, Italy
Irina Buyanova, Linkoping University, Sweden
Weimin M. Chen, Linköping University, Sweden
Taksu Cheon, Kochi University of Technology - Tosa Yamada, Japan
Mihaela Corneanu, Banat's University of Agricultural Sciences and Veterinary Medicine, Romania
Sorin Cotofana, TU Delft, The Netherlands
Sao-Ming Fei, Capital Normal University - Beijing, China
Akihiko Fujiwara, Japan Synchrotron Radiation Research Institute - Hyogo, Japan
Juan Carlos García-Escartín, Universidad de Valladolid, Spain
Yuval Gefen, The Weizmann Institute of Science, Israel
Marco Genovese, Italian Metrological Institute (INRIM) -Torino, Italy
Masahito Hayashi, Nagoya University, Japan
Hoshang Heydari, Stockholm University, Sweden

Copyright Information

For your reference, this is the text governing the copyright release for material published by IARIA.

The copyright release is a transfer of publication rights, which allows IARIA and its partners to drive the dissemination of the published material. This allows IARIA to give articles increased visibility via distribution, inclusion in libraries, and arrangements for submission to indexes.

I, the undersigned, declare that the article is original, and that I represent the authors of this article in the copyright release matters. If this work has been done as work-for-hire, I have obtained all necessary clearances to execute a copyright release. I hereby irrevocably transfer exclusive copyright for this material to IARIA. I give IARIA permission or reproduce the work in any media format such as, but not limited to, print, digital, or electronic. I give IARIA permission to distribute the materials without restriction to any institutions or individuals. I give IARIA permission to submit the work for inclusion in article repositories as IARIA sees fit.

I, the undersigned, declare that to the best of my knowledge, the article is does not contain libelous or otherwise unlawful contents or invading the right of privacy or infringing on a proprietary right.

Following the copyright release, any circulated version of the article must bear the copyright notice and any header and footer information that IARIA applies to the published article.

IARIA grants royalty-free permission to the authors to disseminate the work, under the above provisions, for any academic, commercial, or industrial use. IARIA grants royalty-free permission to any individuals or institutions to make the article available electronically, online, or in print.

IARIA acknowledges that rights to any algorithm, process, procedure, apparatus, or articles of manufacture remain with the authors and their employers.

I, the undersigned, understand that IARIA will not be liable, in contract, tort (including, without limitation, negligence), pre-contract or other representations (other than fraudulent misrepresentations) or otherwise in connection with the publication of my work.

Exception to the above is made for work-for-hire performed while employed by the government. In that case, copyright to the material remains with the said government. The rightful owners (authors and government entity) grant unlimited and unrestricted permission to IARIA, IARIA's contractors, and IARIA's partners to further distribute the work.

Table of Contents

Microfluidic Cell Trapping Device Based on Standard PCB Technology

Nuria-Berenice Palacios-Aguilera, Ting Zhou, Jeroen Bastemeijer, Jeff Mollinger, Andre Bossche
Electronic Instrumentation Laboratory, Delft University of Technology
Mekelweg 4, 2628CD Delft, the Netherlands
n.b.palaciosaguilera@tudelft.nl, 54zhouting@gmail.com, j.bastemeijer@tudelft.nl, j.r.mollinger@tudelft.nl, a.bossche@tudelft.nl

***Abstract*—Nowadays, the methods used to determine cell concentration either count the cells per volume or measure the cells weight per volume. This paper presents the design, fabrication and measurement of a microfluidic cell trapping device envisaged for cell concentration measurements. The work presented here focuses mainly in the fabrication of the device. Measurements are made to validate the fabricated device. The device separates different size particles by using dielectrophoresis. Horizontal as well as vertical electric fields can be used to trap the particles by controlling the amplitude and frequency of AC voltage signals. The device presented here is fabricated using low-cost and low-temperature technologies.**

Keywords-dielectrophoresis; cell trapping; microfluidic;, vertical electric field; PCB

I. INTRODUCTION

Cell concentration is of high importance to medicine and food industry. In the case of medicine, measuring cell concentration is relevant for medical diagnosis; for food industry, it is useful for monitoring the concentration of yeast cells in food production.

Nowadays, the methods used to determine cell concentration either count the cells per volume or measure the weight of cells per volume. Those methods consume time and resources. The cell trapping device presented here is envisaged for cell concentration determination.

This paper presents the design, fabrication and measurements of a low-cost cell trapping microfluidic device. The design feasibility of the device was tested using COMSOL; however, this is not part of this work. Special attention is given to the fabrication process/method of the device since it uses other technologies than silicon and glass. The fabrication of the device is based on a standard PCB (Printed Circuit Board) and the use of SU-8 photoresist, making the device fabrication a low-temperature process. The PCB offers mechanical stability to the device.

An innovative fabrication method is presented making use of an ITO (Indium Tin oxide) glass slide to close the channel. The ITO glass offers optical transparency and the possibility to apply vertical electric fields in the channel.

Since different size cells respond in a different way when inhomogeneous electric fields are present, the dielectrophoretic technique is used to trap and release different size cells. Measurements are performed to validate the fabricated device and therefore the study of the associated models with the control of the particles' position with the use of an electric field is not part of this work.

Furthermore, the cell trapping device in combination with the packaging technology presented in [1] can be used for fast prototyping of low-cost and low-temperature fabricated μTAS (Micro Total Analysis Systems).

The packaging technology presented in [1] consists of inlaying an either fluidic or electronic chip in a PCB material and to build microfluidic channels on top of them. The electrical connections between the components are inkjet-printed.

In summary, the benefits of the device presented here with respect to commercially available devices are little consumption of sample volume, economic, high speed detection and flexibility of integration. Furthermore, it is small with a size of 70 mm x 70 mm x 1.6 mm.

The paper describes the relevant properties of the materials used for fabrication of the device. The fabrication process is detailed as well as the fabrication challenges and how to overcome them.

The experimental setup is explained and the results are presented. The paper finalizes presenting the conclusion and future work.

This paper does not include how to measure the cell concentration itself. Furthermore, analysis of the kinematic model of the particles as well as a deeper study of the associated control method to achieve very accurate positioning are not within the scope of this work.

II. MATERIALS

The materials used to fabricate the device are ITO glass, SU-8, and PCB material. ITO glass consists of a glass with a thin layer of indium oxide (In_2O_3) and tin oxide (SnO_2) on it. The two properties that make it very attractive for microfluidic devices are its electrical conductivity together with its optical transparency. Furthermore, it is biocompatible. Its main disadvantage is its high electrode impedance; 4 to 5 times higher than similar size gold electrodes [2]. The ITO glass used in this project was ordered from DELTA Technologies LTD., USA and Table I enlists its properties.

TABLE I. ITO GLASS PROPERTIES [3]

ITO glass properties	
Property	***Value***
Sheet resistance R_s	5-15 Ω

 ISBN: 978-1-61208-214-1

ITO glass properties	
Property	***Value***
Normal transmittance	>85 %
Nominal coating thickness	1200-1600 Å
Substrate thickness	0.5 mm
Substrate dimensions	25 mm x 50 mm x 0.5 mm

SU-8 is an epoxy-based negative photoresist used to pattern high aspect ratio structures [4]. This material is widely used as a structural material for microfluidics due to its physical properties as excellent chemical resistance, great biocompatibility and good adhesion to a wide range of materials. SU-8, when properly hard baked, is difficult to remove; moreover, if it is not completely exposed it tends to outgas. SU-8 2000 series offer low viscosity. SU-8 2002 is used to flatten the PCB surface and SU-8 2025 is used to build the microfluidic channel wall. Table II enlists the properties of SU-8 2002 and SU-8 2025.

TABLE II. PROPERTIES OF SU-8 2002 AND 2025 [5], [6]

Properties of SU-8 2002 and 2025		
Property	***Value (SU-8 2002)***	***Value (SU-8 2025)***
Viscosity	7.5 cSt	4500 cSt
Density	1.123 g/ml	1.219 g/ml
Thickness	~2-3 µm	~20-80 µm
Glass transition temperature Tg	210 ˚C	210 ˚C
Thermal conductivity	0.3 W/mK	0.3 W/mK

The PCB is used to mechanically support the electronic components, the microfluidic channel structure and to offer electrical connections. Compared with silicon, the PCB is much cheaper. Table III enlists relevant properties of FR-4 (flame retardant 4).

TABLE III. RELEVANT PROPERTIES OF FR-4 [7]

Relevant properties of FR-4	
Property	***Value***
Glass transition temperature Tg	135 ˚C
Thermal conductivity	0.255-0.290 W/mK
Substrate thickness	1.6 mm
Substrate dimensions	70 mm x 70 mm x 1.6 mm

The fabricated PCB has no solder mask and the electrical connections are gold plated to keep the biocompatibility of the device.

III. DEVICE DIMENSIONS

Figure 1 illustrates the cross-section of the electrodes area in the device, showing the dimensions of the microelectrodes as well as the microfluidic channel.

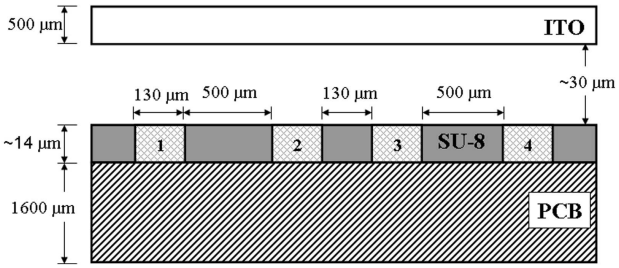

Figure 1. Dimensions of the microfluidic device. Cross-section of the electrodes area.

The PCB used is a 7 cm x 7 cm FR-4 PCB. Four electrodes and two holes for fluidic connections are pre-fabricated in the PCB.

The four electrodes have the same dimensions, 130 µm width and 1000 µm length. The distances between each couple of electrodes are 500 µm between electrodes 1 and 2, 130 µm between electrodes 2 and 3, and 500 µm between electrodes 3 and 4. The radius of the inlet and outlet holes is 400 µm. The microchannel length is 30 mm and the width of the channel is 1 mm. The depth of channel is approximately 30 µm.

IV. FABRICATION

The fabrication of the devices is divided in two stages: the flattening of the PCB surface and the fabrication of the microfluidic channel.

Since the electrodes and other electrical connections are pre-fabricated in the PCB, using standard PCB fabrication procedures, the thickness of the tracks is around 13 µm. The ratio between the channel depth and the thickness of the electrodes is rounded to 2. The flow of the media in the channel would be distorted due to this surface profile thus the surface of the PCB has to be flattened before building the microfluidic channel.

Figure 2 shows the steps followed to flatten the PCB surface. The steps in Figure 2 are performed 6 times since the SU-8 2002 provides layers of 2-3 µm thick, depending on the spinning speed.

First, a plasma treatment is performed to improve the adhesion between the SU-8 and the PCB (a). SU-8 2002 is spun on the surface of the PCB (b), (c). The specimen is subject to a soft baking step at 90 ° C (d). The SU-8 is exposed (e) and a post exposure bake step is performed at 90 ºC (f). The photoresist is developed thus the SU-8 covering the electrodes and electrical connections area is removed (g). A hard baking step is performed at 120 °C. The cycle initiates again performing the plasma treatment to the new surface.

The cycle is performed 6 times in order to achieve an SU-8 layer of around 13 µm thick, achieving the same level between the new PCB surface and the electrodes.

Figure 3 shows the steps followed to fabricate the microfluidic channels without going into detail in the surface flattening process.

The PCB is cleaned with ethanol to remove dust, grease and other forms of contamination from the surface. To

remove the humidity adsorbed during storage, it is dehydrated for two hours at 120 ºC (b). Subsequently, an oxygen plasma treatment is performed to improve the wetability of the substrate and the surface of the PCB is flattened using SU-8 2002 (c). The walls of the microchannel are fabricated using SU-8 2025 (d). Silver ink is deposited in order to make the electrical connection from the ITO glass to the PCB (e). The channel is closed using ITO glass. The ITO glass is attached to the SU-8 channel structure using a non-conductive adhesive (NCA) (f) and the adhesive is cured at 80 ºC during 3 hours (g).

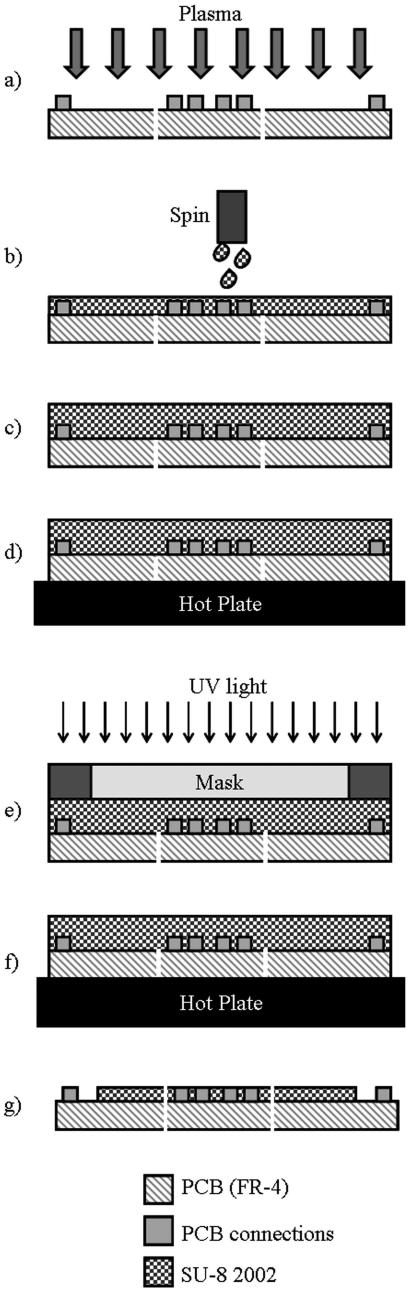

Figure 2. Process to flatten the PCB surface.

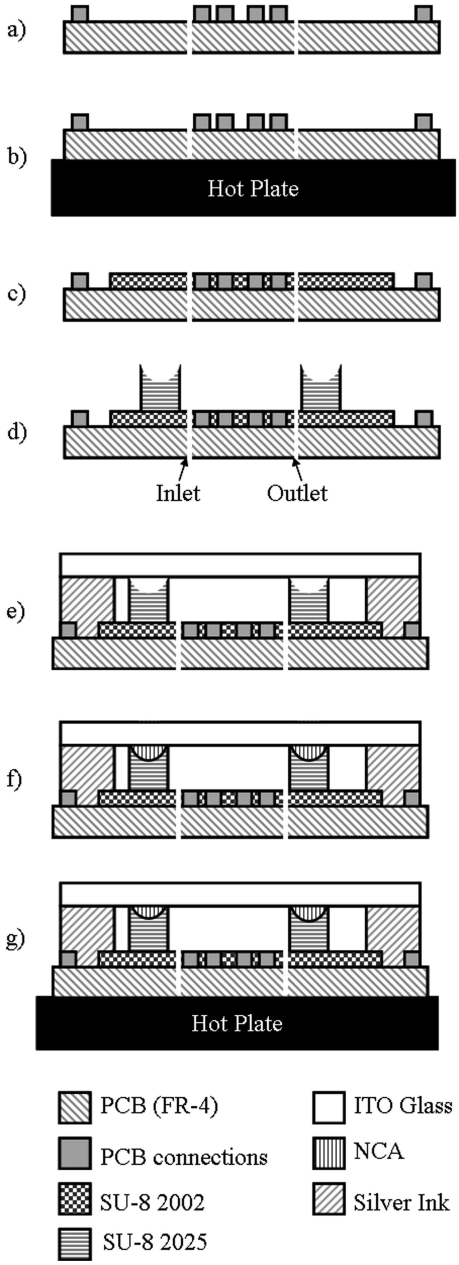

Figure 3. Flowchart to fabricate the microfluidic channels.

The fluidic connections to access the channel are made with a through vias during the fabrication of the PCB. The tubes to access the channel are press fit in the through vias on the back side of the device and glued. The device is ready to be used.

Figure 4 shows a fabricated device. The device is built on a prefabricated PCB including the electrodes.

 ISBN: 978-1-61208-214-1

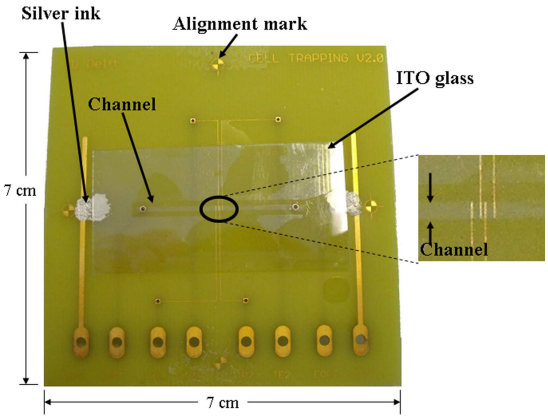

Figure 4. Fabricated device.

The electrical connection from the PCB to the ITO glass is made with silver ink. The fluidic connections for accessing the channel are made in the back side of the PCB.

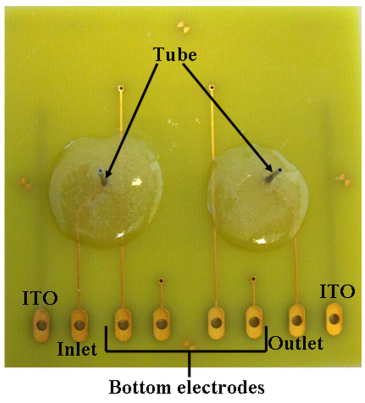

Figure 5. Fluidic connections for accesing the channel.

Figure 5 shows the back side of the PCB. The metal tubes for the inlet and the outlet holes are press fit in the holes and secured on the back side of the device with an epoxy adhesive.

V. FABRICATION CHALLENGES

During the fabrication of the device, there are two challenges to overcome.

The first one is to flatten the PCB surface. Figure 6 shows the PCB surface profile in the area of the electrodes measured with a Dektak profiler; the electrodes have a height of around 13 µm above the PCB surface.

The electrodes and electrical connections are fabricated with copper gold plated on the PCB. The surface is flattened with SU-8 in order to avoid contact of the media with copper and to avoid the flow of the media to be disturbed by the electrodes profile. This process is described in the previous section.

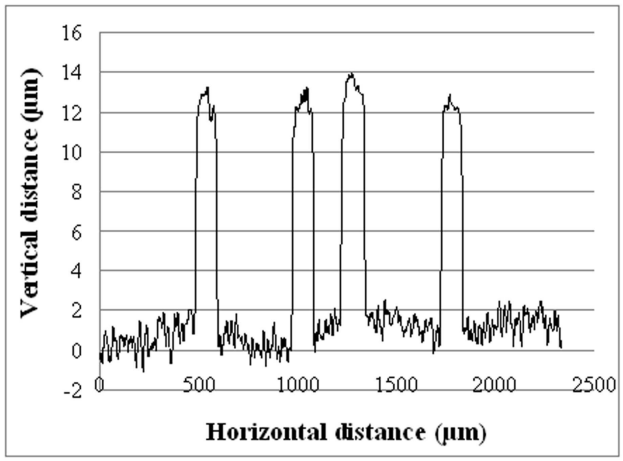

Figure 6. PCB surface profile in the area of the electrodes.

The second challenge to overcome is the way of sealing the channels. A low viscosity NCA is used for that purpose. Nevertheless, if the channel walls are fabricated with the SU-8 processing parameters recommended by the manufacturer, capillary forces make the NCA flow into the channel, blocking it. To overcome this, a channel on top of the channel walls is fabricated. Figure 7 shows (a) the cross-section of the wall of the channel when the recommended processing parameters are used and (b) the cross-section of the channel´s wall when different parameters are used for processing.

"The recommended processing parameters" refers to the way the temperature is taken from room temperature to the specified temperature, and vice versa, during the baking steps.

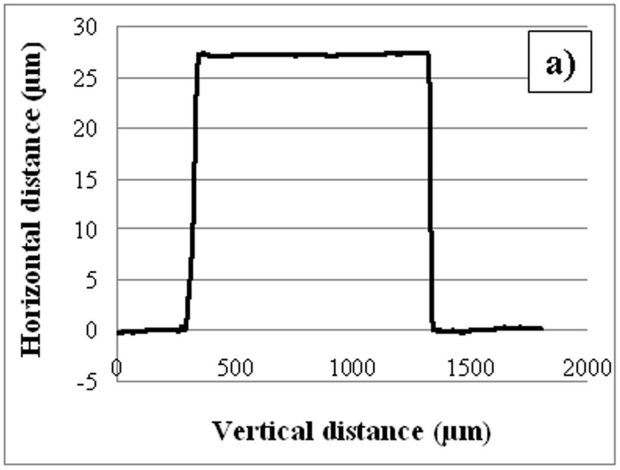

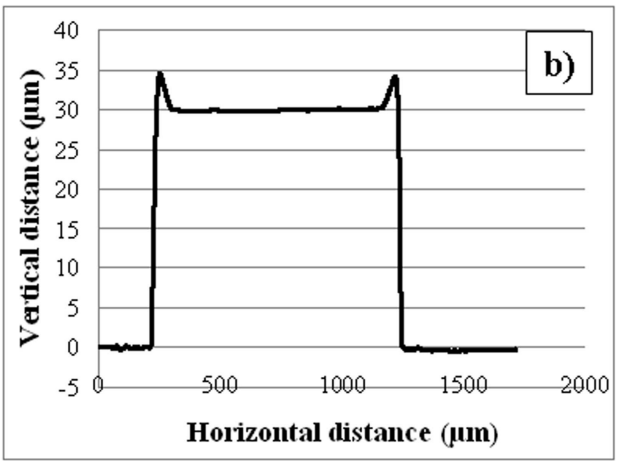

Figure 7. Cross-section of the wall of the channel when slow ramping of the temperatures during the baking steps is used (a) and when no ramping is used (b).

If the step from room temperature to baking temperature, and from baking temperature to room temperature is made in a fast way, stress in the resist will form such that two small walls are created in the top of the channel´s wall, creating a small channel on top of the walls of the channel; this small channel is used to flow the NCA avoiding it from coming into the fluidic channel. The NCA is cured and the channel is sealed. By sealing the channel in this way, no bonding equipment and heavy weights are necessary.

VI. EXPERIMENTS

The DEP (dielectrophoresis) force depends on the flow velocity, frequency and amplitude of the AC voltage signal, and particle size. Frequency and amplitude are isolated in this work to study their effects on trapping particles with a different size.

A syringe pump KdScientific model 200 is connected to the inlet tube of the microfluidic device to drive the flow of demi water with polystyrene particles by applying pressure difference between the inlet and the outlet.

An AC generator KROHN-HITE model 4300 is connected to the electrodes via the pads on the PCB to generate electric fields in the channel.

In order to test horizontal electric fields, a voltage difference is applied between adjacent electrodes, that is to say, between electrodes 1 and 2, 2 and 3, and 3 and 4.

To test vertical electric fields, a voltage difference is applied between the ITO glass and electrodes 2 and 4.

An oscilloscope HP54601B is used to check the applied AC signals.

The device is placed on the table of a microscope IX71 Olympus which has a low noise CCD camera ColorView Olympus to acquire images while the particles are being trapped. The software used to acquire the images is analySIS docu Olympus.

The trapped particles are plain microspheres of polystyrene from Phosphorex, Inc. with a mean diameter of 2, 6 and 10 µm.

VII. RESULTS

Table IV shows the results for trapping different size particles by regulating the frequency of the AC signal. The flow velocity used in this case is 0.1 µl/h.

TABLE IV. FREQUENCY REQUIRED FOR TRAPPING DIFFERENT SIZE PARTICLES WITH A HORIZONTAL ELECTRIC FIELD

Frequency required for trapping different size particles (horizontal electric field)		
Particle radius (µm)	***Voltage Frequency (KHz)***	***Voltage difference between electrodes (V)***
10	>140	26
6	>160	26
2	>1600	26

TABLE V. VOLTAGE AMPLITUDE REQUIRED FOR TRAPPING DIFFERENT SIZE PARTICLES WITH A HORIZONTAL ELECTRIC FIELD

Voltage amplitude required for trapping different size particles (horizontal electric field)		
Particle radius (µm)	***Voltage Frequency (MHz)***	***Voltage difference between electrodes (V)***
10	6	6.4
6	6	10.4
2	6	23.3

Table V shows the results for trapping different size particles by regulating the amplitude of the AC signal. The flow velocity in this case is 2 µl/h.

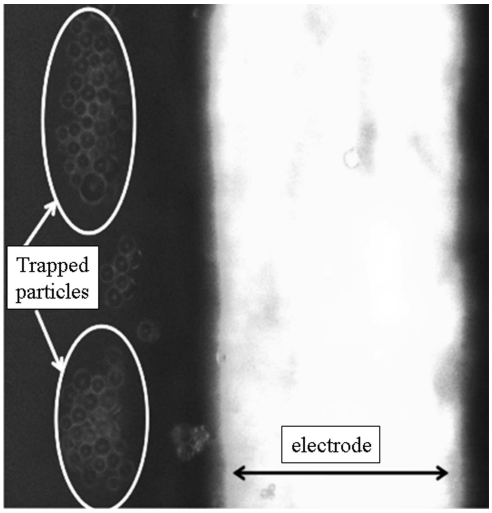

Figure 8. 10 µm and 6 µm particles trapped with a horizontal electric field at 400 KHz and a voltage difference between electrodes of 25 V.

Figure 8 shows trapped particles with a diameter of 10 µm and 6 µm. The frequency of the AC signal is 400 KHz and the voltage amplitude difference between the electrodes is 25 V. The flow velocity used is 0.1 µl/h. A horizontal electric field is used.

 ISBN: 978-1-61208-214-1

Figure 9 shows trapped particles with a diameter of 10 µm. The frequency of the AC signal is 160 KHz and the voltage amplitude difference between the electrodes is 7.5 V. The flow velocity used is 0.1 µl/h. A horizontal electric field is used.

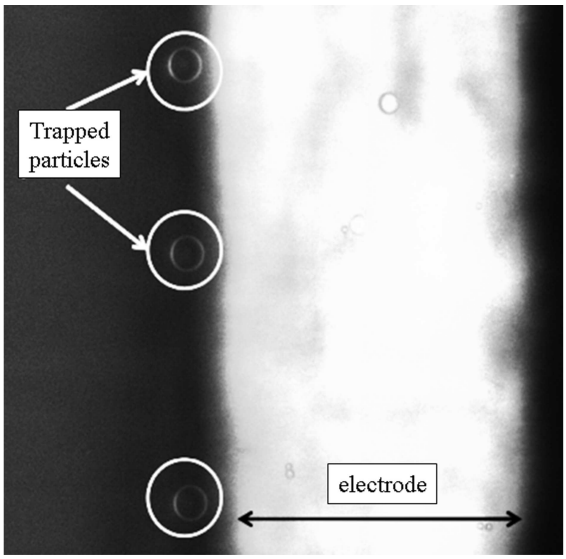

Figure 9. 10 µm particles trapped with a horizontal electric field at 160 KHz and a voltage difference between electrodes of 7.5 V.

Table VI shows the results for trapping different size particles using a vertical electric field. The frequency and amplitude of the AC signal are regulated. The flow velocity in this case is 1 µl/h.

TABLE VI. FREQUENCY AND VOLTAGE REQUIRED TO TRAP DIFFERENT SIZE PARTICLES WITH A VERTICAL ELECTRIC FIELD

Frequency and voltage amplitude required to trap different size particles (vertical electric field)		
Particle radius (µm)	***Voltage Frequency (KHz)***	***Voltage difference between ITO and electrodes 2, 4 (V)***
10	160	8.0
6	160	23.2
2	1200	23.2

The tables and figures show that the device is capable of trapping different size particles by controlling the frequency and the amplitude of the AC voltage signal using horizontal as well as vertical electric fields.

VIII. CONCLUSION AND FUTURE WORK

This work shows the fabrication of a dielectrophoretic microfluidic device for particle trapping and separation. Particles with different size can be separated by controlling the amplitude and frequency of AC voltage signals.

Furthermore, the device can trap particles using horizontal electric fields as well as vertical electric fields.

The device shows better performance in the vertical electric field than in the horizontal electric field; the frequencies required to trap particles of the same size are lower in the vertical direction than in the horizontal direction.

Moreover, the device is fabricated using low-cost and low-temperature technologies allowing fast prototyping and the integration of the device with the technology proposed in [1] to form µTAS.

As a part of future work, the cell concentration determination method is going to be developed enabling the measurements of cell concentration in blood for medical diagnosis and the monitoring of yeast cells' concentration in food production.

Furthermore, the analysis of the kinematic model of the particles and the deeper study of the associated control method to achieve very accurate positioning is also part of future work.

Moreover, future work can enlarge the field of application to the analysis of biological fluids by trapping living cells as different types of microorganisms or nuclei.

ACKNOWLEDGMENT

The authors thank DIMES (Delft Institute of Microsystems and Nanoelectronics) staff members for their valuable support.

REFERENCES

[1] N.B. Palacios-Aguilera, V.R.S.S. Mokkapati, J. Bastemeijer, J.R. Mollinger and A. Bossche, "Dry film resist microfluidic channels on printed circuit board and its application as fluidic interconnection for nanofluidic chips: fabrication challenges", International Conference on Quantum Nano and Micro Technologies (ICQNM 2011), Saint Laurent du Var, France, pp. 71-76, August 2011.

[2] R. Joshi, "Biosensors", Isha Books, Dehli, India, 2006.

[3] http://www.delta-technologies.com/Products.asp?c=1&s=23 retreived on 20 – Apr – 2012.

[4] J. Liu et al., "Process research of high aspect ratio microstructure using SU-8 resist", Microsystem Technologies, Vol. 10, Number 4, pp. 265–268, 2004.

[5] http://www.microchem.com/pdf/SU-82000DataSheet2000_5thru2015Ver4.pdf retreived on 20 – Apr – 2012.

[6] http://www.microchem.com/pdf/SU-82000DataSheet2025thru2075Ver4.pdf retreived on 20 – Apr – 2012.

[7] http://www.p-m-services.co.uk/fr4_data_sheet.htm retreived on 20 – Apr – 2012.

 ISBN: 978-1-61208-214-1

Integration of Nanostructured Multifunctional Surfaces into Analytical Chip

Andrej Oriňák, Renáta Oriňáková
University of P.J.Šafárik in Košice
Faculty of Sciences, Chemistry Institute, Department of Physical Chemistry
Moyzesova 11, 04154 Košice, Slovakia
andrej.orinak@upjs.sk, renata.orinakova@upjs.sk

Lenka Škantárová, Zuzana Nováková
Comenius University in Bratislava
Faculty of Science, Department of Analytical/Physical Chemistry
Mlynská Dolina CHII, Bratislava, Slovakia
lenka.skantarova@fns.uniba.sk

Jozef Radoňák
University of P.J.Šafárik in Košice
Faculty of Medicine, Trieda SNP 1
040 01 Košice, Slovakia
jozef.radonak@upjs.sk

***Abstract*—The nanostructures have currently received the great attractions for highly efficient and simultaneous analysis of a number of analytes. Outstanding optical property of noble metal nanostructures is a powerful phenomenon applied in chemical sensing. In this article, we introduce coupling of gold-capped silicone nanostructure prepared in fluidic channel with micro column high performance liquid chromatography. Micro column separation of the analytes was followed with an on-line deposition of effluent directly into a micro fluidic channel containing the deposited nanostructure. Effluent from micro column formed at gold-capped nanostructure a deposition trace, later analysed by surface-enhanced Raman spectro - scopy. The optical absorbance properties of nanostructure, the analytes in channel behavior as well optimization of chromatographic separation were investigated in this experiment. The surface enhancement factor 9.71 was obtained for rhodamine 6G in 30 μm wide fluidic channel. Optimum mobile phase composition was methanol/ water, 80/20, v/v. Detection of the analytes in 25 μm fluidic channel was affected with capillary forces during deposition process.**

Keywords-nanostructure; signal enhancement; SERS; integration; chip

I. INTRODUCTION

Micro fluidic systems are ideally suited for high-through -put chemical analysis since they offer high intensive analytical signal, consume minimum quantities of reagents, exhibit superior sensitivity and functionality compared to traditional micro-array techniques and can be integrated within complex work flows [1]. Detection of picomolar quantities of untagged oligonucleotides and polymerase chain reaction (PCR)-amplified desoxyribonucleic acid (DNA) samples with interferometric and localized surface plasmon resonance properties on gold nanostructure was demonstrated [2, 3]. An integrated analytical device composed of a microfluidic element and sensitive Raman spectrometer has been used with nanocolloid-based micro fluidic or metal nanostructure-embedded systems [4]. New methodology for enzyme assay using a sensitive and selective nanoparticle (AuNP)-enhanced time-of-flight secondary ion mass spectrometry (TOF SIMS) technique on self-assembled monolayers (SAMs) was reported [5]. Implementation of different functional nanostructures into fluidics was also documented [6-9]. The patterned micropads made of copper nanowires on silicon substrate showed the potential for application as chip to substrate interconnects [10]. Because metal deposited nanostructures usually do not provide any separation function this is in many cases substituted by chromatography or electrophoretic separation [11-12]. However, there are a lot of results documenting the analytes separation directly at a nanostructured surface [13-15]. The integration of fluidics and optics, as in flow-through nanohole arrays, has enabled increased transport of the analytes to sensing surfaces [16]. Uni-directional liquid spreading on asymmetric nanostructured surface [17] have enhanced surface wettability and enabled control of the liquid film thickness and final wetted shape. Liquid phase propagates in a single preferred direction and pins in all others. This is a key piece of chain coupled functional nanostructures in chip. As an example of multifunctional nanostructured surface can act silver nanorods array surface for on-a-chip separation and detection of chemical mixture by combining ultra – thin layer chromatography (UTLC) and surface-enhanced Raman spectroscopy (SERS). Limit of detection are between 10^{-5} – 10^{-6} M [18]. Another integration of the onedimensional nanostructures with the microsystems features with carbon nanotubes and nanowires [19].

In this article, we present the original results with functional gold – capped nanostructure that poses as a SERS nanodetector for the analytes former separated by micro column high performance liquid chromatogryphy (μHPLC). The separated analytes were deposited directly onto linearly moving micro fluidic channel with gold-capped nanostructure deposited inside. The separation conditions, a liquid phase behavior after micro fluidic channel dropping as

 ISBN: 978-1-61208-214-1

well SERS sensitivity were studied for future implementation in analytical microsystems or chips (with integrated multifunctional nanostructures; separation, unidirectional phase propagation, detection, etc.).

II. MATERIALS AND METHODS

A. Chemicals

All the chemicals used (acetonitrile, dioxane, methanol, rhodamine 6G (R6G) and rhodamine B (RB)) were purchased from Alfa Aesar GmbH (Germany). All of them were of an analytical grade of purity. The μHPLC mobile phases were mixed in the proportions: methanol: water / 80:20 (v/v); acetonitrile: water / 80:20 (v/v); dioxane: water/ 80:20 (v/v) and also filtered through 0.2μm filters to prevent obturation of a microcolumn. The structural formulas of both rhodamines are given at Figures 1 and 2.

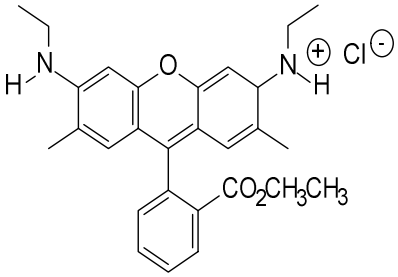

Figure 1. Structural formula of R6G, M.w. 479.01g/mol.

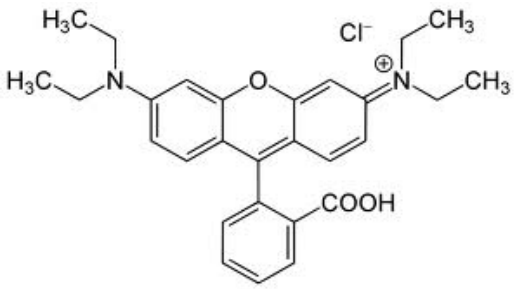

Figure 2. Structural formula of RB, M.w. = 479.21 g/mol.

B. Materials and methods

The black silicon nanostructure was prepared by advanced silicon etching (ASE) (STS MESC Multiplex), etching the plain silicon wafer with tiohexafluoride /oxygen plasma. The parameters of the etching gases and the conditions of plasma: SF_6 flow – 99 standard cubic centimeter per minute (sccm), O_2 flow – 90 sccm, coil power – 2800 W, platen power – 16 W, pressure process – 5.06Pa, pressure base – 12.53Pa, time – 4 minutes. After the etching process, the substrate was covered with the layer of noble metal (Au) by e-beam deposition process. Single side polished silicon wafers with diameter 100 mm and thickness 525 μm ± 25 μm [14].The different channels with integrated gold - capped nanostructures are given at Figure 3.

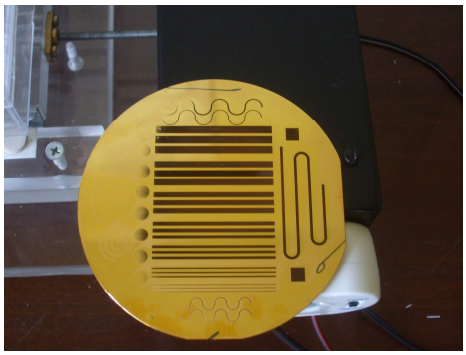

Figure 3. The microfluidic channels (different width) with implemented silicone gold - capped nanostructure inside.

In this experiment were used the micro channels 25 μm deep and 25 or 30 μm wide. Micro column high- performance liquid chromatography (μHPLC) was performed by Shimadzu high performance liquid micro pump LC-5A (Shimadzu Corporation, Kyoto Japan). LC-5A is a delivering system of mobile phase for μHPLC using a small plunger reciprocating pump. In this instrument, employment of the constant displacement with quick return (CDQR) enables pulsation-free and stable flow even with a single plunger. CDQR means delivery solvent at a constant rate and with high speed suction. This instrument has a wide range of flow rate setting from 1 μl/min. to 9.900 μl/min. Specific is a high delivery pressure of 500 kg/cm^2 maximum. For a liquid chromatography system, a micro volume high pressure injector model 7520 (Rheodyne) with 0.5μL sample loop has been used. Separation of both the rhodamines was done at a micro column Prote–Col C_{18} (SGE Analytical, Australia), 150 mm long, 300 μm column internal diameter and pore size of 12 nm. Home made column holder and deposition device cell let move channel with constant rate and let effluent from micro column to be deposited into a fluidic channel. Complete instrumental set up is given at Figure 4.

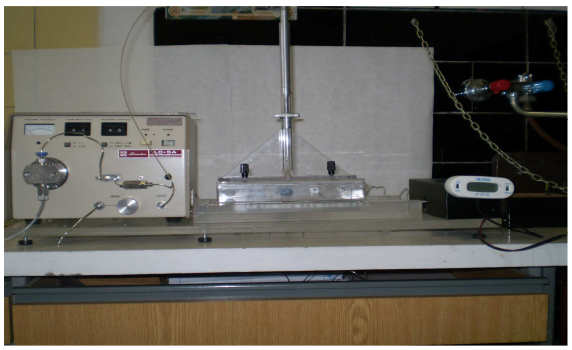

Figure 4. Analytical miniaturised system with micropump(left), separation microcolumn (middle) and fluidic channel with nanostructure in deposition cell (middle bottom).

 ISBN: 978-1-61208-214-1

Capillary μHPLC column was tested in the following conditions: mobile phase: acetonitrile/ water 60:40, v/v; mobile phase flow rate: 4 μL/ min; sample injection volume: 0.02 μL. A concentration of both the analytes in the mixture was 1 mmol/L. The Raman spectra were obtained using an i-Raman® instrument (B&W Tek). Excitation was provided by a 532.1 nm Nd:YAG laser. The laser power at the sample was approximately 9 mW. The acquisition time for each accumulation was 5 s.

III. RESULTS AND DISCUSSION

A. *μHPLC mobile phase optimization*

The optimization of μHPLC mobile phase composition has been based on the preliminary results obtained from thin layer chromatography (TLC) as documented in table 1. The retardation factor R_f, was calculated for a each spot according to the following formula:

$$R_f = a/b \quad (1)$$

where *a, b* are the distance moved by the sample component (a) and the solvent mixture (b). The best separation efficiency has been obtained by applying mobile phase methanol (MeOH) - water (80/20, v/v). The worse separation efficiency was obtained with dioxane- water mobile phase. The analytes were spread when acetonitrile-water mobile phase applied. Separation was controlled visually by a deposition of μHPLC effluent directly to white adsorption substrate sheet (Figure 5). The first eluted was RB, that is pink- violet coloured, and as a second one R6G characteristic with orange-red coloured spot (Figure 5).

TABLE I. THE RESULTS OF SEPARATION OF RHODAMINES MIXTURE (DEPOSITION LINEAR VELOCITY WAS 2.7 MM/MIN.).

Mobile phase	***Cell Temperature [°C]***	***Pump Pressure [x 100 kg/cm²]***	**Rhodamine R_F**	
			R6G	*RB*
MeOH-water 80:20	26.3	1.9	0.23	0.30
ACN - water 80:20	25.3	0.7	0.35	0.16
Dioxane: water 80:20	27.6	1.8	0.29	0.51

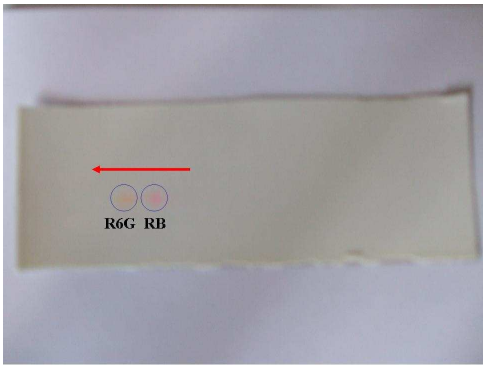

Figure 5. White substrate sheet with deposited effluent of micro column separated R6G and RB with MeOH-water mobile phase (80:20, v/v). Red arrow signals a micro column effluent deposition direction.

In the next experiment, the same mixture of rhodamines has been separated with the optimized mobile phase. The analytes eluted were continuously deposited into linearly moving microfluidic channel, containing functional gold-capped nanostructure that can enhance analytical signal in SERS. A micrograph of a cut microfluidic channel with a deposited nanostructure surface is given in Figure 6. Optimum effluent deposition rate as well a mobile phase flow rate were established at 2.7 mm/min. and 6 μL /min., simultaneously.

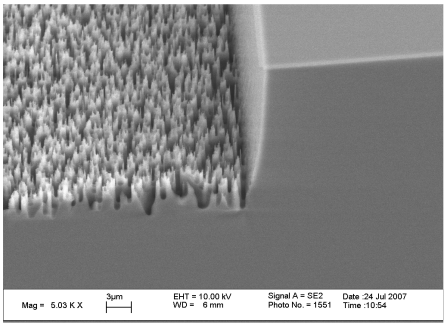

Figure 6. Micrograpg of silicon etched gold – capped nanostructure in fluidic channel.

B. *SERS detection of the R6G and RB at a gold- capped nanostructure*

Raman spectra of R6G and RB stock solutions at a gold – capped nanostructured surface are given at the Figures 7 and 8, respectively. There are the small differences in Raman shift positions. Significant is a lower intensity of the RB Raman bands to compare with R6G one. The Raman shift intensities were used for calculation of Raman signal enhancement for both the rhodamines at nanostructure in fluidic microchannel. The enhancement factor, *fe*, was calculated according to the following formula:

$$f_e = \frac{c_{ref}}{c_{sample}} \cdot \frac{I_{sample}}{I_{ref}} \quad (2)$$

where c_{ref} and c_{sample} are the reference concentration and sample concentrations, respectively, and I_{ref} is the signal intensity of the respective Raman peak.

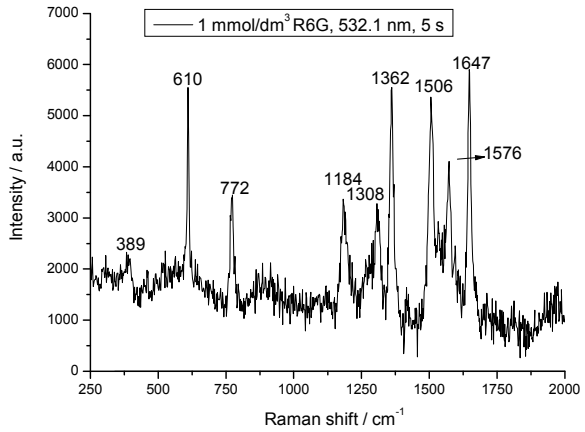

Figure 7. Raman spectrum of R6G at the gold-capped nanostructure.

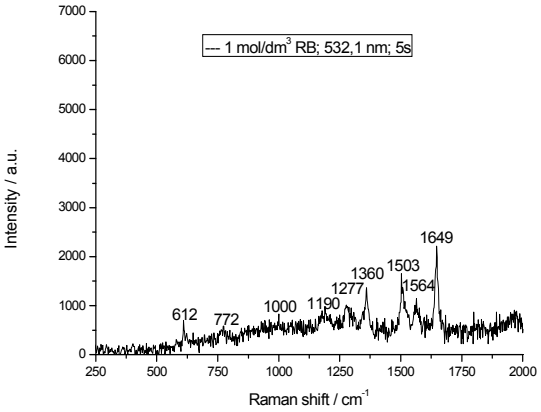

Figure 8. Raman signal intensity of RB stock solution at gold-capped nanostructure.

C. *SERS detection of the R6G and RB at a gold- capped nanostructure after a separation at micro column and deposition of an effluent into the fluidic microchannels*

Fluidic channels with the implemented gold-capped nanostructure were 25 or 30 μm wide and Raman signal shift was monitored for more intensive shift bands: 610, 1362, 1649 and 1506 cm^{-1} for R6G. Simultaneously, for RB the following Raman shift bands were concerned for data evaluation: 772, 1190, 1277 and 1564 cm^{-1}. From Figure 9, resulted position of R6G in the 30μm wide channel confirmed by SERS spectrum. Signal enhancement factor f_e for R6G was determined at value 9.71 (1362 cm^{-1}) and 7.29 (1564 cm^{-1}). It is less than reported in the experiments at surface nanosatructure [20].

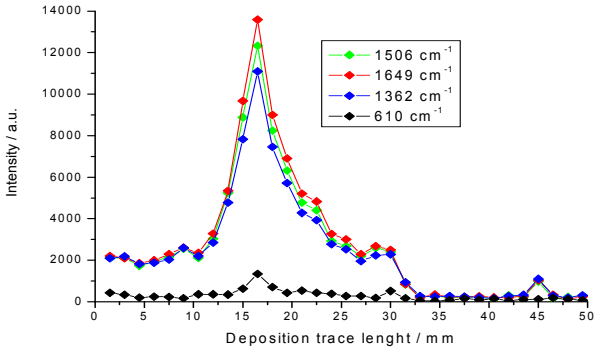

Figure 9. Signal intensity of Rama shift bands of separated and deposited rhodamine 6G at fluidic channel with gold-capped nanostructure. Mobile phase : MeOH:water , 80:20, v/v; 30μm channel width.

In a Figure 10, it is demonstrated detection of RB after chromatographic mixture separation and deposition of an effluent into a fluidic microchannel. The values of a signal enhancement f_e, were lower, ranging from 2.45 (1277 cm^{-1}) to 2.30 (1564 cm^{-1}). This is corresponding to difference in the Raman shift intensities (Figure 7, 8). In 20 μm wide channel was measured a lower Raman signal enhancement. It was in the range from 0.67 (1362 cm^{-1}) to 0.59 (1564 cm^{-1}) for R6G while only 0.19 (1277 cm^{-1}) and 0.18 (1564 cm^{-1}) in case of RB, which means no enhancement at all. An effluent deposition in this channel was probably strongly effected with a dispersion of the analytes separated from column directly at nanostructure. A mass of separated analyte was deposited in the length deposition trace. From the next results, it was confirmed that both the rhodamine analytes can be detected at nanostructure directly into a fluidic channel. Moreover, functional nanostructure affected signal enhancement for both the analytes. A position of RB was spread and no so sharp as given at Figure 9 for R6G.

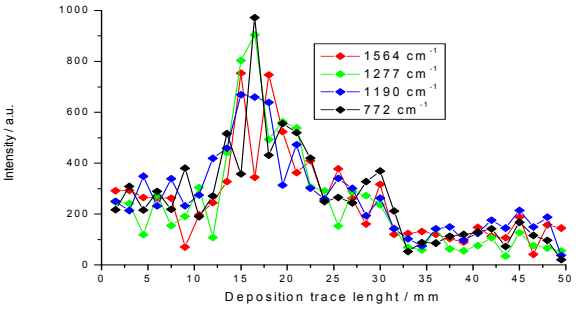

Figure 10. Rama signal shift of a separated and deposited RB in fluidics channel with gold-capped nanostructure. Mobile phase MeOH : water , 80:20, v/v; 30μm channel width.

 ISBN: 978-1-61208-214-1

There were also observed the special driven processes coupled with capillary force in microchannel and an analyte mass transfer that will be studied later on. The limits of detection, however, are fundamentally limited by local analyte concentration.

IV. CONCLUSIONS

A gold - capped silicon etched nanostructure has been deposited directly into microfluidic channel. With special μHPLC system and deposition device the separated rhodamines 6G and B have been deposited directly into integrated nanostructure in fluidic channel after chromatographic separation. From Raman spectroscopy band shift results it was found that rhodamine 6G can be good detected at gold–capped nanostructure in a micro-channel due to analytical signal enhancement, forced by nanostructure. Thinner, 20 μm wide microfluidic channel did not enable the equivalent signal enhancement. Generally, a Raman signal enhancement value was lower as in the measurements obtained out of microfluidic channel at the same defined nanostructure. Integration of functional nanostructure into a microfluidic channel enabled separated analytes deposition, spectroscopic detection, position scan, comparison of signal enhancement as well study of behaviou in this environment. The integrated nanostructures generate new functions that were directly included in an analytical miniaturized systems to form an analytical base for a chip or sensor integration.

ACKNOWLEDGMENT

The authors wish to thank MŠ SR VEGA 1/0211/12, APVV-0280-11 for financial support and Dr. I.Talian for silicon gold-capped nanostructure preparation.

REFERENCES

[1] S. Cho, D.-K. Kang, J. Choo, A. J. deMello, and S.-I. Chang, “Recent advances in microfluidic technologies for biochemistry and molecular biology”, BMB Reports vol. 44 pp. 705-712, 2011.

[2] D.-K. Kim, K. Kerman, M. Saito, R. R. Sathuluri, T. Endo, S. Yamamura, Y.-S. Kwon,and E. Tamiya, “Label-free DNA biosensor based on localized surface plasmon resonance coupled with interferometry”, Anal.Chem., vol. 79, pp. 1855-1864, 2007.

[3] D.-K. Kim, K. Kerman, S. Yamamura, Y.-S. Kwon, Y. Takamura,and E. Tamiya,”Label-free optical detection of protein antibody-antigen interaction on an capped porous anodic alumina layer chip”, Japan. J.Appl. Phys., vol. 47, pp. 1351-1354, 2008..

[4] C. Lim, J. Hong, B. G. Chung, A. J. deMello, and J. Choo,”Optofluidic platforms based on surface-enhanced Raman scattering”,Analyst, vol. 135, pp. 837-844, 2012.

[5] Y.-P. Kim, E. Oh, H. K. Shon, D. W. Moon, T. G. Lee, and H.-S. Kim,” Gold nanoparticle-enhanced secondary ion mass spectrometry and its bio-applications”, Appl. Surf.Sci. vol. 255, pp. 1064-1067, 2008.

[6] T. O. Dare, H. A. Davies, J. A. Turton, L. Lomas, T. C. Williams, and M. J. York,”Application of surface-enhanced laser desorpti - on/ionization technology to the detection and identification of urinary parvalbumin-alpha: a biomarker of compound-induced skeletal muscle toxicity in the rat”, Electrophoresis, vol. 23, pp. 3241-3251, 2002.

[7] S.-W. Ryu, Ch.-H. Kim, J.-W. Han, Ch. Jung, H. G. Park,and Y. K. Choi,” Gold nanoparticle embedded silicon nanowire biosensor for applications of label-free DNA detection”, Biosen. Bioelect., vol 25 pp. 2182-2185, 2010.

[8] J. C. Aspas, B. Heeg, B. Bescós, V. Zapata, and A. G. Ureña,”Vibrational enhancement on beam-surface ionization processes”, Faraday Disc., vol. 96, pp. 227-233, 1993.

[9] H. Wang, X. Luo, H. Yao, C. Du, Z. Y. Zhao, and S. Zhu,”Key technologies for LSPR-sensing microfluidic biochip”, art. No. 67241V, Proceedings of the society of photo-optical instrumentation engineers, 2007.

[10] G. Sharma, C. S. Chong, L. Ebin, V. Kripesh, C. L. Gan, and C. H. Sow,” Patterned micropads made of copper nanowires on silicon substrate for application as chip to substrate interconnects”, Nanotech. vol. 18, pp. 105-107, 2007.

[11] L. Geng, P. Jiang, J. Xu, B. Che, and F. Qu, Y. Deng,”Applications of Nanotechnology in Capillary Electrophoresis and Microfluidic Chip Electrophoresis for Biomolecular Separations”,Progr. Chem.,vol. 21, pp.1905-1921, 2009.

[12] R. M. Connatser, L. A. Riddle, and M. J. Sepaniak,”Metal-polymer nanocomposites for integrated microfluidic separations and surface enhanced Raman spectroscopic detection” J. Sep. Sci., vol. 27, pp. 1545-1550, 2004.

[13] L. W. Bezuidenhout, and M. J. Brett,”Ultrathin layer chromatography on nanostructured thin films”, J.Chromatogr. A, vol. 1183, pp. 179-185, 2008.

[14] A. Fonverne, F. Ricoui, C. Demesmay, C. Delattre, A. Fournier, J. Dijon, and F. Vinet,”In situ synthesized carbon nanotubes as a new nanostructured stationary phase for microfabricated liquid chromatographic column”, Sens. Actu. B, vol. 129, pp. 510 – 517, 2008.

[15] M. S. Haque, K. B. K. Teo, N. L. Rupensinghe, S. Z. Ali, I. Haneef, S. Maeng, J. Park, F. Udrea, and W. I. Milne,”On-chip deposition of carbon nanotubes using CMOS microhotplates”, Nanotech. vol. 19, pp.458-462, 2008.

[16] C. Escobedo, A.G. Brolo, R. Gordon, and D. Sinton, ”Optofluidic Concentration: Plasmonic nanostructure as concentrator and sensor, Nano Lett. vol. 12, pp.1592-1596, 2012.

[17] K. H. Chu, R. Xiao, and E. N. Wang,”Uni-directional liquid spreading on asymmetric nanostructured surfaces”, Nat. Mat., vol 9, pp. 413-417, 2010.

[18] J.Chen, J.Abell, Y-W. Huang and Y.Zhao,“On.Chip ultra-thin layer chromatography and surface enhanced Raman spectroscopy“,Lab on a Chip, in press.

[19] B.E. Alaca,”Integration of one-diemnsional nanostructures with Microsystems: an overview”,Int.Mat.Rev. vol.54, pp.245-260, 2009.

[20] I. Talian, M. Aranyosiová, A. Oriňák, D. Velič, D. Haško, D. Kaniansky, R. Oriňáková, and J. Hübner,”Functionality of novel black silicon based nanostructured surfaces studied by TOF SIMS”, Appl. Surf. Sci., vol. 256, pp. 2147-2154, 2010.

 ISBN: 978-1-61208-214-1

Evanescent Wave-based Near-wall Thermometry Utilizing Brownian Motion

Kanjirakat Anoop
Micro Scale Thermo Fluids (MSTF) Laboratory
Texas A&M University at Qatar
Doha, Qatar
e-mail: anoop.baby@qatar.tamu.edu

Reza Sadr
Micro Scale Thermo Fluids (MSTF) Laboratory
Texas A&M University at Qatar
Doha, Qatar
e-mail:reza.sadr@qatar.tamu.edu

***Abstract*—Evanescent wave-based Particle Image Velocimetry (or nPIV) is known to be an effective tool in estimating near-wall velocity fields. nPIV uses evanescent wave illumination of particle tracers in the fluid within order of O(100nm) from the wall where illumination intensity decays exponentially with distance normal to the wall. Brownian motion of the sub-micron tracer particles used in nPIV is a function of fluid temperature in this region. Monte Carlo simulation of particle movement in this region is used to investigate the possibilities of utilizing this effect for near-wall thermometry. Synthetic nPIV images of the illuminated polystyrene particles of 100nm diameter in the near-wall region are initially generated for different fluid temperature measurement. The spatial distribution of the particles takes into account the forces such as buoyancy, electrostatic repulsion and van der Waals attraction, in addition to the hindered Brownian motion near the walls. The synthetic images were then processed using standard cross-correlation function. The results of the numerical simulation show that the temperature variation causes a change in width and height of the nPIV correlation function. Initial experimental studies are conducted to verify the results of simulations.**

Keywords-Total Internal Reflection; nPIT; thermometry.

I. INTRODUCTION

Near-wall temperature measurement of a fluid at micro scale is an important part of studying convection heat transfer. Nano/micro-fabricated thermocouples and resistance temperature detectors (RTD) provides the highest out-of-plane resolution for temperature measurement [1]. However, these sensors are often complicated, somehow intrusive and can affect the flow structure in micro-scale flows. Non-intrusive thermometry such as infrared thermometry (IRT), molecular tagging thermometry (MTT), laser induced fluorescence thermometry (LIFT) and particle image velocimetry (PIV) based thermometry are generally preferred for micro-scale flow investigations [2]. In micro/nano-PIV, fluorescent tracer particles are seeded in the fluid to track the flow assuming they faithfully follow the fluid. Inevitably, as the seeding particle sizes are small, they undergo Brownian motion, where at low speed; this could introduce undesirable bias in the velocity measurements. The effect of the Brownian motion in PIV when using cross-correlation method, is a width-wise spreading of correlation peak. This effect is generally undesirable in velocimetry as it reduces signal-to-noise ratio of the results and increases the uncertainty in determination of the averaged particle displacement. Olsen and Adrian [3] proposed that such spreading of correlation peak could be utilized for thermometry, as Brownian motion of the seeded particles has direct dependence on temperature. Hohreiter et al. [4] demonstrated the use of correlation based micro-PIV technique utilizing Brownian motion of seeded particles to determine temperature. Their result shows a temperature measurement with an experimental accuracy of $\pm$ 3^{o}C inside a micro channel. In a separate study, Chamarthy et al. [5] noted that low image density PIV tracking method to process particle images performed better than cross-correlation based thermometry. The average difference between the predicted and measured fluid temperature was recorded to be $\pm$ 2.6^{o}C at an out-of plane resolution of ~ 20μm.

Zettner and Yoda [6] introduced an extension to μPIV technique based on evanescent-wave illumination generated by total internal reflection (TIR) of a laser beam at the fluid-solid interface between the flow and the wall, known as nano-PIV (nPIV). Sadr et al. [7] investigated the introduced error in velocity measurements as a result of particle mismatch due to "drop out" and "drop in" of particle tracers in the illuminated region brought in by the effects of hindered Brownian motion. Later, using an analytical approach, Sadr et al. [8] introduced an empirical relation between mean particle displacement and the average shear fluid velocity in the near-wall region with a given thickness. This was later expanded by studying the effects of Brownian motion, light penetration profiles, surface forces such as van der Waals, and electrostatic forces and the velocity gradient on the near-wall measurements using a traditional PIV cross-correlation method [9].

This paper extends the applicability of nPIV technique for temperature measurements utilizing the Brownian motion of seeded particles and proposes the use of nPIT (nano-particle image thermometry) technique for investigating near-wall temperatures. Monte Carlo simulation [8] is used to generate artificial images of particles in the evanescent wave region. Simulations are performed for fluid at stationary condition at different temperatures to simulate Brownian motion at varying temperatures. Effect of non-uniform illumination, hindered Brownian motion and the surface forces acting on the particles near the wall are considered while generating images of particles. Image pairs generated with a given time delay are cross-correlated to

 ISBN: 978-1-61208-214-1

analyze the spread of correlation peak width with temperature. Details of the methodology and theoretical model used are discussed next. Finally, experimental efforts are reported to verify the results of the simulations.

II. THEORETICAL MODEL

As mentioned earlier, in nPIV evanescent wave generated at the glass water interface is used to illuminate particles only in the near-wall region. When a light beam travels through a medium, with a refractive index n_1, into another transparent medium with a lower refractive index of n_2 at an angle exceeding the critical angle, $\theta_c=sin^{-1}(n_2/n_1)$, it is totally reflected at the interface. However, the electromagnetic field penetrates into the lower refractive index region and propagates for a small distance parallel to the interface creating what is called an evanescent wave. This evanescent wave is capable of exciting fluorescent particles in this region while the large numbers of particles farther away in the bulk liquid remain unexcited. Evanescent wave intensity, I, in the direction normal to the interface decays exponentially with distance, z:

$$I = I_0 \exp\left(-z/z_p\right) \tag{1}$$

where I_0 is the maximum intensity at the wall and z_p is the penetration depth:

$$z_p = \frac{\lambda_0}{4\pi n_1}\left[\sin^2\theta - \left(\frac{n_2}{n_1}\right)^2\right]^{-\frac{1}{2}} \tag{2}$$

λ_0 is the wavelength of the light and θ is the incident angle. For visible light at a glass water interface, z_p is on the order of O(100nm). Figure 1 shows the schematic of a general TIRF setup used in an nPIV experiment where only the near-wall fluorescent particles in the fluid are excited and viewed from the bottom of the microscope plate. The emission intensity of the tracer particles in this region is also an exponential function of the distance from the wall with a decaying trend as stated by Equation 1. However, depending on the optical characteristics of the imaging system, ultimate depth of visible region, z_v, depends on the intensity of the incident laser beam, fluorescent particle characteristics, camera and the background noise of the imaging system. In practice, this depth is usually more than the estimated penetration depth. In nPIV the focal depth of the objective lens is larger than the penetration depth of the evanescence wave, therefore, all the particles in the image are in focus and there is no back-ground light.

For a stationary fluid, the particle movement is a result of Brownian motion and surface forces. Brownian motion is the micro-scale movement of particles immersed in a fluid as a result of the thermal energy of the fluid. At submicron scale, Brownian displacement is of the same length scale as that of fluid convection and therefore becomes important during fluid velocimetry. Brownian motion is usually expressed in terms of its diffusion coefficient.

In an unconfined flow, Brownian diffusion coefficient is represented in the form of the Stokes-Einstein equation [10]:

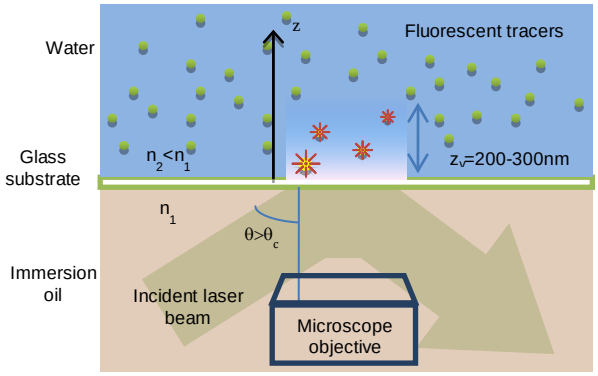

Figure 1. Schematic of nPIV measurement technique.

$$D = \frac{kT}{6\pi\mu a} \tag{3}$$

where k is the Boltzmann constant, T and μ are temperature and viscosity of the fluid, respectively. For liquids, with increase in temperature, absolute viscosity value decreases. Hence, for a smaller seeding particle diameter (100nm in this case) diffusion coefficient increases with increase in temperature when suspended in a liquid. Quantifying the relative change in random particle movement due to Brownian motion is the key principle used in nPIT.

In the near-wall region, where nPIT is interrogating, the diffusion coefficient is hindered due to the additional hydrodynamic effects at the wall and the Brownian diffusion coefficient, β, can be expressed in the tensor form as:

$$D = \begin{bmatrix} D_x & 0 & 0 \\ 0 & D_y & 0 \\ 0 & 0 & D_z \end{bmatrix} = D \begin{bmatrix} \beta_{\parallel} & 0 & 0 \\ 0 & \beta_{\parallel} & 0 \\ 0 & 0 & \beta_{\perp} \end{bmatrix} \tag{4}$$

where $\beta_{\perp}$ and $\beta_{\parallel}$ are the wall correction factors for movement perpendicular and parallel to the wall, respectively [11]:

$$\beta_{\parallel} = \left[1 - \frac{9}{16}\left(\frac{a}{z}\right) + \frac{1}{8}\left(\frac{a}{z}\right)^3 - \frac{45}{256}\left(\frac{a}{z}\right)^4 - \frac{1}{16}\left(\frac{a}{z}\right)^5\right], \tag{5}$$

and

$$\beta_{\perp} = \left[\frac{2h\cdot(3h+a)}{(6h^2+9ah+2a^2)}\right] \tag{6}$$

where a is the particle radius and $h=(z-a)$. As the particles move away from the wall, the correction factors tend to unity and the diffusion coefficient tends to that of the Stokes-Einstein value. In present simulation, this anisotropic nature of Brownian diffusion coefficient is considered.

Particle displacements due to Brownian motion are obtained from Langevin equation, which describes the displacement of a spherical particle, $\Delta\vec{x}$, over a time period,

Δt, [12]. For a stationary fluid with no external forces acting on the particle, the Langevin equation in x direction reduces to [11]:

$$\Delta x = \sum_{t=0}^{t=\Delta t} \{\chi \delta r_x\} \quad (7)$$

where χ is an array of normally distributed random numbers with a mean of zero and a standard deviation of one and $\delta r = \sqrt{2D\delta t}$. In z direction, perpendicular to the wall, there is no translational velocity and only the first term in the Langevin equation reduces to:

$$\Delta z = \sum_{t=0}^{t=\Delta t} \left\{ \frac{D_z}{kT} F_z \delta t + \frac{dD_z}{dz} \delta t + \chi \delta r_z \right\} \quad (8)$$

External forces acting on particles in the direction perpendicular to the wall include, electrostatic forces and van der Waals forces [13, 14], F_{el} and F_{vdw}, respectively, caused by the presence of the wall, plus buoyancy force, F_b, which is a result of density mismatch between the suspending medium and the tracer particles. The total force acting on a particle in the direction normal to the wall would be the summation of all these forces, $F_z = F_{el} + F_{vdw} + F_b$, where, the combined effects of electrostatic, van der Waals, and buoyancy forces generate a net repulsive force that pushes the tracers away from the wall [9].

III. MONTE CARLO SIMULATION

Simulations are carried out with exponentially decaying illumination. Artificial images of tracer particles at time $t = 0$ and later at time $t=\Delta t$ are generated. Particle displacements in the x, y and z directions are calculated for different time steps of $\Delta t = \sum \delta t$ using equations 7 and 8 which encompasses the effects of Brownian motion and other external forces. The time step $\delta t = 5\ \mu$s used in this work is much smaller than Δt and is an order of magnitude larger than the particle momentum relaxation time. Particle–wall collisions are considered to be perfectly elastic, preventing any particles from going 'through' the wall.

Non-uniform illumination is considered while generating artificial images for present work replicating an actual evanescent wave illumination. The brightness (size) of the particle images are a function of their distance from the wall, where particles near the wall look bigger and brighter than those further away. By implementing an exponentially decaying intensity of illumination normal to the wall, variation in particle image sizes in the field was created. Particle images in this work were assumed to be circular with a Gaussian intensity distribution profile with a peak greyscale value calculated using the equation

$$I_p = C \cdot \exp\left(-h / z_p\right) \quad (9)$$

where $h=(z-a)$ and C represents the net power emitted and collected from the bottom of each sphere and a is particle radius [7]. The effective particle image diameter, D_{image} = 8 pixels, has an Airy disk pattern, which can be approximated using a Gaussian profile with an approximate diameter of the point spread function of the microscope system [15]. Electronic noise and shot noise are also added to the image using a combination of white and Gaussian distribution noise, respectively [9] to mimic real image characteristics.

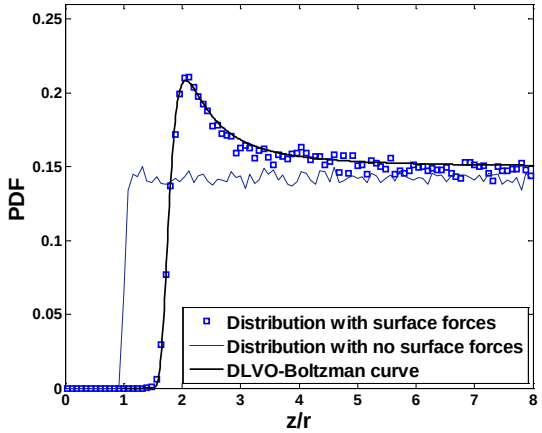

Figure 2. PDf's of particle distribution throughout z_v.

Initially, 1500 particles of radius 50 nm are distributed over a distance of $5z_p$ normal to the wall in the fluid for simulation. This results in a particle density of ~1.89 particles/μm^3, in an image size of (653x70) pixels in the x and y directions, similar to actual experimental images. Particles are initially uniformly distributed in the flow and then surface forces move the particles to their final steady state distribution. The final Probability Distribution Function (PDF) of the particles throughout the visible region, z_v, at this stage is shown in Fig. 2 for two cases of a) no surfaces forces, b) surface forces for ζ-potentials of $\zeta_{particle}$ = 100mV and ζ_{wall} = 80mV respectively [16, 17]. The surface forces and zeta potential of the particles and surface contribute significant effect in the distribution of particles near the wall. As can be seen from the figure, when the surface forces effects are considered, the particles are seen pushed away from the wall region, making sparse density of particles near to the walls. It is also observed that the steady state probability distribution function of the particles, for a given surface force, can adequately be modeled by a Boltzmann profile as reported before [16]. In present simulations, inter-frame time delays more than 2ms are used. This is mainly due to the fact that longer time delays provided better measurement sensitivity with variation in temperature. However with increase in time delays, the noise-to-signal ratio also increased, reducing the accuracy.

IV. RESULTS AND DISCUSSION

2500 independent artificial image pairs of 653 x70 pixels of tracer particles at time t=0 and later at time $t=\Delta t$ were generated. The images in each pair were then post–processed using a standard FFT-based cross correlation program that uses a 3D Gaussian peak finding algorithm based on a Gaussian surface fit [9]. Each image was divided into five adjacent interrogation windows, each 186×68 pixels size

with an overlap of ~50%, with the midpoints positioned along the center line of the image in the *y* direction. The image pairs are then cross- correlated to obtain the cross correlation coefficient.

Figure 3 shows the cross-correlation coefficient variation for different fluid temperatures after ensemble averaging. As can be noted, the peak height decreases whereas the peak width of the correlation increases with increase in fluid temperature. The above variation is for an inter-frame time delay of 3ms. The correlation function as depicted in Fig. 3 is obtained after carrying out ensemble averaging of all the correlation planes of 2500 image pairs. The main advantage of ensemble averaged correlation approach is the fact that the noise in individual correlation planes is significantly reduced by having an averaged correlation plane.

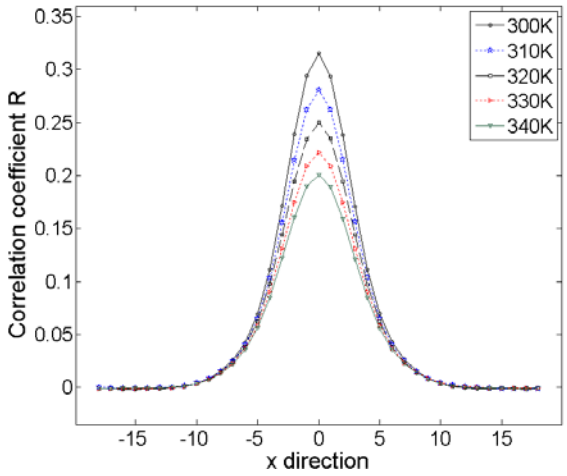

Figure 3. Cross-correlation coefficient for different fluid temperatures

Usually, ensemble averaging alone would mitigate the noises present, however, it is noticed in the simulations that there exits some correlation planes (about 1-2%) which had higher noise-to-signal ratio. Including them in analysis, would increase the uncertainties while determining peak widths and heights. Hence, before averaging bad correlation planes that are having a noise-to-signal ratio below 0.9 are removed from the analysis. It is noted that at lower temperatures, more number of correlation planes exists which has lower noise-to-signal ratio. As temperature is increased, the number of correlations with higher noise-to-signal ratio also increased. Since correlations with lower noise-to-signal ratio could adversely affect the peak width and height evaluation.

Figure 4(a) shows peak width variation with temperature for two inter-frame time delays of 3ms and 5ms. Peak width is estimated by fitting a Gaussian surface with at least 13 points in the peak region:

$$G(x,y) = A \cdot \mathrm{e}^{\frac{-(x-x_0)}{2\sigma_x^2}} \times \mathrm{e}^{\frac{-(y-y_0)}{2\sigma_y^2}} \qquad (10)$$

where A is the peak height and σ_x and σ_y are representatives peak widths in x and y directions.

For a stationary fluid, both the widths should be similar in magnitude [5]. The error bars as depicted in the figure represent 95% confidence levels of the presented data calculated as suggested by Benedict *et al.* [18]. A close observation of the figure shows that the uncertainty in the width estimated for a time delay of 5ms is higher than that for 3ms. Uncertainties are also observed to be higher at the higher temperatures. The reason for the above observation would be an existence of a better correlation, which is having a smaller spread in uncertainties at lower time delays. However, higher temperature sensitivity is observed for the longer time delays, as the effect of temperature on Brownian motion is more reflected when time delays are higher.

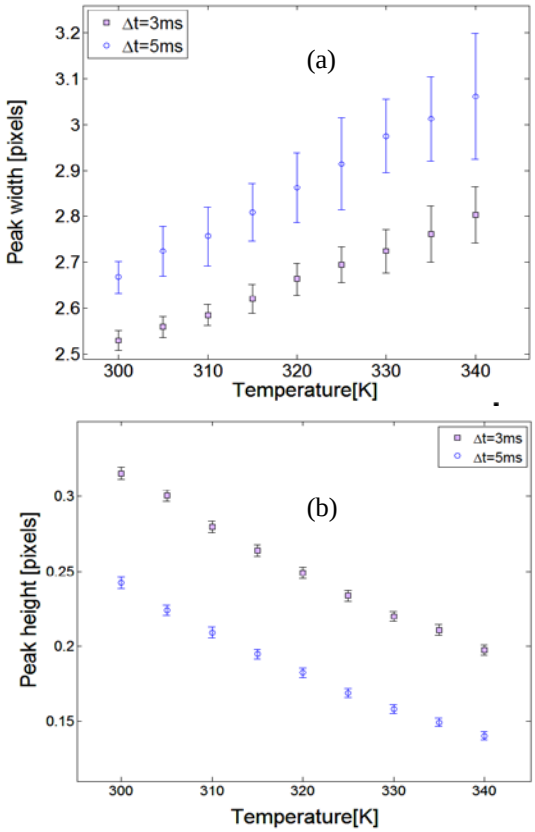

Figure 4. (a) Peak width variation with temperature (b) Peak height variation with temperature.

Figure 4(b) shows variation of the peak height with temperature for the same time delays as given in Fig. 4(a). As peak width and height variations seem to have opposing trends, therefore, the ratio of peak width to height would be a better parameter for thermometry. Peak width to height ratio variation for various temperatures for two time delays is depicted in Fig. 5. In this figure also, the sensitivity with temperature is seen to be more for 5ms than for 3ms. However, the uncertainties are lower in the case when the inter-frame time delay was 3ms. It can be concluded that the ratio of correlation width to height may be used to obtain fluid temperature in the near-wall region for an nPIT setup. After noticing the feasibility of using nPIT technique based on synthetic images efforts are made to conduct experiments.

 ISBN: 978-1-61208-214-1

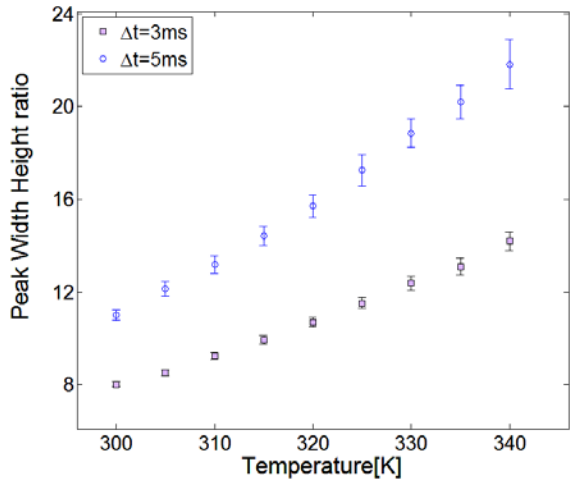

Figure 5. Variation of peak width to height ratio with temperature

V. INITIAL EXPERIMENTS

Some initial experiments are conducted to practically validate the observed effects of simulations. An experimental setup as depicted in Fig. 6(a) is used to confine the fluid at a constant temperature and to analyze the Brownian motion of seeded particles. Constant temperature condition is achieved using a temperature controlled microscope stage. The temperature of the stage is adjusted by circulating water from a constant temperature water supply (F25-ED Julabo). A metal substrate with a hole drilled and a glass coverslip (0.13mm thick) pasted below holds the sample fluid. The heat from the microscope stage is effectively conducted to the sample fluid through the metal substrate. The fluid temperature is recorded using a precision K-type thermocouple inserted in the sample through an insulated block, placed on top of the metal substrate.

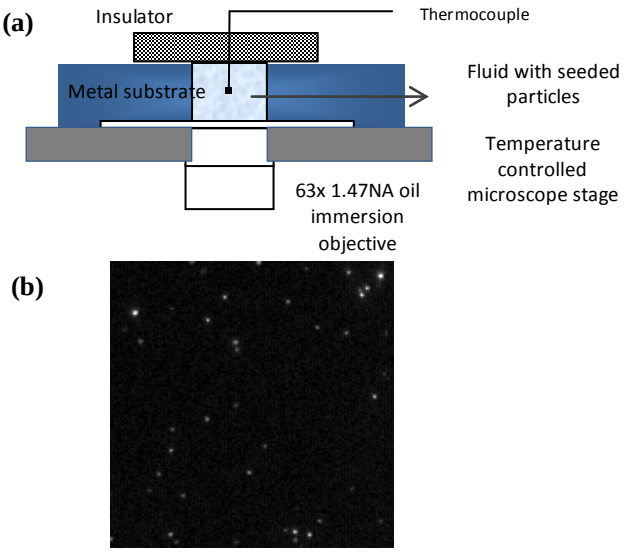

Figure 6. (a) Schematic of experimental setup used (b) Typical nPIV image obtained

An Argon-Ion CW laser beam with a wave length of 488 nm (Spectra Physics BeamLok 2060) was used to provide excitation light in the near-wall region. Images were obtained using an EMCCD camera (ProEM 512, Princeton Instruments) attached to an inverted epi-fluorescence microscope (Leica DMI6000B) via a 63x 1.47NA oil immersion objective. The pixel resolution for the images obtained from this imaging set up was 4×10^6 (pixel/meter). The nPIV seeding particles used were 100nm (±5%) diameter polystyrene fluorescent particles (F8803, Invitrogen) having peak excitation and emission wavelengths of 505nm and 515nm, respectively. In all the experimental runs, the fluorescent particle concentration was maintained at a constant volume concentration of 0.017%. Evanescent wave illumination was generated on the bottom glass-water interface in the microchannel. The angle of incidence of light in the water-quartz interface was evaluated to be 75°, based on the numerical aperture value of the objective lens and refractive indices at the interface. This yielded a penetration depth of $z_p \cong 105$nm (Eq. 2). The depth of visible region (z_v) is then estimated to be 310nm for the basefluid. This estimation is based on the penetration depth and the intensity value of the background noise in captured images. A typical nPIT image obtained during experimentation is shown in Fig. 6 (b).

For each experiment, 1500 nPIT image pairs of 200x200 pixels were acquired with a inter frame time delay of 0.5 ms. The interrogation window size was set at 186×68 pixels with a search radius of 15 pixels. In each case, there were sufficient numbers of matched tracer particles in the interrogation windows. The images are then post–processed using the same cross-correlation program used in the simulation section to determine the correlation peak width and height.

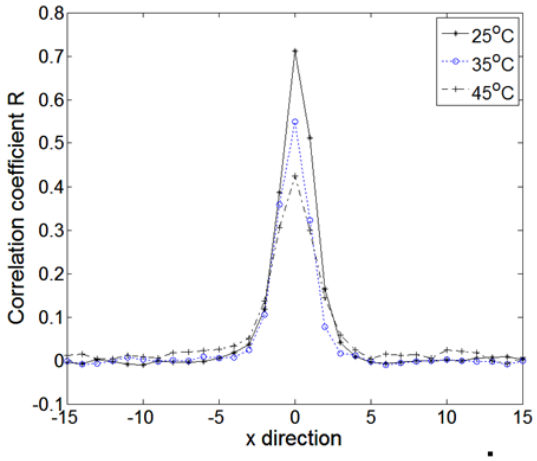

Figure 7. Experimental cross-correlation coefficient for different fluid temperatures

Figure 7 shows the experimental observation of cross-correlation function for temperatures varied from 25°C to 45°C. The trend of peak height reduction and peak width

broadening are observed to be similar to that of the simulations. In order to strengthen the correlation and to reduce the spread of uncertainties in peak width, a smaller inter-frame time delay of 0.5ms is considered in the experiment. However, experimental uncertainties are observed to be much higher than simulations. Nevertheless, the initial experimental results are presently reported here to show the practical feasibility of using nPIT technique and more strenuous efforts are required in future to obtain a highly repeatable cross-correlation relation with temperature.

VI. CONCLUSIONS AND FUTURE WORK

The present work investigated the feasibility of using evanescent wave illumination technique for temperature measurement. Monte Carlo simulation is used to artificially generate nPIV images of stationary fluid seeded with fluorescent particles with an exponentially decaying intensity from the wall. These images are then cross-correlated to investigate the effect of temperature on the peak width and height of the cross-correlation function. The results of simulations show that correlation width increase whereas its height decreases with increase in fluid temperature. Uncertainties in the measured peak width are lower when the inter-frame time delays are short. However, the sensitivity with temperature is observed to be more when the time delays are longer. Peak width to height ratio is observed to be a better parameter for quantifying while using nPIT technique. More elaborate experimental observations with varying time delays are required in the future in order to completely quantify the effect of Brownian motion on thermometry.

ACKNOWLEDGMENT

This publication was made possible by NPRP grant # 08-574-2-239 from the Qatar National Research Fund (a member of Qatar Foundation). The statements made herein are solely the responsibility of the authors.

REFERENCES

[1] P. R. N. Childs, J. R. Greenwood, and C. A. Long, “Review of temperature,” Review of Scientific Instruments, vol. 71, pp. 2959-2978, 2000.

[2] P. Chamarthy, S. V. Garimella, and S. T. Wereley, “Measurement of the temperature non-uniformity in a microchannel heat sink using microscale laser-induced fluorescence,” International Journal of Heat and Mass Transfer, vol. 53, pp. 3275-3283, 2010

[3] M. G. Olsen and R. J. Adrian 2000, “Brownian motion and correlation in particle image velocimetry,” Optics & Laser Technology vol. 32, pp. 621-627,2000.

[4] V. Hohreiter, S. T. Werely, M. G. Olsen, and J. N. Chung, “Cross-correlation analysis for temperature measurement,” Measurement Science and Technology, vol. 13, pp. 1072-1078, 2002

[5] P. Chamarthy, S. V. Garimella, and S. T. Wereley, “Non-intrusive temperature measurement using microscale visualization techniques,” Experiments in Fluids, vol. 47, pp. 159-170, 2009.

[6] C. M. Zettner and M. Yoda, “Particle velocity field measurements in a near-wall flow using evanescent wave illumination,” Experiments in Fluids, vol. 34, pp. 115-121, 2003.

[7] R. Sadr, H. Li, and M. Yoda, “Impact of hindered brownian diffusion on the accuracy of particle-image velocimetry using evanescent-wave illumination,” Experiments in Fluids, vol. 38, pp. 90-98, 2005.

[8] R. Sadr, C. Hohenegger, H. Li, P. J. Mucha, and M. Yoda, “Diffusion-induced bias in near-wall velocimetry,” Journal of Fluid Mechanics, vol. 57, pp. 443-56, 2007

[9] R. Sadr, K. Anoop, and R. Khader, “ Effects of surface forces and non-uniform out-of plane illumination on the accuracy of nPIV velocimetry,” Measurement Science and Technology, vol. 23, 055303, 2012

[10] A. Einstein, “Uber die von der molekularkinetischen theorie der warme geforderte bewegung von in ruhenden flussigkeiten suspendierten teilchen,” Ann Physics, vol. 17 pp. 549, 1905.

[11] M. A. Bevan and D. C. Prieve, “Hindered diffusion of colloidal particles very near to a wall: revisited,” Journal of Chemical Physics, vol. 113, pp. 1228-36, 2000

[12] A. T. Clark, M. Lal, and G. M. Watson, “Dynamics of colloidal particles in the vicinity of an interacting surface,” Faraday Discussion of the Chemical Society, vol. 83 pp. 179-191, 1987.

[13] M. Oberholzer, N. Wagner, and A. M. Lenhoff, “Grand canonical Brownian dynamics simulation of colloidal adsorption,” Journal of Chemical Physics, vol. 107 9157-67, 1997.

[14] A. Banerjee and K. D. Kihm, “Experimental verification of near-wall hindered diffusion for the Brownian motion of nanoparticles using evanescent wave microscopy,” Physics Review E, vol. 72, 042101/1-4, 2005.

[15] C. Meinhart and S. T. Wereley**, “**The theory of diffraction-limited resolution in microparticle image velocimetry,” Institute of Physics Publishing, Measurement Science and Technology, vol. 14, pp. 1047-53, 2003.

[16] P. Huang, J. S. Guasto, and K. Breuer, “The effects of hindered mobility and depletion of particles in near-wall shear flows and the implications for nanovelocimetry,” Journal of Fluid Mechanics, vol. 637, pp. 241-265, 2009.

[17] J. A. Fagan, P. J. Sides, and D. C. Prieve, “Calculation of ac electric field effects on the average height of a charged colloid: effects of electrophoretic and Brownian motions,” Langmuir, vol. 19, pp. 6627-32, 2003.

[18] L. H. Benedict and R. D. Gould, “ Towards better uncertainty estimates for turbulence statistics,” Experiments in Fluids, vol. 22, pp. 129-136, 1997.

 ISBN: 978-1-61208-214-1

Effect of Erythrocyte Sedimentation and Aggregation on the Conductivity of Blood in a Miniature Chamber

Alexander Zhbanov
Department of Medical System Engineering
Gwangju Institute of Science and Technology (GIST)
Gwangju, Republic of Korea
e-mail: azhbanov@gist.ac.kr

Sung Yang
Department of Medical System Engineering
School of Information and Mechatronics
Department of Nanobio Materials and Electronics
Gwangju Institute of Science and Technology (GIST)
Gwangju, Republic of Korea
e-mail: syang@gist.ac.kr

***Abstract*—The mechanisms influencing the erythrocyte sedimentation and aggregation still remain unclear despite considerable research effort. In this study, we determined the erythrocyte sedimentation rate (ESR) by measuring the electrical conductivity of blood in a miniature chamber with two planar electrodes on the bottom. As the red blood cells settle towards the bottom, the hematocrit (HCT) or erythrocyte volume fraction increases continuously with the time in the lower part of volume. The measured conductivity of blood in the chamber slightly increased during the first minute of observation and then decreased for more than 1.5 h. The dielectric theory was applied to determine the effective conductivity of blood. We have shown the increase of blood conductivity due to aggregation by both experimentally and theoretically. We have investigated the ESR at different HCT levels by using experimentally measured decreasing of blood conductance with time. A particle dynamic model (PDM) was developed to elucidate the relationship between the microfluidic interaction of red blood cells (RBCs) and macroscopic ESR tests. We estimated the initial velocity and acceleration of erythrocytes and completion time of sedimentation.**

Keywords-blood conductivity; erythrocyte sedimentation rate (ESR); aggregation; particle dynamic model (PDM)

I. INTRODUCTION

The erythrocyte sedimentation rate (ESR) is a simple and inexpensive laboratory test for assessing the inflammatory or acute response. The International Committee for Standardization in Hematology recommends the use of the Westergren method [1]. The duration of the Westergren test is one hour. The idea of shortened erythrocyte sedimentation rate evaluation (about 30, 20, 10 min or shorter) was discussed in several works [2-4]. However, the acceleration and automation of the ESR test encounters difficulties because the mechanisms influencing the erythrocyte sedimentation rate still remain unclear, despite considerable research efforts. A critical review of current models of the erythrocyte sedimentation is given in a recent work [5].

Several investigators have measured the time dependence of the blood conductivity. These studies based on the phenomenon that, as the red cells settle, hematocrit (HCT) decreases in the upper region of the blood column [5-9]. In the present work, we study the changes in blood conductivity during the aggregation and sedimentation in a small chamber with two planar electrodes on the bottom. The measured conductance of blood in the chamber increases slightly during the first minute of observation and then decreases longer than one hour.

In this work, we try to find the relation between ESR and blood conductivity during the sedimentation. We consider the effective medium theory describing electrical conductivity of coated ellipsoidal particle suspensions. We compare our experimental data with theoretical prediction of blood conductivity. We develop a particle dynamic model (PDM) to elucidate the relationship between the microfluidic interaction of red blood cell (RBC) and macroscopic ESR test. We estimate the initial velocity and acceleration of erythrocyte and the time taken for sedimentation.

The structure of the paper is as follows. Section II describes material, methods, and measuring changes in the blood conductivity. The effective medium theory and its application to calculate the conductivity are given in Section III. The influence of RBC aggregation and sedimentation on the blood conductivity is also considered in this Section. The estimation of RBC sedimentation speed is given in Section IV. Section V offers the particle dynamic simulation of RBC aggregation and sedimentation. In addition, different ways of describing the aggregation of particles is discussed here. Our conclusions appear in Section VI.

II. CHANGES IN BLOOD CONDUCTIVITY DURING AGGREGATION AND SEDIMENTATION

A. Measurement System

The schematic drawing of fabricated device is shown in Fig. 1. The device is fabricated by conventional MEMS process. It is consists of a polydimethylsiloxane (PDMS) chamber (5mm-wide and 5mm-deep) and two gold-paleted 2D planar electrodes, each of width 300 μm with gap 1200 μm apart. The 200 nm thick gold film was sputtered and then wet etched to the shape of electrodes.

To record a data, an impedance analyzer (4294A, Agilent technologies) [10], and a data acquisition system (National Instruments, LabVIEW) [11] were used.

 ISBN: 978-1-61208-214-1

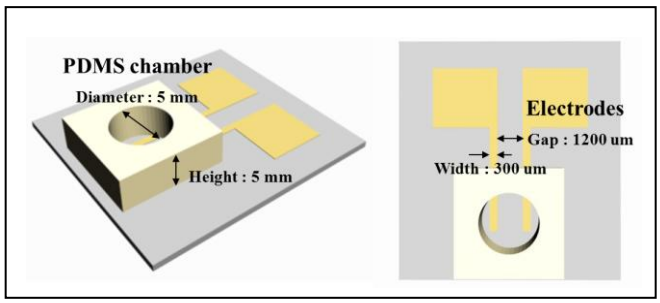

Figure 1. Schematic of the device for measuring the electrical conductivity of blood

B. *Preparation of Blood Samples*

Venous blood samples were drawn from the antecubital vein of healthy volunteers and collected in vacutainers (6 ml, BD, Franklin Lakes, NJ, USA), which contained (K2) Ethylenediaminetetraacetic acid (EDTA) as the anti-coagulant.

In order to prepare the samples with different concentrations of fibrinogen, the whole blood was centrifuged at 3000 rpm for 10 min, and then the plasma and buffy-coat were removed. The erythrocytes were washed three times with an isotonic phosphate buffered saline (PBS, pH=7.4, 290mOsmol/kg) to eliminate fibrinogen on their surface. The erythrocytes, plasma, and PBS were then mixed in desired proportion.

C. *Time Dependence of Blood Conductivity*

We measured the conductivity σ of whole blood samples, with HCT values of 35, 45, and 55%, respectively, over a period of 5000 s. The results are shown in Fig. 2. The initial change in conductivity is shown in the inset.

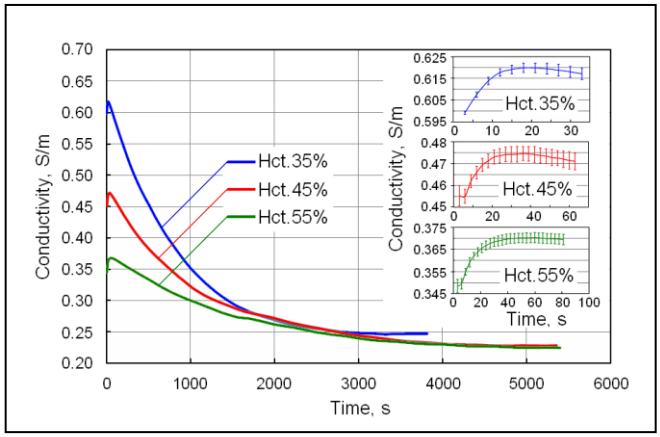

Figure 2. Changes in the conductivity of blood during sedimentation.

The effective conductivity has a physical meaning only for a homogeneous suspension of mixed particles. During sedimentation, the conductivity of blood varies on height. However, we prefer to use a unit of conductivity, because at the initial time the conductivity corresponds to the conductivity of a homogeneous blood suspension and at the end of sedimentation it is very close to the conductivity of deposit.

Fig. 2 shows that the conductivity of the blood in the chamber increased during the first minute of observation. The conductivity then decreased, and continued to do so for more than 1.5 h. The conductivity for the period during which it was increasing is shown in more detail in the inset to Fig. 2.

We injected the erythrocyte suspension into the chamber using a pipette, and immediately began recording the conductivity. In our experiments, the conductivity remained constant during the first few seconds. We attribute this to the initial movement and mixing of the suspension after it had been injected into the chamber (prior to any aggregation).

III. CONDUCTIVITY OF WHOLE BLOOD

A. *Effective Medium Theory of the Electrical Conductivity of Blood*

Erythrocytes make up ~ 99% of the total amount of cells in the blood plasma. Thus, the physical properties of red blood cells and plasma have a decisive influence on the aggregation, the sedimentation, and the electrical conductivity of blood.

The human erythrocyte is a conducting biconcave discoid coated with a thin insulating membrane. We have based our method for calculating the effective conductivity of whole blood on effective medium theory. It seems accurate to assume that blood may be considered to be a mixture of randomly oriented spheroidal particles (Fig. 3) [12, 13].

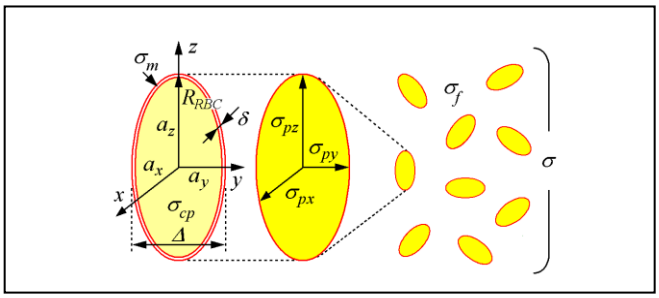

Figure 3. Model of coated spheroidal particles for red blood cells.

We define the axes of the ellipsoids to be $a_x = a_y$, and a_z (aligned with the x, y, and z axes of the reference frame), in order to model spheroidal inclusions.

The thickness δ of the erythrocyte membrane is very small (Fig. 3). In this case δ/a_x, δ/a_y, $\delta/a_z << 1$, and the volume ratio v of the inner ellipsoid to the outer ellipsoid is approximately given by

$$v \approx (1 - \delta/a_x)(1 - \delta/a_y)(1 - \delta/a_z). \quad (1)$$

The equivalent conductivity of the coated ellipsoid has three components σ_{px}, σ_{py}, and σ_{pz}. Each component σ_{pk} for the k- axis ($k = x, y, z$) is expressed as:

 ISBN: 978-1-61208-214-1

$$\sigma_{pk} = \sigma_m \frac{\beta_k \sigma_m + \sigma_{cp} - \beta_k \nu(\sigma_m - \sigma_{cp})}{\beta_k \sigma_m + \sigma_{cp} + \nu(\sigma_m - \sigma_{cp})}. \quad (2)$$

where σ_m and σ_{cp} are the electrical conductivity of membrane and cell cytoplasm respectively, $\beta_k = (1 - L_k)/L_k$. The depolarisation factors, L_k, in closed form are given elsewhere [12-14].

Appling Bruggeman's procedure [15] to a dispersion of ellipsoids, we can find the effective conductivity:

$$\sigma = \sigma_f + \frac{\frac{1}{3}\phi_p \sigma_f \sum_k^{x,y,z} \frac{(\sigma_{pk} - \sigma_f)}{\sigma_f + L_k(\sigma_p - \sigma_f)}}{1 + \phi_p \left[\frac{1}{3}\sigma_f \sum_k^{x,y,z} \frac{1}{\sigma_f + L_k(\sigma_{pk} - \sigma_f)} - 1 \right]}. \quad (3)$$

where σ_f is the conductivity of plasma, ϕ_p is the volume fraction of erythrocytes and σ is the conductivity of blood.

Equation (3) is similar to that proposed by Giordano et al. [16] if we use (2) for the principal conductivities.

B. Comparison of Theoretical and Experimental Data

Analyzing the published data, we selected the following average values of blood parameters: conductivity of the erythrocyte cell membrane $\sigma_m = 5 \cdot 10^{-5}$ S/m and of the RBC cytoplasm $\sigma_{cp} = 0.5$ S/m; radius of red cells $R_{RBC} = 4$ μm and thickness $\Delta = 2$ μm; membrane thickness $\delta = 7.5 \cdot 10^{-3}$ μm.

The conductivity of plasma at T = 24 and 37 °C was assumed to be $\sigma_f = 1.2$ and 1.57 S/m, respectively. All our experiments were performed at room temperature 24±1 °C. Equation (3) predicts conductivities that closely match the experimental values of the disaggregated erythrocyte suspensions.

A comparison of the blood resistivity for a range of HCT from published experimental data and our study (3) is given in Fig. 4.

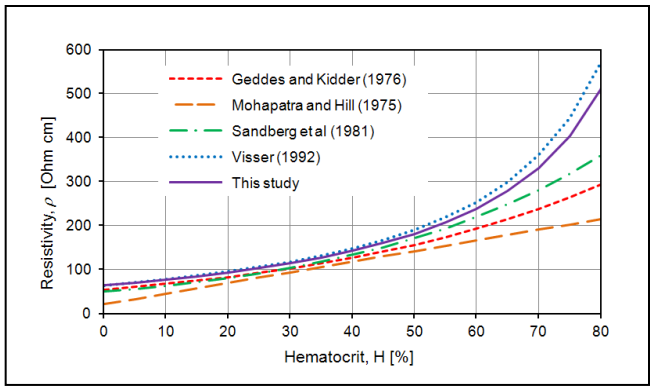

Figure 4. Dependence of the blood resistivity on HCT.

The red dotted line corresponds to Geddes and Kidder empirical formula [17]. The orange long-dashed line is Mohapatra and Hill data [18]. The green dashed-dotted line shows Sandberg et al. dependence [19]. The blue dotted line is Visser's experimental data [20]. The violet solid line shows the results generated using (3). Our approximation demonstrates a good agreement with experimental data.

C. Influence of RBC Aggregation on the Conductivity

Erythrocytes can aggregate to form rouleaux. We use the term *aggregation number* to specify the number of 'coins' in an aggregate. Fig, 5A depicts an aggregate in which the aggregation number is 5 A disaggregated mixture has aggregation number 1. A good approximation for such pile would be a heterogeneous cylinder shown in Fig. 5B. The equivalent conductivity of the heterogeneous cylinder has three components $\sigma_{px} = \sigma_{py}$, and σ_{pz} (see Fig. 5C). Applying (2) in limits when a_x and a_y tend to infinity and when a_z tends to infinity, we have $\sigma_{px} = \sigma_{py} = 0.0253$ S/m and $\sigma_{pz} = 0.00658$ S/m. Next, we use the model of prolate ellipsoids instead of cylinders (Fig. 5D).

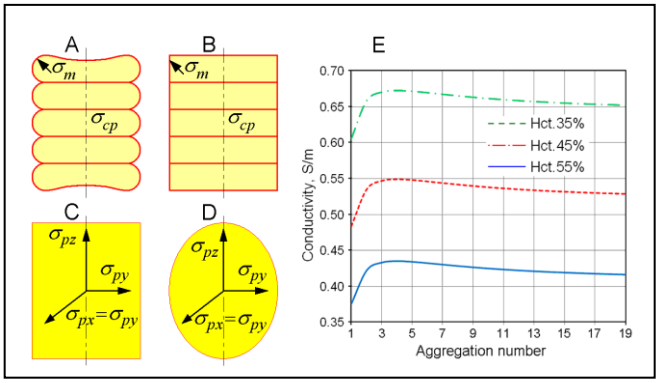

Figure 5. Models for an erythrocyte aggregation in rouleaux (A)-(D) and increasing in blood conductivity with aggregation nubmer (E).

Our calculation of changing in the whole blood conductivity with aggregation number is shown in Fig. 5E. The maximum increase in conductivity is approximately 0.075 S/m at aggregation number 4 for all levels of HCT. In our experiment we observe the maximum increase of 0.02 S/m (Fig. 2). We explain this deviation by the fact that in our experiment we have the mixture of RBCs with various aggregation numbers.

D. Decreasing of Conductivity with RBC Sedimentation

In our experiments, the conductivity approached a minimum of approximately 0.225 S/m at the end of sedimentation. Analyzing results calculated by (3) we can conclude that the HCT of deposit is H = 70%. We analytically approximated the change in conductivity with time using the following exponential dependence:

$$\sigma = A_1 \exp(-B_1 t) + C_1. \quad (4)$$

where $C_1 = 0.225$ S/m is the blood conductivity at H = 70%.

 ISBN: 978-1-61208-214-1

The coefficients A_1 and B_1 we obtained for different HCT are given in Table I. Equation (4) demonstrates a good agreement with experimental data.

TABLE I. COEFFICIENTS FOR THE ANALYTICAL APPROXIMATIONS

HCT	A_1, S/m	B_1, s^{-1}	A_2, S/m	B_2, $\%^{-1}$	D_2, %
35%	0.405	0.001176	0.489	0.5006	0.1409
45%	0.265	0.001005	0.325	0.5218	0.1538
55%	0.155	0.0007259	0.197	0.5622	0.1833

IV. ESTIMATION OF SEDIMENTATION SPEED

A. Model of Sedimentation

In Fig. 6A we present a simple model of a column of blood during sedimentaion. The blood column has three separate zones: the up zone of pure plasma, the middle part of initial HCT, and the deposit of hematocrit H = 70% at the bottom of column. In reality, the boundaries between zones are slightly blurred.

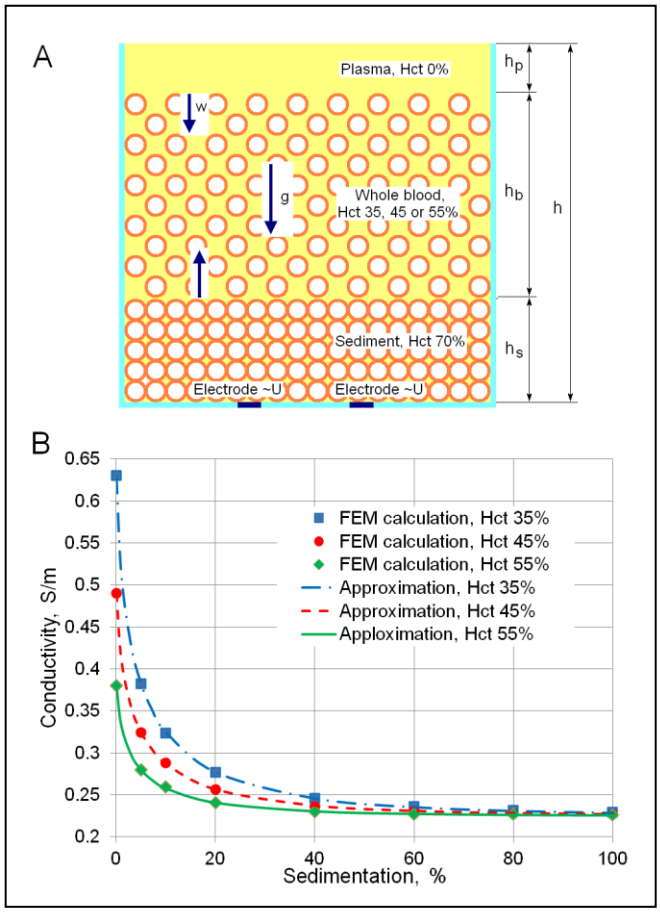

Figure 6. Simple model of RBC sedimentation (A) and approximation of conductivity dependence on sedimentation of blood (B).

We have shown that the blood conductivity only increases slightly during aggregation (see Fig. 3 and 5E). We can therefore assume that a constant electrical conductivity is maintained in the middle part of the blood column during deposition. The height of plasma zone, h_p and the height of sediment, h_s both increase, but the thickness of middle part, h_b decreases over time (Fig. 6A). The total height of the blood column is $h = h_p + h_b + h_s$. We determine the percentage of sedimentation as follows: $S = (h - h_0) / h \times 100\%$. For speed of sedimentation we use a series expansion $v = v_0 + \alpha t$, where v_0 is the initial speed of sedimentation in %/s and α is the acceleration of sedimentation in $\%/s^2$. Acceleration takes place due to aggregation, which increases the mass of the falling particles.

The time dependence of sedimentation is given by:

$$S = v_0 t + at^2/2. \quad (5)$$

The inverse relationship is

$$t = \frac{-v_0 + \sqrt{v_0^2 + 2\alpha S}}{\alpha}. \quad (6)$$

We applied a finite element simulation to calculate dependence of conductivity on sedimentation (Fig. 6B).

After substitution of (6) in (4) we have

$$\sigma(S) = A_2 \exp\left(-B_2\sqrt{D_2 + S}\right) + C_1. \quad (7)$$

where $A_2 = A_1 \exp\left(\frac{B_1 v_0}{\alpha}\right)$, $B_2 = \frac{\sqrt{2}B_1}{\sqrt{\alpha}}$, and $D_2 = \frac{v_0^2}{2\alpha}$.

We obtained the coefficients A_2, B_2, and D_2 obtained by the least square method for different HCT values; these are given in Table I. These coefficients enable the initial speed and the acceleration of sedimentation to be calculated. Their values are given in Table II. Here w_0 is the initial velocity and a is the acceleration of boundary between plasma and blood

TABLE II. INITIAL SPEED, ACCELERATION AND COMPLETION TIME OF RBC SEDIMENTATION

HCT	v_0, %/s	w_0, μm/s	α, $\%/s^2$	a, $\mu m/s^2$	t, s
35%	$1.764 \cdot 10^{-3}$	0.04409	$11.04 \cdot 10^{-6}$	$2.759 \cdot 10^{-4}$	4100
45%	$1.511 \cdot 10^{-3}$	0.02697	$7.419 \cdot 10^{-6}$	$1.325 \cdot 10^{-4}$	4993
55%	$1.106 \cdot 10^{-3}$	0.01184	$3.334 \cdot 10^{-6}$	$3.572 \cdot 10^{-5}$	7421

B. Settling Velocity

For small Reynolds number, Re < 1, the drag force of spherical particle obeys to the Stokes' law:

$$F_D = 6\pi\mu R w, \quad (8)$$

where μ is the dynamic viscosity of the fluid, R is the sphere radius, and w is the mean velocity of the sphere relative to the fluid. If the drag force equals to the gravity force and

buoyancy force, then the resulting terminal velocity, w_t is given by:

$$w_t = 2(\rho_p - \rho_f)R^2 g/9\mu. \quad (9)$$

where ρ_p and ρ_f are the densities of particle and fluid, respectively, g is the gravity acceleration.

Equation (9) indicates that particles with a greater mass will have a higher velocity. The relaxation time of a spherical particle is given by:

$$\tau = 2(\rho_p - \rho_f)R^2/9\mu. \quad (10)$$

A sphere of equivalent volume to a red cell has radius R = 2.78 μm. We can estimate the terminal velocity of individual insulated erythrocyte as w_t = 0.561 μm/s = 2.02 mm/h. The relaxation time of single erythrocyte is τ_{RBC} = 1.34 μs. This relaxation time is very short, compared to the time taken for sedimentation. We therefore conclude that RBCs have a finite initial speed.

A large number of experiments have demonstrated that a dense cloud of particles settling in a fluid has the terminal velocity lower than it is given by the Stokes' law. It has been empirically found that the reduction in terminal velocity mainly depends on the volume fraction of the particles in the system. The semi-empirical Richardson-Zaki equation [21] is one of the most commonly used correction factors:

$$w_s = w_t(1 - \phi_p)^n. \quad (11)$$

where w_s is the settling velocity at a high volumetric concentration of particles, n is an empirically determined exponent. Richardson and Zaki showed that n is a function only of the Reynolds number (in the absence of the wall effects) [21]. The empirical value for the exponent n for low Reynolds number conditions (Re < 0.2) is n = 4.65, and this is the value that we use in our analysis. Calculated settling velocity of erythrocyte sedimentation at different HCT is as follows: $w_s(0\%)$ = 0.415, $w_s(35\%)$ = 0.0599 μm/s, $w_s(45\%)$ = 0.0282, and $w_s(55\%)$ = 0.0114 μm/s. It agrees well with experimental data (see Table II).

V. PARTICLE DYNAMIC SIMULATION OF RBC AGGREGATION AND SEDIMENTATION

A. Elastic and Aggregation Forces between RBCs

Following Fenech et al. [22] we define the elastic and aggregation forces. The elastic force is given by:

$$f_e = \kappa(2R - d_{ij})^{3/2}, \text{ if } d_{ij} < 2R \text{ and 0 otherwise }, \quad (12)$$

where d_{ij} is the distance between the centers of RBCs i and j, κ is the elastic modulus.

The attractive/repulsive Morse potential is:

$$\Phi_{ij} = D\left(e^{2B(\delta_0 - \delta_{ij})} - 2e^{B(\delta_0 - \delta_{ij})}\right), \quad (13)$$

where D is the coefficient of surface energy, $\delta_{ij} = (d_{ij} - 2R)$ is the membrane cell-cell distance, δ_0 is the membrane cell-cell distance for which the attractive/repulsive force is zero.

The aggregation force can be found after differentiation of Morse potential

$$f_a = 2DAB\left(e^{2B(\delta_0 - \delta_{ij})} - e^{B(\delta_0 - \delta_{ij})}\right), \quad (14)$$

where A is the area of RBC interacting surfaces. For our simulations we used the following parameters values: κ = $1.2 \cdot 10^{-6}$ N/m; $\delta_0 = 11 \cdot 10^{-9}$ m; $B = 5 \cdot 10^6$; $DA = 5 \cdot 10^{-24}$ J [22].

For calculation of the hydrodynamic interaction forces between particles we used a method based on Stokesian Dynamics approach [23-25]. We implemented the method [24] to calculate the lubrication forces in simulations of sedimenting particles.

B. Simulation of Aggregation and Sedimentation

Fig. 7 shows the snapshots of RBC motion at first five minutes of deposition at hematocrit H = 45%. Two dimensional aggregation and sedimentation was modeled by spheres of radius R = 2.78 μm to match RBC volume.

We applied periodical boundary conditions in the particle dynamic simulation to consider the middle part of settling particles. In Fig. 7, we show the calculation only with 81 RBCs to make a clear image. The initial positions of RBCs were determined by random placing the spheres in a rectangular cell.

C. Characterization of Settling Particles

Many different ways were suggested for characterization of aggregation: AI, aggregation index; AR, aggregation radius; AAS, average aggregate size; SAF, small aggregate fraction; MAF, medium aggregate fraction; LAF, large aggregate fraction; VR, vacuum radius.

In the left panel of Fig. 7, the number of RBC in aggregate is expressed by gradation of red. The right panel of Fig. 7 indicates the number of neighbours connected with the erythrocyte. The empty circle represents an individual erythrocyte. Yellow, orange, red, and reddish-brown circles indicate that cell is surrounded by 1, 2, 3, and 4 neighbours, respectively. Changes of VR are also given in Fig. 7.

The increase in the average settling velocity at different HCT with time is shown in Fig. 8. One can see a good agreement between calculated and experimental data.

 ISBN: 978-1-61208-214-1

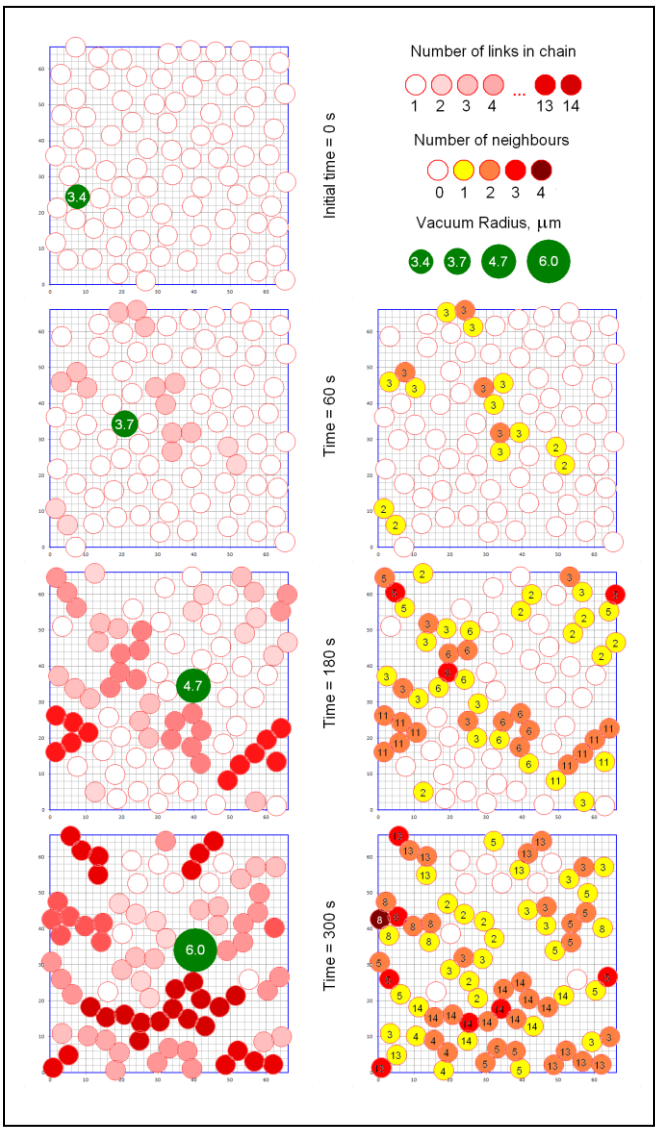

Figure 7. Snapshots of sedimentation and aggregation.

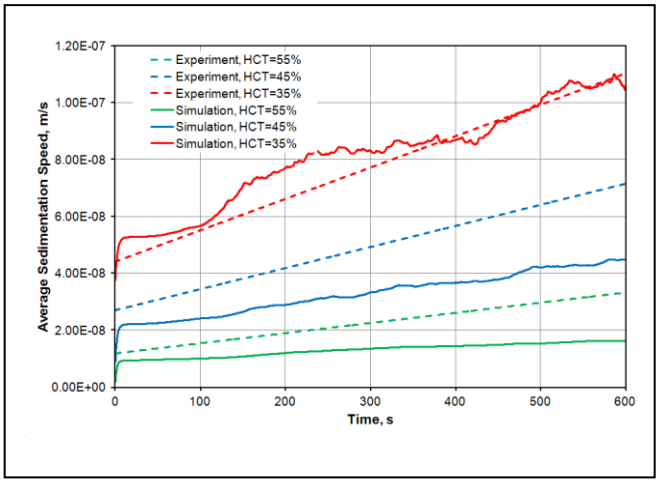

Figure 8. Changes of RBC settling velocity with time.

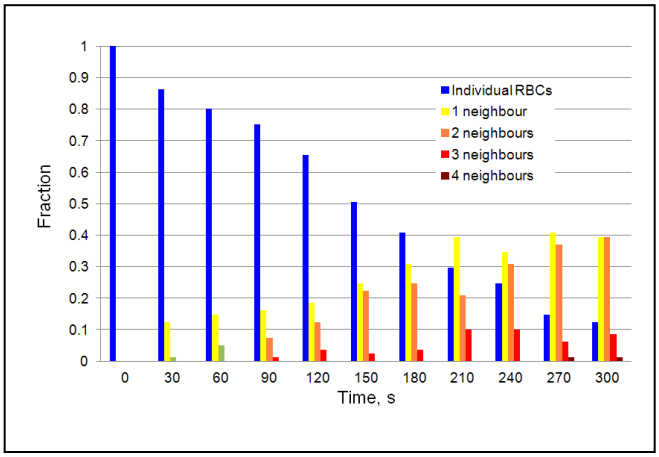

Figure 9. Fraction of particles surrounded by neighbours.

The change in velocity over time is largely dependent on the initial distribution of particles in the computational cell, but on average corresponds to uniformly accelerated motion.

We believe that an important characteristic of the aggregation and sedimentation is the fraction of particles surrounded by different number of neighbours (Fig. 9). We assume that acceleration of settling velocity takes place due to aggregation, which increases the mass of the falling particles.

By comparing Fig. 8 with Fig. 9, it clearly shows that the settling velocity and the number of aggregated particles are strongly related.

Analysis of the simulation also shows that some particles sometimes rise up. We observed the formation and collapse of a RBC networks. The sedimentation rate demonstrates a complex stochastic behavior in time.

VI. CONCLUSION

We studied the changes in blood conductivity during aggregation and sedimentation in a miniature chamber with two planar electrodes on the bottom. The dielectric theory was applied to determine the conductivity of the whole blood. The erythrocytes were modeled as conducting oblate spheroid coated with a thin insulating membrane. The conductivity of erythrocyte rouleaux formations was described by prolate spheroids with different components of conductivity. The experimentally measured conductance of blood in the chamber slightly increases during the first minute of observation and then decreases for more than 1.5 h. We attribute the slight increase in blood conductivity within the first minute to erythrocyte aggregation. Our theoretical calculations predict increase in conductivity with the number of erythrocytes aggregated. The calculation results are in good agreement with experiment. Further

 ISBN: 978-1-61208-214-1

decrease in electrical conductivity is caused by deposition of red cells at the bottom of chamber. We analytically approximated the change in the blood conductivity on time and dependence between conductivity and sedimentation. Using these approximations we estimated the initial velocity and acceleration of erythrocyte sedimentation. A particle dynamic model was developed to investigate the microfluidic RBC interaction. We estimated the initial velocity and acceleration of erythrocytes and completion time of sedimentation. As a result, the relation between the ESR and the blood conductivity was found. It is likely that our method could also be applied to accelerated ESR tests.

ACKNOWLEDGMENT

This work was partially funded by grants from the Ministry of Education, Science and Technology (MEST, KRF-20110028861), World Class University Program (R31-2008-000-10026-0) and the institute of Medical System Engineering (*iMSE*), GIST, Republic of Korea.

REFERENCES

[1] J. M. Jou, S. M. Lewis, C. Briggs, S. H. Lee, B. De La Salle, and S. McFadden, "ICSH review of the measurement of the erythocyte sedimentation rate," Int. J. Lab. Hematol., vol. 33, April 2011, pp. 125-132, doi:10.1111/j.1751-553X.2011.01302.x.

[2] P. Yagupsky and J. E. Bearman, "Shortened erythrocyte sedimentation rate,".Pediatr. Infect. Dis. J., vol. 6, May 1987, pp. 494-495.

[3] T. Alexy, E. Pais, and H. J. Meiselman, "A rapid method to estimate Westergren sedimentation rates," Rev. Sci. Instrum., vol. 80, Sep. 2009, Vol. 80, pp. 096102 (3 pages).

[4] M. Shteinshnaider, D. Almoznino-Sarafian, I. Tzur, S. Berman, N. Cohen, and O. Gorelik, "Shortened erythrocyte sedimentation rate evaluation is applicable to hospitalised patients," Eur. J. Intern. Med., vol. 21, Jun. 2010, pp. 226-229, doi:10.1016/j.ejim.2010.02.002.

[5] A. Pribush, D. Meyerstein, and N. Meyerstein, "The mechanism of erythrocyte sedimentation. Part 1: Channeling in sedimenting blood," Colloid. Surf. B-Biointerfaces, vol. 75, Jan. 2010, pp. 214-223, doi:10.1016/j.colsurfb.2009.08.036.

[6] K. Cha, E. F. Brown, and D. W. Wilmore, "A new bioelectrical impedance method for measurement of the erythrocyte sedimentation rate," Physiol. Meas., vol. 15, Nov. 1994, pp. 499-508, doi:10.1088/0967-3334/15/4/011.

[7] A. Pribush, D. Meyerstein, and N. Meyerstein, "The mechanism of erythrocyte sedimentation. Part 2: The global collapse of settling erythrocyte network," Colloid. Surf. B-Biointerfaces, vol. 75, Jan. 2010, P. 224-229, doi:10.1016/j.colsurfb.2009.08.037.

[8] A. Pribush, L. Hatskelzon, and N. Meyerstein, "A novel approach for assessments of erythrocyte sedimentation rate," Int. J. Lab. Hematol., vol. 33, Jun. 2011, pp. 251-257, doi:10.1111/j.1751-553X.2010.01277.x.

[9] A. Pribush, D. Meyerstein, and N. Meyerstein, "The effect of the prior flow velocity on the structural organization of aggregated erythrocytes in the quiescent blood," Colloid. Surf. B-Biointerfaces, vol. 82, Feb. 2011, pp. 518-525 , doi:10.1016/j.colsurfb.2010.10.010.

[10] http://www.home.agilent.com/agilent/home.jspx

[11] http://www.ni.com/labview/

[12] K. Asami and T. Yonezawa, "Dielectric behavior of non-spherical cells in culture," Biochim. Biophys. Acta, vol. 1245, Dec. 1995, pp. 317-324, doi:10.1016/0304-4165(95)00116-6.

[13] K. Asami, "Characterization of heterogeneous systems by dielectric spectroscopy," Prog. Polym. Sci., vol. 27, Oct. 2002, pp. 1617-1659. doi:10.1016/S0079-6700(02)00015-1.

[14] S. Giordano, "Effective medium theory for dispersions of dielectric ellipsoids," Electrostat., vol. 58, May 2003, pp. 59-76, doi:0.1016/S0304-3886(02)00199-7.

[15] D. A. G. Bruggeman, "Berechnung verschiedener physikalischer Konstanten von heterogenen Substanzen. I. Dielektrizitätskonstanten und Leitfähigkeiten der Mischkörper aus isotropen Substanzen," Ann. Phys.-Berlin, vol. 416, Jul. 1935, pp. 636-664, doi:10.1002/andp.19354160705.

[16] S. Giordano, P. L. Palla, and L. Colombo, "Effective permittivity of materials containing graded ellipsoidal inclusions," Eur. Phys. J. B, vol. 66, Jan. 2008, pp. 29-35, doi:10.1140/epjb/e2008-00382-7.

[17] L. A. Geddes and H. Kidder, "Specific resistance of blood at body temperature II," Med. Biol. Eng. Comput., vol. 14, Mar. 1976, pp. 180-185, doi:10.1007/BF02478745.

[18] S. N. Mohapatra and D. W. Hill, "The Changes in Blood Resistivity with Haematocrit and Temperature," Intensive Care Med., vol. 1, Dec. 1975, pp. 153-162, doi:10.1007/BF00624433.

[19] K. Sandberg, B. A. Sjöqvist, and T. Olsson, "Relation between Blood Resistivity and Hematocrit in Fresh Human Fetal Blood," Pediatr. Res., vol. 15, Jun. 1981, pp. 964-966, doi:10.1203/00006450-198106000-00017.

[20] K.B. Visser, "Electric conductivity of stationary and flowing human blood at low frequencies," Medical and Biological Engineering and Computing, vol. 30, Nov. 1992, pp. 636-640, doi:10.1007/BF02446796.

[21] J. F. Richardson and W.N. Zaki, "Sedimentation and fluidisation: Part I," Trans. Inst. Chem. Engs., vol. 32, 1954, pp. 35-53.

[22] M. Fenech, D. Garcia, H. J. Meiselman, and G. Cloutier, "A particle dynamic model of red blood cell aggregation kinetics," Ann. Biomed. Eng., vol. 37, Nov. 2009, pp. 2299-2309, doi:10.1007/s10439-009-9775-1.

[23] T. Kumagai, "Numerical analysis of equation of motion for a cluster of spheres in fluid at low Reynolds numbers," JSME J. Ser. B, vol. 38, Apr. 1995, pp. 563-569, doi:10.1299/jsmeb.38.563.

[24] C. Vanroyen, A. Omari, J. Toutain, and D. Reungoat, "Interactions between hard spheres sedimenting at low Reynolds number," Eur. J. Mech. B-Fluids, vol. 24, Sep.-Oct. 2005, pp. 586-595, doi:10.1016/j.euromechflu.2005.01.002.

[25] G. C. Abade and F. R. Cunha, "Computer simulation of particle aggregates during sedimentation," Comput. Meth. Appl. Mech. Eng., vol. 196, nos. 45-48, Sep. 2007, pp. 4597-4612, doi:10.1016/j.cma.2007.05.022

 ISBN: 978-1-61208-214-1

Schemes for Deterministic Joint Remotely Preparing an Arbitrary Three-qubit State

You-Bang Zhan[*], Yuan-Shun Cui[&], A-Long Yu[$],
Xiao-Wei Li[§], Gui-Bin Chen[♯]

School of Physics and Electronic Electrical Engineering,
Huaiyin Normal University, Huaian 223300, P. R. China
e-mail: [*] ybzhan@hytc.edu.cn [&] cys571015@hytc.edu.cn [$] yal@hytc.edu.cn
[§] lxw@hytc.edu.cn [♯] gbchen@hytc.edu.cn

***Abstract*—Recently, a new scheme for joint remotely preparing an arbitrary three-qubit state based on two three-qubit projective measurements was proposed. In this paper, we put forward two novel schemes to complete the joint remote preparation for this class of three-qubit state with complex coefficients via three Greenberger-Horne-Zeilinger (GHZ) states as the quantum channel. In the present schemes, two senders share the original state which they wish to help the receiver to remotely prepare. To complete the schemes, some novel sets of mutually orthogonal basis vectors are introduced. It is shown that, only if two senders collaborate with each other, and perform projective measurements under suitable measuring basis and appropriate unitary operations on their own qubits respectively, the receiver can reconstruct the original state. Compared with the previous scheme, the advantage of the present schemes is that the total success probability can reach 1.**

Keywords-joint remote state preparation; arbitrary three-qubit state; three-qubit projective measurement; unit success probability

Ⅰ. INTRODUCTION

In the last decade, Lo [1], Pati [2], and Bennett *et al.* [3] presented a new quantum communication scheme that uses classical communication and a previously shared entangled resource to remotely prepare a quantum state. This communication scheme is called remote state preparation (RSP). Compared with teleportation [4], RSP requires less classical communication cost than teleportation. Since then, various theoretical protocols for generalization of RSP have been proposed and experimental implementations of RSP scheme have been presented [5-22]. One can note easily that the above schemes assume the case that only one sender knows the original state.

Recently, a novel aspect of PSP, called as the joint remote state preparation(JRSP), has been proposed [23-29]. In these schemes of the JRSP [23-29], two senders (or N senders) know partly of original state they want to remotely preparation, respectively. In a recent paper [30], joint remote preparation of an arbitrary three-qubit state with complex coefficients has been proposed. More recently, Chen *et al.* [31] pointed out that the scheme by Luo *et al.* [30] does not work for states with arbitrary complex coefficients, and then proposed a new scheme for JRSP of an arbitrary three-qubit state with complex coefficients via EPR-type pairs [31]. In the scheme [31], the coefficients of the original state are split into two symmetric subsets. For maximally quantum channel, Chen's scheme can be successfully realized only with the probability $\frac{1}{8}$ by two sets of three-qubit orthogonal basis projective measurement.

Now, we re-investigate the joint remote preparation of an arbitrary three-qubit state with complex coefficients. In this paper, two novel JRSP schemes are presented with unit successful probability. For clearly, we only consider maximally entangled channel. In Section 2, we propose the first scheme using three-qubit GHZ states as the quantum channel, and construct two sets of measuring basis which are same as [31]. Different from the Chens' scheme in [31], in our scheme, to acquire unit success probability, the coefficients of the original state are split into two non-symmetric subsets, and after first sender

 ISBN: 978-1-61208-214-1

(Alice) performs her projective measurement, the second sender (Bob) should make a suitable unitary operation on his qubits, and then perform another projective measurement on the qubits, the receiver can recover the original state by appropriate unitary operations, and the total successful probability of JPSP process being 1. In Section 3, we propose the other deterministic JRSP scheme via a novel three-qubit orthogonal basis projective measurement, and the total success probability is still 1. The required classical communication cost of each of these schemes is six bits. Some discussions and conclusions are given in the last Section.

Ⅱ. JRSP VIA TWO THREE-QUBIT PROJECTIVE MEASUREMENTS AND AN UNITARY OPERATION BY TWO SENDERS

Suppose that two senders Alice and Bob wish to help the receiver Charlie remotely prepare the state [31]

$$\begin{aligned}|p\rangle = {} & r_1 e^{i\varphi_1}|000\rangle + r_2 e^{i\varphi_2}|001\rangle + r_3 e^{i\varphi_3}|010\rangle \\ & + r_4 e^{i\varphi_4}|011\rangle + r_5 e^{i\varphi_5}|100\rangle + r_6 e^{i\varphi_6}|101\rangle \\ & + r_7 e^{i\varphi_7}|110\rangle + r_8 e^{i\varphi_8}|111\rangle, \end{aligned} \quad (1)$$

where r_j and φ_j $(j=1,2\cdots,8)$ are real, and $\sum_{j=1}^{8} r_j^2 = 1$. To acquire unit success probability, inspired by the schemes of [22, 32, 33], we assume that Alice and Bob share the state $|p\rangle$ and they know the state partly, *i.e.*, Alice knows r_j $(j=1,2\cdots,8)$, and Bob knows φ_j $(j=1,2\cdots,8)$, but Charlie does not know them at all. This means that the coefficients of the state (1) are split into two non-symmetric subsets, *i.e.*, modulus (r_j) and phase (φ_j) coefficients. We also suppose that the state shared by Alice, Bob, and Charlie as the quantum channel are three GHZ states

$$|\psi_{1(2,3)}\rangle = \frac{1}{\sqrt{2}}(|000\rangle + |111\rangle)_{a_1b_1c_1(a_2b_2c_2, a_3b_3c_3)}, \quad (2)$$

where the qubits a_1, a_2, a_3 belong to Alice, qubits b_1, b_2, b_3 to Bob, and qubits c_1, c_2, c_3 to Charlie, respectively.

In order to complete the JRSP, Alice and Bob should construct their own measuring bases respectively. The first measuring basis chosen by Alice is a set of mutually orthogonal basis vectors (MOBVs) $\{|\mu_k\rangle\}(k=1,2,\cdots,8)$, which is given by

$$\begin{pmatrix} |\mu_1\rangle \\ |\mu_2\rangle \\ |\mu_3\rangle \\ |\mu_4\rangle \\ |\mu_5\rangle \\ |\mu_6\rangle \\ |\mu_7\rangle \\ |\mu_8\rangle \end{pmatrix} = F \begin{pmatrix} |000\rangle \\ |001\rangle \\ |010\rangle \\ |011\rangle \\ |100\rangle \\ |101\rangle \\ |110\rangle \\ |111\rangle \end{pmatrix}, \quad (3)$$

where

$$F = \begin{pmatrix} r_1 & r_2 & r_3 & r_4 & r_5 & r_6 & r_7 & r_8 \\ r_2 & -r_1 & r_4 & -r_3 & r_6 & -r_5 & r_8 & -r_7 \\ r_3 & -r_4 & -r_1 & r_2 & -r_7 & r_8 & r_5 & -r_6 \\ r_4 & r_3 & -r_2 & -r_1 & r_8 & r_7 & -r_6 & -r_5 \\ r_5 & -r_6 & r_7 & -r_8 & -r_1 & r_2 & -r_3 & r_4 \\ r_6 & r_5 & -r_8 & -r_7 & -r_2 & -r_1 & r_4 & r_3 \\ r_7 & -r_8 & -r_5 & r_6 & r_3 & -r_4 & -r_1 & r_2 \\ r_8 & r_7 & r_6 & r_5 & -r_4 & -r_3 & -r_2 & -r_1 \end{pmatrix}. \quad (4)$$

The second measuring basis chosen by Bob is a set of MOBVs $\{|\tau_m\rangle\}(m=1,2,\cdots,8)$, which is given by

$$\begin{pmatrix} |\tau_1\rangle \\ |\tau_2\rangle \\ |\tau_3\rangle \\ |\tau_4\rangle \\ |\tau_5\rangle \\ |\tau_6\rangle \\ |\tau_7\rangle \\ |\tau_8\rangle \end{pmatrix} = \frac{1}{2\sqrt{2}} G \begin{pmatrix} |000\rangle \\ |001\rangle \\ |010\rangle \\ |011\rangle \\ |100\rangle \\ |101\rangle \\ |110\rangle \\ |111\rangle \end{pmatrix}, \quad (5)$$

where

$$G = \begin{pmatrix} x_1 & x_2 & x_3 & x_4 & x_5 & x_6 & x_7 & x_8 \\ x_1 & -x_2 & x_3 & -x_4 & x_5 & -x_6 & x_7 & -x_8 \\ x_1 & -x_2 & -x_3 & x_4 & -x_5 & x_6 & x_7 & -x_8 \\ x_1 & x_2 & -x_3 & -x_4 & x_5 & x_6 & -x_7 & -x_8 \\ x_1 & -x_2 & x_3 & -x_4 & -x_5 & x_6 & -x_7 & x_8 \\ x_1 & x_2 & -x_3 & -x_4 & -x_5 & -x_6 & x_7 & x_8 \\ x_1 & -x_2 & -x_3 & x_4 & x_5 & -x_6 & -x_7 & x_8 \\ x_1 & x_2 & x_3 & x_4 & -x_5 & -x_6 & -x_7 & -x_8 \end{pmatrix}, \quad (6)$$

where $x_j = e^{-i\varphi_j} (j = 1, 2 \cdots, 8)$.

Now, let Alice perform three-qubit projective measurement on the qubits a_1, a_2, a_3 by using the basis $\{|\mu_k\rangle\}(k = 1, 2, \cdots, 8)$ and publicly announces her measurement result. Next, according to Alice's result of measurement, Bob first makes a suitable unitary operation U_B on his qubits b_1, b_2, b_3, then he should perform three-qubit projective measurement on the qubits b_1, b_2, b_3 under the basis $\{|\tau_m\rangle\}(m = 1, 2, \cdots, 8)$. After these measurements, Alice and Bob inform Charlie of their outcomes of measurement by the classical channel. In accord with Alice's and Bob's results, Charlie can reconstruct the original state $|p\rangle$ by appropriate unitary operation. For instance, without loss of generality, assume Alice's result of measurement is $|\mu_3\rangle_{a_1 a_2 a_3}$, the qubits $b_1, c_1, b_2, c_2, b_3, c_3$ will collapse into the state

$$\begin{aligned} |\phi\rangle = \frac{1}{2\sqrt{2}} (& r_3 |000000\rangle - r_4 |000011\rangle - r_1 |001100\rangle \\ & + r_2 |001111\rangle - r_7 |110000\rangle + r_8 |110011\rangle \\ & + r_5 |111100\rangle - r_6 |111111\rangle)_{b_1 c_1 b_2 c_2 b_3 c_3}. \end{aligned} \quad (7)$$

According to Alice's announcement, Bob should make an unitary operation $U_B = (\sigma_z)_{b_1} \otimes (-i\sigma_y)_{b_2} \otimes (\sigma_z)_{b_3}$ on his qubits b_1, b_2, b_3, the state (7) will become

TABLE 1: Corresponding relation between the measurement results (*MR*) of Alice and the local unitary operations U_B performed by Bob.

MR	U_B
$\|\mu_1\rangle_{a_1 a_2 a_3}$	$(I)_{b_1} \otimes (I)_{b_2} \otimes (I)_{b_3}$
$\|\mu_2\rangle_{a_1 a_2 a_3}$	$(I)_{b_1} \otimes (I)_{b_2} \otimes (-i\sigma_y)_{b_3}$
$\|\mu_3\rangle_{a_1 a_2 a_3}$	$(\sigma_z)_{b_1} \otimes (-i\sigma_y)_{b_2} \otimes (\sigma_z)_{b_3}$
$\|\mu_4\rangle_{a_1 a_2 a_3}$	$(I)_{b_1} \otimes (-i\sigma_y)_{b_2} \otimes (\sigma_x)_{b_3}$
$\|\mu_5\rangle_{a_1 a_2 a_3}$	$(-i\sigma_y)_{b_1} \otimes (I)_{b_2} \otimes (\sigma_z)_{b_3}$
$\|\mu_6\rangle_{a_1 a_2 a_3}$	$(-i\sigma_y)_{b_1} \otimes (\sigma_z)_{b_2} \otimes (\sigma_x)_{b_3}$
$\|\mu_7\rangle_{a_1 a_2 a_3}$	$(\sigma_x)_{b_1} \otimes (-i\sigma_y)_{b_2} \otimes (\sigma_z)_{b_3}$
$\|\mu_8\rangle_{a_1 a_2 a_3}$	$(-i\sigma_y)_{b_1} \otimes (\sigma_x)_{b_2} \otimes (\sigma_x)_{b_3}$

$$\begin{aligned} |\phi'\rangle = \frac{1}{2\sqrt{2}} (& r_1 |000100\rangle + r_2 |000111\rangle + r_3 |001000\rangle \\ & + r_4 |001011\rangle + r_5 |110100\rangle + r_6 |110111\rangle \\ & + r_7 |111000\rangle + r_8 |111011\rangle)_{b_1 c_1 b_2 c_2 b_3 c_3}. \end{aligned} \quad (8)$$

Then, Bob measures his qubits b_1, b_2, b_3 in the basis $\{|\tau_m\rangle\}(m = 1, 2, \cdots, 8),$ and informs Charlie of his result by the classical channel. Assume Bob's results of measurement is $|\tau_2\rangle_{b_1 b_2 b_3}$, the state of qubits c_1, c_2, c_3

will collapse into the state

$$\begin{aligned}|\varphi\rangle = \frac{1}{8}(& r_1 e^{i\varphi_1}|010\rangle - r_2 e^{i\varphi_2}|011\rangle + r_3 e^{i\varphi_3}|000\rangle \\ & - r_4 e^{i\varphi_4}|001\rangle + r_5 e^{i\varphi_5}|110\rangle - r_6 e^{i\varphi_6}|111\rangle \\ & + r_7 e^{i\varphi_7}|100\rangle - r_8 e^{i\varphi_8}|101\rangle). \end{aligned} \quad (9)$$

In accord with Alice's and Bob's outcomes, Charlie can perform an unitary operation $U_C = (I)_{c_1} \otimes (\sigma_x)_{c_2} \otimes (\sigma_z)_{c_3}$ on qubits c_1, c_2 and c_3, and the original state $|p\rangle$ can be recovered. If Alice's measurement results are the other 7 cases, Bob should perform the appropriate unitary operation on the qubits b_1, b_2, b_3 and then measure these qubits in the basis $\{|\tau_m\rangle\}$. The relation between the results obtained by Alice and the appropriate unitary transformation performed by Bob is shown in the Table 1. It is easily found that, for all the 64 measurement outcomes of Alice and Bob, the receiver Charlie can reconstruct the original state $|p\rangle$ and the total successful probability of the present JRSP process being 1. So, our scheme is deterministic. It requires classical communication cost is six bits in this scheme.

III. JRSP VIA TWO THREE-QUBIT PROJECTIVE MEASUREMENTS BY TWO SENDERS

Now, let us further propose the scheme for remote preparation of an arbitrary three-qubit state by only two three-qubit projective measurements. Assume the state that Alice and Bob wish to help the receiver Charlie remotely prepare is still in state $|p\rangle$ (see (1)), and the quantum channel shared by Alice, Bob and Charlie is still in states (2).

In order to realize the JRSP, two senders need to construct their own measuring bases respectively. The first measuring basis chosen by Alice is still in a set (3). The second measuring bases by Bob are eight sets of MOBVs $\{|\eta_m^{(k)}\rangle\}$, which are given by

$$\begin{pmatrix} |\eta_1^{(k)}\rangle \\ |\eta_2^{(k)}\rangle \\ |\eta_3^{(k)}\rangle \\ |\eta_4^{(k)}\rangle \\ |\eta_5^{(k)}\rangle \\ |\eta_6^{(k)}\rangle \\ |\eta_7^{(k)}\rangle \\ |\eta_8^{(k)}\rangle \end{pmatrix} = \frac{1}{2\sqrt{2}} H^{(k)} \begin{pmatrix} |000\rangle \\ |001\rangle \\ |010\rangle \\ |011\rangle \\ |100\rangle \\ |101\rangle \\ |110\rangle \\ |111\rangle \end{pmatrix}, \quad (10)$$

where $k = 1, 2, \cdots, 8$, and $H^{(k)}$ are 8×8 matrices given in appendix.

Alice first performs the three-qubit projective measurements on her qubits a_1, a_2, a_3 under the basis $\{|\mu_k\rangle\}$ (see Eqs. (3)) and publicly announces her outcomes of measurement. In accord with Alice's result, Bob should choose suitable measuring basis in the MOBVs $\{|\eta_m^{(k)}\rangle\}$ to measure his qubits b_1, b_2, b_3 and then inform Charlie of his result of measurement by the classical channel. According to Alice's and Bob's outcomes, Charlie can reconstruct the original state $|p\rangle$ by appropriate unitary operation. For example, without loss of generality, assume Alice's measurement result is $|\mu_2\rangle_{a_1 a_2 a_3}$, then Bob should choose measuring basis $\{|\eta_m^{(2)}\rangle\}$ (see Eq.(10) and the Appendix), which is given by

$$\begin{pmatrix} |\eta_1^{(2)}\rangle \\ |\eta_2^{(2)}\rangle \\ |\eta_3^{(2)}\rangle \\ |\eta_4^{(2)}\rangle \\ |\eta_5^{(2)}\rangle \\ |\eta_6^{(2)}\rangle \\ |\eta_7^{(2)}\rangle \\ |\eta_8^{(2)}\rangle \end{pmatrix} = \frac{1}{2\sqrt{2}} H^{(2)} \begin{pmatrix} |000\rangle \\ |001\rangle \\ |010\rangle \\ |011\rangle \\ |100\rangle \\ |101\rangle \\ |110\rangle \\ |111\rangle \end{pmatrix}, \quad (11)$$

 ISBN: 978-1-61208-214-1

where

$$H^{(2)}=\begin{pmatrix} x_2 & x_1 & x_4 & x_3 & x_6 & x_5 & x_8 & x_7 \\ x_2 & -x_1 & x_4 & -x_3 & x_6 & -x_5 & x_8 & -x_7 \\ x_2 & -x_1 & -x_4 & x_3 & -x_6 & x_5 & x_8 & -x_7 \\ x_2 & x_1 & -x_4 & -x_3 & x_6 & x_5 & -x_8 & -x_7 \\ x_2 & -x_1 & x_4 & -x_3 & -x_6 & x_5 & -x_8 & x_7 \\ x_2 & x_1 & -x_4 & -x_3 & -x_6 & -x_5 & x_8 & x_7 \\ x_2 & -x_1 & -x_4 & x_3 & x_6 & -x_5 & -x_8 & x_7 \\ x_2 & x_1 & x_4 & x_3 & -x_6 & -x_5 & -x_8 & -x_7 \end{pmatrix}, \quad (12)$$

(here $x_j = e^{-i\varphi_j}$, $j = 1,2,\cdots,8$), to measure the qubits b_1, b_2, b_3. After these measurements, Alice and Bob inform Charlie of their outcomes by the classical channel. If Bob's measurement result is $\left|\eta_4^{(2)}\right\rangle_{b_1b_2b_3}$, the qubits c_1, c_2, c_3 will collapse into the state

$$\begin{aligned}\left|\psi\right\rangle = \frac{1}{8}(&r_2 e^{i\varphi_2}\left|000\right\rangle + r_1 e^{i\varphi_1}\left|001\right\rangle - r_4 e^{i\varphi_4}\left|010\right\rangle \\ &- r_3 e^{i\varphi_3}\left|011\right\rangle - r_6 e^{i\varphi_6}\left|100\right\rangle - r_5 e^{i\varphi_5}\left|101\right\rangle \\ &+ r_8 e^{i\varphi_8}\left|110\right\rangle + r_7 e^{i\varphi_7}\left|111\right\rangle)_{c_1c_2c_3}. \end{aligned} \quad (13)$$

According to Alice's and Bob's public announcements, Charlie can perform the local unitary operation $(\sigma_z)_{c_1} \otimes (\sigma_z)_{c_2} \otimes (\sigma_x)_{c_3}$ on his qubits c_1, c_2 and c_3, and the original state $\left|p\right\rangle$ can be recovered. If Alice's measurement results are the other 7 cases in the basis $\{\left|\mu_k\right\rangle\}(k = 1,2,\cdots,8)$, Bob should choose appropriate measuring bases $\{\left|\eta_m^{(k)}\right\rangle\}(k = 1,2,\cdots,8)$ to measure his qubits b_1, b_2 and b_3, then Charlie can recover the original state $\left|p\right\rangle$ by suitable unitary operations. Here we no longer depict them one by one. The corresponding relation of Alice's measurement result $\left|\mu_k\right\rangle_{a_1a_2a_3}$ and the measuring basis $\{\left|\eta_m^{(k)}\right\rangle\}$ performed by Bob can be described explicitly as

$$\begin{aligned} &\left|\mu_1\right\rangle_{a_1a_2a_3} \to \{\left|\eta_m^{(1)}\right\rangle\}, \quad \left|\mu_2\right\rangle_{a_1a_2a_3} \to \{\left|\eta_m^{(2)}\right\rangle\}, \\ &\left|\mu_3\right\rangle_{a_1a_2a_3} \to \{\left|\eta_m^{(3)}\right\rangle\}, \quad \left|\mu_4\right\rangle_{a_1a_2a_3} \to \{\left|\eta_m^{(4)}\right\rangle\}, \\ &\left|\mu_5\right\rangle_{a_1a_2a_3} \to \{\left|\eta_m^{(5)}\right\rangle\}, \quad \left|\mu_6\right\rangle_{a_1a_2a_3} \to \{\left|\eta_m^{(6)}\right\rangle\}, \\ &\left|\mu_7\right\rangle_{a_1a_2a_3} \to \{\left|\eta_m^{(7)}\right\rangle\}, \quad \left|\mu_8\right\rangle_{a_1a_2a_3} \to \{\left|\eta_m^{(8)}\right\rangle\}, \end{aligned} \quad (14)$$

where $m = 1,2,\cdots,8$. It is easily found that for all the 512 measurement outcomes of Alice and Bob, the receiver Charlie can reconstruct the original state $\left|p\right\rangle$, and the total successful probability *P* is

$$P = 512 \times \frac{1}{8} \times \frac{1}{64} = 1. \quad (15)$$

So, the JRSP scheme is also deterministic. The required classical communication cost is six bits.

Ⅳ.CONCLUSION

In conclusion, we have presented two novel schemes for joint remote preparation of an arbitrary three-qubit states with complex coefficients. In these schemes, two senders share the arbitrary three-qubit states, but each sender only partly knows the state, and two three-qubit GHZ states are exploited as the quantum channel. To complete the JRSP schemes, some novel sets of three-qubit mutually orthogonal basis vectors have been introduced. In the first scheme, the first sender performs a three-qubit projective measurement on her qubits. According to the measurement result of the first sender, the second sender should perform a suitable unitary operation on his qubits, then makes another three-qubit projective measurement on those qubits. In accord with the measurement outcomes of two senders, the receiver can reconstruct the original state by appropriate unitary operation. Next, we have proposed second scheme for JRSP of arbitrary three-qubit state with two senders. In

 ISBN: 978-1-61208-214-1

this scheme, the first sender performs a three-qubit projective measurement on her qubits and the measuring basis is still in Section 2. Different from the scheme in Section 2, according to measurement result of first sender, the second sender should choose one of the novel eight sets of the measuring basis to measure his qubits. After these projective measurements by two senders, the original state can be recovered by the receiver. Compared with the previous scheme of JRSP in [31], the advantage of the present schemes is that the total success probability can reach 1. Thus, our present schemes are useful in expanding RSP field in quantum information science.

REFERENCES

[1] K. H. Lo, “Classical-communication cost in distributed quantum-information processing: A generalization of quantum-communication complexity" Phys. Rev. A, vol. 62, 2000, 012313, doi: 10.1013/PhysRevA. 62. 012313.

[2] A. K. Pati, “Minimun classical bit for remote preparation and measurement of a qubit" Phys. Rev. A, vol. 63, 2001, 014302, doi: 10.1013/PhysRevA. 63. 014302.

[3] C. H. Bennett, D. P. Divincenzo, P. W. Shor, J. A. Smolin, B. M. Terhal, and W. K. Wootters, “Remote state preparation" Phys. Rev. Lett., vol. 87, 2001, 077902, doi: 10.1013/PhysRevLett. 87. 077902.

[4] C. H. Bennett, G. Brassard, C. Crepeau, R. Jozsa, A. Peres, and W. K. Wootters, “Teleporating an unknown quantum state via dual classical and Einstein-Podolsky -Rosen channels" Phys. Rev. Lett., vol. 70, 1993, pp. 1895-1899, doi: 10.1013/PhysRev Lett. 70. 1895.

[5] I. Devetak and T. Berger, “Low-entanglement remote state preparation" Phys. Rev. Lett., vol. 87, 2001, 197901, doi: 10.1013/PhysRevLett. 87. 197901.

[6] B. Zeng and P. Zhang, “Remote-state preparation in higher dimension and the parallelizeable manifold S^{n-1}" Phys. Rev. A, vol. 65, 2002, 022316, doi: 10.1013 /PhysRevA. 65. 022316.

[7] D. W. Berry and B. C. Sanders, “Optimal remote state preparation" Phys. Rev. Lett., vol. 90, 2003, 057901, doi: 10.1013/PhysRevLett. 90. 057901.

[8] A. Abeyesinghe and P. Hayden, “Generalized remote state preparation: trading cbits, qubits, and ebits in quantum communication" Phys.Rev. A, vol. 68, 2003, 062319, doi: 10.1013/PhysRevA. 68. 062319.

[9] D. W.Leung and P. W. Shor, “Oblivious remote state preparation" Phys. Rev. Lett., vol. 90, 2003, 127905, doi: 10.1013/PhysRev
Lett. 90. 127905.

[10] M. G. A. Paris, M. Cola, and R. Bonifacio, “Remote state preparation and teleportation in phase space " J.Opt.B: Quantum Semiclass. Opt., vol. 5, 2003, pp. S360-S364, doi: 10.1088/ 1464-4266/5/3/370.

[11] M. Y. Ye , Y. S. Zhang, and G. C. Guo, “Faithful remote state preparation using finite classical bits and a nonmaximally entangled state” Phys. Rev. A, vol. 69, 2004, pp. 022310, doi: 10.1013/PhysRevA. 69. 022310.

[12] A. Hayashi, T. Hashimoto, and M. Horibe, “Remote state preparation without oblivious conditions” Phys. Rev. A, vol. 67, 2003, 052302, doi: 10.1013/ PhysRevA. 67. 052302.

[13] Z. Kurucz, P. Adam, Z. Kis, and J. Janszky, “Continous variable remote state preparation” Phys.Rev. A, vol. 72, 2005, 052315, doi: 10.1013 /PhysRevA.72. 052315.

[14] J. M. Liu, X. L. Feng, and C. H. Oh, “Remote preparation of arbitrary two- and three-qubit states” EPL, vol. 87, 2009, 30006, doi: 10.1209/0295-5075/87/30006.

[15] P. C. Ma and Y. B. Zhan, “Scheme for remotely preparing a four-particle entangeld cluster-type state” Opt.Commun., vol. 283, 2010, pp. 2640-2643, doi: 10.1016/j.optcom 2010. 02. 034.

[16] M. X. Luo, X. B. Chen, S. Y. Ma, Y. X. Yang, and Z. M. Hu, “Deterministic remote preparation of an arbitrary W-class state with multiparty" J. Phys. B: At.Mol.Opt.Phys., vol. 43, 2010, 065501, doi: 10.1088/0953-0475/43/6/065501.

[17] X. H. Peng, X. W. Zhu, X. M. Fang, M. Feng, M. L. Liu, and K. L. Gao,“Experimental implementation of remote state preparation by nuclear magnetic resonance” Phys. Lett. A, vol. 306, 2003, pp. 271-276, doi: 10.1016/S0375-9601(02) 01604-3.

[18] S. A. Babichev, B. Brezger, and A. I. Lvovsky,

 ISBN: 978-1-61208-214-1

"Remote preparation of a single-mode photonic qubit by measuring field quadrature noise" Phys. Rev. Lett., vol. 92, 2004, 047903, doi: 10.1013 /PhysRev Lett. 92.047903.

[19] G. Y. Xiang, J. Li, B. Yu, and G. C. Guo, "Remote preparation of mixed states via noisy entanglement" Phys. Rev. A, vol. 72, 2005, 012315, doi: 10.1013/PhysRevA. 72. 012315.

[20] N. A. Peters, J. T. Barreiro, M. E. Goggin, T. C. Wei, and P. G. Kwiat, "Remote state preparation: arbitrary remote control of photon polarization" Phys. Rev. Lett., vol. 94, 2005, 150502, doi: 10.1013/PhysRevLett. 94. 150502.

[21] W. Rosenfeld, S. Berner, J. Volz, M. Weber, and H. Weinfurter, "Remote preparation of an atomic quantum memory" Phys. Rev.Lett., vol. 98, 2007, 050504, doi: 10.1013/PhysRevLett. 98. 050504.

[22] M. Y. Wang and F. L. Yan, "Two-step deterministic remote preparation of an arbitrary quantum state" Commun.Theor.Phys., vol. 54, 2010, pp. 792-796, doi: 10.1088/0253-6102/54/5/03.

[23] Y. Xia, J. Song, and H. S. Song, "multiparty remote state preparation" J. Phys. B: At.Mol.Opt.Phys., vol. 40, 2007, pp. 3719-3724, doi: 10.1088/0953-4075/40/18/011.

[24] N. B. An and J. Kim, "Joint remote state preparation" J. Phys. B: At.Mol.Opt.Phys., vol. 41, 2008, 095501, doi: 10.1088/0953 -4075/41/9 /095501.

[25] N. B. An and J. Kim, "Collective remote statepreparation" Int. J. Quantum. Inf., vol. 6, 2008, pp. 1051-1066, doi: 10.1142 /s0219749908004304.

[26] K. Hou, J. Wang, Y. L. Lu, and S. H. Shi, "Joint remote preparation of a multipartite GHZ-class state" Inter. J. Theor. Phys., vol. 48, 2009, pp. 2005-2015, doi: 10.1007/s10073-009 -9975-3.

[27] N. B. An, "Joint remote preparation of a general two-qubit state" J. Phys. B: At.Mol.Opt.Phys., vol. 42, 2009, 125501, doi: 10.1088 /0953-4075/42/12 /125501.

[28] Q. Q. Chen, Y. Xia, J. Song, and N. B. An, "Joint remote state preparation of a W-type state via W-type states" Phys. Lett. A, vol.374, 2010, pp. 4483-4487，doi: 10.1016 /j.physleta. 2010.09.013.

[29] N. B. An, "Joint remote state preparation via W and W-type states" Opt. Commun., vol. 283, 2010, pp. 4113-4117, doi: 10.1016/j.optcom.2010.06.016.

[30] M. X. Luo, X. B. Chen, S. Y. Ma, X. X. Niu, and Y. X. Yang, "Joint remote preparation of an arbitrary three-qubit state" Opt. Commun., vol. 283, 2010, pp. 4796-4801, doi: 10.1016/j.optcom .2010.07.043.

[31] Q. Q. Chen, Y. Xia, and N. B. An, "Joint remote preparation of an arbitrary three-qubit state via EPR-type pairs" Opt. Commun., vol. 284, 2011, pp. 2617-2601, doi: 10.1016/j.optcom. 2011.01.033.

[32] X. Q. Xiao, J. M. Liu, and G. H. Zeng, "Joint remote state preparation of arbitrary two- and three-qubit states" J. Phys. B: At.Mol.Opt.Phys., vol. 44, 2011, 075501, doi: 10.1088/0953 -4075/44/7/075501.

[33] N. B. An, C. T. Bich, and N. V. Don, "Deterministic joint remote state preparation" Phys. Lett. A, vol. 375, 2011, pp. 3570-3573, doi: 10.1016/j.physleta. 2011.08.045.

Appendix

The matrices $H^{(k)}(k=1,2,\cdots,8)$ in Eq.(10) are of the form

$$H^{(1)}=\begin{pmatrix} x_1 & x_2 & x_3 & x_4 & x_5 & x_6 & x_7 & x_8 \\ x_1 & -x_2 & x_3 & -x_4 & x_5 & -x_6 & x_7 & -x_8 \\ x_1 & -x_2 & -x_3 & x_4 & -x_5 & x_6 & x_7 & -x_8 \\ x_1 & x_2 & -x_3 & -x_4 & x_5 & x_6 & -x_7 & -x_8 \\ x_1 & -x_2 & x_3 & -x_4 & -x_5 & x_6 & -x_7 & x_8 \\ x_1 & x_2 & -x_3 & -x_4 & -x_5 & -x_6 & x_7 & x_8 \\ x_1 & -x_2 & -x_3 & x_4 & x_5 & -x_6 & -x_7 & x_8 \\ x_1 & x_2 & x_3 & x_4 & -x_5 & -x_6 & -x_7 & -x_8 \end{pmatrix}, \quad (A.1)$$

$$H^{(2)} = \begin{pmatrix} x_2 & x_1 & x_4 & x_3 & x_6 & x_5 & x_8 & x_7 \\ x_2 & -x_1 & x_4 & -x_3 & x_6 & -x_5 & x_8 & -x_7 \\ x_2 & -x_1 & -x_4 & x_3 & -x_6 & x_5 & x_8 & -x_7 \\ x_2 & x_1 & -x_4 & -x_3 & x_6 & x_5 & -x_8 & -x_7 \\ x_2 & -x_1 & x_4 & -x_3 & -x_6 & x_5 & -x_8 & x_7 \\ x_2 & x_1 & -x_4 & -x_3 & -x_6 & -x_5 & x_8 & x_7 \\ x_2 & -x_1 & -x_4 & x_3 & x_6 & -x_5 & -x_8 & x_7 \\ x_2 & x_1 & x_4 & x_3 & -x_6 & -x_5 & -x_8 & -x_7 \end{pmatrix}, \quad (A.2)$$

$$H^{(3)} = \begin{pmatrix} x_3 & x_4 & x_1 & x_2 & x_7 & x_8 & x_5 & x_6 \\ x_3 & -x_4 & x_1 & -x_2 & x_7 & -x_8 & x_5 & -x_6 \\ x_3 & -x_4 & -x_1 & x_2 & -x_7 & x_8 & -x_5 & -x_6 \\ x_3 & x_4 & -x_1 & -x_2 & x_7 & x_8 & -x_5 & -x_6 \\ x_3 & -x_4 & x_1 & -x_2 & -x_7 & x_8 & x_5 & x_6 \\ x_3 & x_4 & -x_1 & -x_2 & -x_7 & -x_8 & x_5 & x_6 \\ x_3 & -x_4 & -x_1 & x_2 & x_7 & -x_8 & -x_5 & x_6 \\ x_3 & x_4 & x_1 & x_2 & -x_7 & -x_8 & -x_5 & -x_6 \end{pmatrix}, \quad (A.3)$$

$$H^{(4)} = \begin{pmatrix} x_4 & x_3 & x_2 & x_1 & x_8 & x_7 & x_6 & x_5 \\ x_4 & -x_3 & x_2 & -x_1 & x_8 & -x_7 & x_6 & -x_5 \\ x_4 & -x_3 & -x_2 & x_1 & -x_8 & x_7 & -x_6 & -x_5 \\ x_4 & x_3 & -x_2 & -x_1 & x_8 & x_7 & -x_6 & -x_5 \\ x_4 & -x_3 & x_2 & -x_1 & -x_8 & x_7 & x_6 & x_5 \\ x_4 & x_3 & -x_2 & -x_1 & -x_8 & -x_7 & x_6 & x_5 \\ x_4 & -x_3 & -x_2 & x_1 & x_8 & -x_7 & -x_6 & x_5 \\ x_4 & x_3 & x_2 & x_1 & -x_8 & -x_7 & -x_6 & -x_5 \end{pmatrix}, \quad (A.4)$$

$$H^{(5)} = \begin{pmatrix} x_5 & x_6 & x_7 & x_8 & x_1 & x_2 & x_3 & x_4 \\ x_5 & -x_6 & x_7 & -x_8 & x_1 & -x_2 & x_3 & -x_4 \\ x_5 & -x_6 & -x_7 & x_8 & -x_1 & x_2 & -x_3 & -x_4 \\ x_5 & x_6 & -x_7 & -x_8 & x_1 & x_2 & -x_3 & -x_4 \\ x_5 & -x_6 & x_7 & -x_8 & -x_1 & x_2 & x_3 & x_4 \\ x_5 & x_6 & -x_7 & -x_8 & -x_1 & -x_2 & x_3 & x_4 \\ x_5 & -x_6 & -x_7 & x_8 & x_1 & -x_2 & -x_3 & x_4 \\ x_5 & x_6 & x_7 & x_8 & -x_1 & -x_2 & -x_3 & -x_4 \end{pmatrix}, \quad (A.5)$$

where $x_j = e^{-i\varphi_j}$ $(j = 1, 2, \cdots, 8)$.

$$H^{(6)} = \begin{pmatrix} x_6 & x_5 & x_8 & x_7 & x_2 & x_1 & x_4 & x_3 \\ x_6 & -x_5 & x_8 & -x_7 & x_2 & -x_1 & x_4 & -x_3 \\ x_6 & -x_5 & -x_8 & x_7 & -x_2 & x_1 & -x_4 & -x_3 \\ x_6 & x_5 & -x_8 & -x_7 & x_2 & x_1 & -x_4 & -x_3 \\ x_6 & -x_5 & x_8 & -x_7 & -x_2 & x_1 & x_4 & x_3 \\ x_6 & x_5 & -x_8 & -x_7 & -x_2 & -x_1 & x_4 & x_3 \\ x_6 & -x_5 & -x_8 & x_7 & x_2 & -x_1 & -x_4 & x_3 \\ x_6 & x_5 & x_8 & x_7 & -x_2 & -x_1 & -x_4 & -x_3 \end{pmatrix}, \quad (A.6)$$

$$H^{(7)} = \begin{pmatrix} x_7 & x_8 & x_5 & x_6 & x_3 & x_4 & x_1 & x_2 \\ x_7 & -x_8 & x_5 & -x_6 & x_3 & -x_4 & x_1 & -x_2 \\ x_7 & -x_8 & -x_5 & x_6 & -x_3 & x_4 & -x_1 & -x_2 \\ x_7 & x_8 & -x_5 & -x_6 & x_3 & x_4 & -x_1 & -x_2 \\ x_7 & -x_8 & x_5 & -x_6 & -x_3 & x_4 & x_1 & x_2 \\ x_7 & x_8 & -x_5 & -x_6 & -x_3 & -x_4 & x_1 & x_2 \\ x_7 & -x_8 & -x_5 & x_6 & x_3 & -x_4 & -x_1 & x_2 \\ x_7 & x_8 & x_5 & x_6 & -x_3 & -x_4 & -x_1 & -x_2 \end{pmatrix}, \quad (A.7)$$

$$H^{(8)} = \begin{pmatrix} x_8 & x_7 & x_6 & x_5 & x_4 & x_3 & x_2 & x_1 \\ x_8 & -x_7 & x_6 & -x_5 & x_4 & -x_3 & x_2 & -x_1 \\ x_8 & -x_7 & -x_6 & x_5 & -x_4 & x_3 & -x_2 & -x_1 \\ x_8 & x_7 & -x_6 & -x_5 & x_4 & x_3 & -x_2 & -x_1 \\ x_8 & -x_7 & x_6 & -x_5 & -x_4 & x_3 & x_2 & x_1 \\ x_8 & x_7 & -x_6 & -x_5 & -x_4 & -x_3 & x_2 & x_1 \\ x_8 & -x_7 & -x_6 & x_5 & x_4 & -x_3 & -x_2 & x_1 \\ x_8 & x_7 & x_6 & x_5 & -x_4 & -x_3 & -x_2 & -x_1 \end{pmatrix}, \quad (A.8)$$

 ISBN: 978-1-61208-214-1

Quantum Interference in Cognition: Structural Aspects of the Brain

Diederik Aerts, Sandro Sozzo
Center Leo Apostel for Interdisciplinary Studies
Brussels Free University
Krijgskunderstraat 33, B-1160 Brussels, Belgium
diraerts@vub.ac.be, ssozzo@vub.ac.be

***Abstract*—We identify the presence of typically quantum effects, namely superposition and interference, in what happens when human concepts are combined, and provide a quantum model in complex Hilbert space that represents faithfully experimental data measuring the situation of combining concepts. Our model shows how 'interference of concepts' describes the effects of underextension and overextension when two concepts combine to the disjunction of these two concepts. This result supports our earlier hypothesis that human thought has a superposed two-layered structure, one layer consisting of classical logical thought and a superposed layer consisting of quantum conceptual thought. Possible connections with recent findings of a grid-structure for the brain are analyzed, and consequences on applied disciplines, such as artificial intelligence and quantum computation, are considered. These results suggest that quantum models can be successfully employed to operationally describe the brain functioning, but they do not presuppose a microscopic quantum explanation of such functioning.**

***Keywords-concept theory*; *quantum cognition*; *cognitive processes*; *interference*; *brain structure*.**

I. INTRODUCTION

In recent years, it has become clear that quantum structures do not only appear within situations in the micro world, but that also situations of the macro world exhibit a quantum behavior [1]–[16]. Mainly, in domains such as cognitive science (decision theory, concept theory), biology (evolution theory, ecology, population dynamics) and computer science (semantic theories, information retrieval, artificial intelligence), aspects have been identified where the application of classical structures is problematic while the application of quantum structures is promising. The aspects of these domains where classical theories fail, and quantum structures are successful, reveal quite systematically four specific and very characteristic quantum effects, namely *interference*, *contextuality*, *emergence* and *entanglement*. Sometimes it has been possible to use the full quantum apparatus of linear operators in complex Hilbert space to model these effects as they appear in these situations. However, in quite some occasions a mathematical formalism more general than standard quantum mechanics in complex Hilbert space is needed. We have introduced in [17] a general modeling scheme for contextual emergent entangled interfering entities. In the present article, we instead focus on the identification of quantum superposition and interference in cognition to describe 'how' and 'why' interference models the well documented effects of *overextension* and *underextension* when concepts combine in disjunction [18]. Possible connections with some recent and interesting research on the structure of the brain and technological applications to symbolic artificial intelligence and computation are also presented.

Interference effects have been studied in great detail and are very common for quantum entities, the famous 'double slit situation' being an archetypical example of them [19]–[24]. Also for concepts we have studied some effects related to the phenomenon of interference in earlier work [9], [17], [25]–[27]. In the present article, we concentrate on the situation where two concepts, more specifically the concepts *Fruits* and *Vegetables* are combined by using the logical connective 'or' into a new concept *Fruits or Vegetables*. Such disjunctive combinations of concepts have been studied intensively by James Hampton [18]. Hampton collected experimental data from subjects being asked to estimate the typicality of a collection of exemplars with respect to *Fruits* and with respect to *Vegetables*. Then he asked the subjects also to estimate the typicality of the same exemplars with respect to the combination *Fruits or Vegetables*. By using the data of these experiments we identify interference between the concepts *Fruits* and *Vegetables*, and describe how this interference accounts for the effects of underextension and overextension identified by Hampton.

In Section II, we consider the set of data collected by Hampton, and work out a quantum description modeling these data. In Section III, we illustrate the phenomenon of interference as it appears in the considered conceptual combination, and in Section IV, we present an explanation for the occurrence of this quantum effect by comparing it with the interference typical of the two-slit experiment. This modeling suggests the hypothesis in Section V that a *quantum conceptual layer* is present in human thought which is superposed to the usually assumed *classical logical layer*, the former being responsible of deviations from classically expected reasoning in cognition. Finally, we present in Section VI a suggestion inspired by recent research where a *grid*, rather than a *neural network*, pattern, is identified in the structure of the brain [28]. More specifically, we put forward the hypothesis, albeit speculative, that the interference we identity between concepts, and the complex Hilbert space

 ISBN: 978-1-61208-214-1

that we structurally use to model this interference, might contain elements that have their isomorphic counterparts in the dynamics of the brain. Aspects of the impact of this hypothesis on the modeling and formalizing of natural and artificial knowledge, as well as the implications on artificial intelligence, robotics and quantum computation, are also investigated.

II. Fruits interfering with Vegetables

Let us consider the two concepts *Fruits* and *Vegetables*, and their combination *Fruits or Vegetables*, and work out a quantum model for the data collected by J. Hampton for this situation [18], [25]. The concepts *Fruits* and *Vegetables* are two exemplars of the concept *Food*. And we consider a collection of exemplars of *Food*, more specifically those listed in Table 1. Then we consider the following experimental situation: Subjects are asked to respond to the following three elements: *Question* A: 'Choose one of the exemplars from the list of Table 1 that you find a good example of *Fruits*'. *Question* B: 'Choose one of the exemplars from the list of Table 1 that you find a good example of *Vegetables*'. *Question* A *or* B: 'Choose one of the exemplars from the list of Table 1 that you find a good example of *Fruits or Vegetables*'. Then we calculate the relative frequency $\mu(A)_k$, $\mu(B)_k$ and $\mu(A \text{ or } B)_k$, i.e the number of times that exemplar k is chosen divided by the total number of choices made in response to the three questions A, B and A or B, respectively, and interpret this as an estimate for the probabilities that exemplar k is chosen for questions A, B and A or B, respectively. These relative frequencies are given in Table 1.

		$\mu(A)_k$	$\mu(B)_k$	Λ_k	Δ_k	λ_k	ϕ_k
A=Fruits *B=Vegetables*							
1	*Almond*	0.0359	0.0133	0.0269	0.0246	0.0218	83.8854°
2	*Acorn*	0.0425	0.0108	0.0249	0.0266	-0.0214	-94.5520°
3	*Peanut*	0.0372	0.0220	0.0269	0.0296	-0.0285	-95.3620°
4	*Olive*	0.0586	0.0269	0.0415	0.0428	0.0397	91.8715°
5	*Coconut*	0.0755	0.0125	0.0604	0.0440	0.0261	57.9533°
6	*Raisin*	0.1026	0.0170	0.0555	0.0598	0.0415	95.8648°
7	*Elderberry*	0.1138	0.0170	0.0480	0.0654	-0.0404	-113.2431°
8	*Apple*	0.1184	0.0155	0.0688	0.0670	0.0428	87.6039°
9	*Mustard*	0.0149	0.0250	0.0146	0.0199	-0.0186	-105.9806°
10	*Wheat*	0.0136	0.0255	0.0165	0.0195	0.0183	99.3810°
11	*Root Ginger*	0.0157	0.0323	0.0385	0.0240	0.0173	50.0889°
12	*Chili Pepper*	0.0167	0.0446	0.0323	0.0306	-0.0272	-86.4374°
13	*Garlic*	0.0100	0.0301	0.0293	0.0200	-0.0147	-57.6399°
14	*Mushroom*	0.0140	0.0545	0.0604	0.0342	0.0088	18.6744°
15	*Watercress*	0.0112	0.0658	0.0482	0.0385	-0.0254	-69.0705°
16	*Lentils*	0.0095	0.0713	0.0338	0.0404	0.0252	104.7126°
17	*Green Pepper*	0.0324	0.0788	0.0506	0.0556	-0.0503	-95.6518°
18	*Yam*	0.0533	0.0724	0.0541	0.0628	0.0615	98.0833°
19	*Tomato*	0.0881	0.0679	0.0688	0.0780	0.0768	100.7557°
20	*Pumpkin*	0.0797	0.0713	0.0579	0.0755	-0.0733	-103.4804°
21	*Broccoli*	0.0143	0.1284	0.0642	0.0713	-0.0422	-99.6048°
22	*Rice*	0.0140	0.0412	0.0248	0.0276	-0.0238	-96.6635°
23	*Parsley*	0.0155	0.0266	0.0308	0.0210	-0.0178	-61.1698°
24	*Black Pepper*	0.0127	0.0294	0.0222	0.0211	0.0193	86.6308°

Table I
Interference data for concepts *A=Fruits* and *B=Vegetables*. We put here $\Lambda_k = \mu(A \text{ or } B)_k$ and $\Delta_k = \frac{\mu(A)_k + \mu(B)_k}{2}$.

For example, for *Question* A, from 10,000 subjects, 359 chose *Almond*, hence $\mu(A)_1 = 0.0359$, 425 chose *Acorn*, hence $\mu(A)_2 = 0.0425$, 372 chose *Peanut*, hence $\mu(A)_3 = 0.0372$, ..., and 127 chose *Black Pepper*, hence $\mu(A)_{24} = 0.0127$. Analogously for *Question* B, from 10,000 subjects, 133 chose *Almond*, hence $\mu(B)_1 = 0.0133$, 108 chose *Acorn*, hence $\mu(B)_2 = 0.0108$, 220 chose *Peanut*, hence $\mu(B)_3 = 0.0220$, ..., and 294 chose *Black Pepper*, hence $\mu(B)_{24} = 0.0294$, and for *Question* A or B, 269 chose *Almond*, hence $\mu(A \text{ or } B)_1 = 0.0269$, 249 chose *Acorn*, hence $\mu(A \text{ or } B)_2 = 0.249$, 269 chose *Peanut*, hence $\mu(A \text{ or } B)_3 = 0.269$, ..., and 222 chose *Black Pepper*, hence $\mu(A \text{ or } B)_{24} = 0.222$.

Let us now explicitly construct a quantum mechanical model in complex Hilbert space for the pair of concepts *Fruit* and *Vegetable* and their disjunction '*Fruit or Vegetable*', and show that quantum interference models the experimental data gathered in [18]. We represent the measurement of 'a good example of' by means of a self-adjoint operator with spectral decomposition $\{M_k \mid k = 1, \ldots, 24\}$ where each M_k is an orthogonal projection of the Hilbert space $\mathcal{H}$ corresponding to item k from the list of items in Table 1. The concepts *Fruits*, *Vegetables* and '*Fruits or Vegetables*' are represented by unit vectors $|A\rangle$, $|B\rangle$ and $\frac{1}{\sqrt{2}}(|A\rangle + |B\rangle)$ of the Hilbert space $\mathcal{H}$, where $|A\rangle$ and $|B\rangle$ are orthgonal, and $\frac{1}{\sqrt{2}}(|A\rangle + |B\rangle)$ is their normalized superposition. Following standard quantum rules we have $\mu(A)_k = \langle A|M_k|A\rangle$, $\mu(B)_k = \langle B|M_k|B\rangle$, hence

$$\begin{aligned} \mu(A \text{ or } B)_k &= \tfrac{1}{2}\langle A+B|M_k|A+B\rangle \\ &= \tfrac{1}{2}(\mu(A)_k + \mu(B)_k) + \Re\langle A|M_k|B\rangle, \end{aligned} \tag{1}$$

where $\Re\langle A|M_k|B\rangle$ is the interference term. Let us introduce $|e_k\rangle$ the unit vector on $M_k|A\rangle$ and $|f_k\rangle$ the unit vector on $M_k|B\rangle$, and put $\langle e_k|f_k\rangle = c_k e^{i\gamma_k}$. Then we have $|A\rangle = \sum_{k=1}^{24} a_k e^{i\alpha_k}|e_k\rangle$ and $|B\rangle = \sum_{k=1}^{24} b_k e^{i\beta_k}|f_k\rangle$, which gives

$$\langle A|B\rangle = \Big(\sum_{k=1}^{24} a_k e^{-i\alpha_k}\langle e_k|\Big)\Big(\sum_{l=1}^{24} b_l e^{i\beta_l}|f_l\rangle\Big) = \sum_{k=1}^{24} a_k b_k c_k e^{i\phi_k} \tag{2}$$

where we put $\phi_k = \beta_k - \alpha_k + \gamma_k$. Further we have $\mu(A)_k = a_k^2$, $\mu(B)_k = b_k^2$, $\langle A|M_k|B\rangle = a_k b_k c_k e^{i\phi_k}$, which gives, by using (1),

$$\mu(A \text{ or } B)_k = \frac{1}{2}(\mu(A)_k + \mu(B)_k) + c_k\sqrt{\mu(A)_k\mu(B)_k}\cos\phi_k \tag{3}$$

We choose ϕ_k such that

$$\cos\phi_k = \frac{2\mu(A \text{ or } B)_k - \mu(A)_k - \mu(B)_k}{2c_k\sqrt{\mu(A)_k\mu(B)_k}} \tag{4}$$

and hence (3) is satisfied. We now have to determine c_k in such a way that $\langle A|B\rangle = 0$. Recall that from $\sum_{k=1}^{24}\mu(A \text{ or } B)_k = 1$ and (3), and with the choice of $\cos\phi_k$ that we made in (4), it follows that $\sum_{k=1}^{24} c_k\sqrt{\mu(A)_k\mu(B)_k}\cos\phi_k = 0$. Taking into account

(2), which gives $\langle A|B\rangle = \sum_{k=1}^{24} a_k b_k c_k(\cos\phi_k + i\sin\phi_k)$, and making use of $\sin\phi_k = \pm\sqrt{1-\cos^2\phi_k}$, we have $\langle A|B\rangle = 0 \Leftrightarrow \sum_{k=1}^{24} c_k\sqrt{\mu(A)_k\mu(B)_k}(\cos\phi_k + i\sin\phi_k) = 0 \Leftrightarrow \sum_{k=1}^{24} c_k\sqrt{\mu(A)_k\mu(B)_k}\sin\phi_k = 0 \Leftrightarrow$

$$\sum_{k=1}^{24} \pm\sqrt{c_k^2\mu(A)_k\mu(B)_k - (\mu(A \text{ or } B)_k - \frac{\mu(A)_k+\mu(B)_k}{2})^2} = 0 \quad (5)$$

We introduce the following quantities

$$\lambda_k = \pm\sqrt{\mu(A)_k\mu(B)_k - (\mu(A \text{ or } B)_k - \frac{\mu(A)_k+\mu(B)_k}{2})^2} \quad (6)$$

and choose m the index for which $|\lambda_m|$ is the biggest of the $|\lambda_k|$'s. Then we take $c_k = 1$ for $k \neq m$. We explain now the algorithm that we use to choose a plus or minus sign for λ_k as defined in (6), with the aim of being able to determine c_m such that (5) is satisfied. We start by choosing a plus sign for λ_m. Then we choose a minus sign in (6) for the λ_k for which $|\lambda_k|$ is the second biggest; let us call the index of this term m_2. This means that $0 \leq \lambda_m + \lambda_{m_2}$. For the λ_k for which $|\lambda_k|$ is the third biggest – let us call the index of this term m_3 – we choose a minus sign in case $0 \leq \lambda_m + \lambda_{m_2} + \lambda_{m_3}$, and otherwise we choose a plus sign, and in this case we have $0 \leq \lambda_m + \lambda_{m_2} + \lambda_{m_3}$. We continue this way of choosing, always considering the next biggest $|\lambda_k|$, and hence arrive at a global choice of signs for all of the λ_k, such that $0 \leq \lambda_m + \sum_{k\neq m}\lambda_k$. Then we determine c_m such that (5) is satisfied, or more specifically such that

$$c_m = \sqrt{\frac{(-\sum_{k\neq m}\lambda_k)^2 + (\mu(A \text{ or } B)_m - \frac{\mu(A)_m+\mu(B)_m}{2})^2}{\mu(A)_m\mu(B)_m}} \quad (7)$$

We choose the sign for ϕ_k as defined in (4) equal to the sign of λ_k. The result of the specific solution that we have constructed is that we can take $M_k(\mathcal{H})$ to be rays of dimension 1 for $k \neq m$, and $M_m(\mathcal{H})$ to be a plane. This means that we can make our solution still more explicit. Indeed, we take $\mathcal{H} = \mathbb{C}^{25}$ the canonical 25 dimensional complex Hilbert space, and make the following choices

$$|A\rangle = (\sqrt{\mu(A)_1}, \ldots, \sqrt{\mu(A)_m}, \ldots, \sqrt{\mu(A)_{24}}, 0) \quad (8)$$

$$|B\rangle = (e^{i\beta_1}\sqrt{\mu(B)_1}, \ldots, c_m e^{i\beta_m}\sqrt{\mu(B)_m}, \ldots, e^{i\beta_{24}}\sqrt{\mu(B)_{24}}, \sqrt{\mu(B)_m(1-c_m^2)}) \quad (9)$$

$$\beta_m = \arccos(\frac{2\mu(A \text{ or } B)_m - \mu(A)_m - \mu(B)_m}{2c_m\sqrt{\mu(A)_m\mu(B)_m}}) \quad (10)$$

$$\beta_k = \pm\arccos(\frac{2\mu(A \text{ or } B)_k - \mu(A)_k - \mu(B)_k}{2\sqrt{\mu(A)_k\mu(B)_k}}) \quad (11)$$

where the plus or minus sign in (11) is chosen following the algorithm we introduced for choosing the plus and minus sign for λ_k in (6). Let us construct this quantum model for the data given in Table 1. The exemplar which gives rise to the biggest value of $|\lambda_k|$ is *Tomato*, and hence we choose a plus sign and get $\lambda_{19} = 0.0768$. The exemplar giving rise to the second biggest value of λ_k is *Pumpkin*, and hence we choose a minus sign, and get $\lambda_{20} = -0.0733$. Next comes *Yam*, and since $\lambda_{19}+\lambda_{20}-0.0615 < 0$, we choose a plus sign for λ_{18}. Next is *Green Pepper*, and we look at $0 \leq \lambda_{19} + \lambda_{20}+\lambda_{18}-0.0503$, which means that we can choose a minus sign for λ_{17}. The fifth exemplar in the row is *Apple*. We have $\lambda_{19} + \lambda_{20} + \lambda_{18} + \lambda_{17} - 0.0428 < 0$, which means that we need to choose a plus sign for λ_8. Next comes *Broccoli* and verifying shows that we can choose a minus sign for λ_{21}. We determine in an analogous way the signs for the exemplars *Raisin*, plus sign, *Elderberry*, minus sign, *Olive*, plus sign, *Peanut*, minus sign, *Chili Pepper*, minus sign, *Coconut*, plus sign, *Watercress*, minus sign, *Lentils*, plus sign, *Rice*, minus sign, *Almond*, plus sign, *Acorn*, minus sign, *Black Pepper*, plus sign, *Mustard*, minus sign, *Wheat*, plus sign, *Parsley*, minus sign, *Root Ginger*, plus sign, *Garlic*, minus sign, and finally *Mushroom*, plus sign. In Table 1 we give the values of λ_k calculated following this algorithm, and from (7) it follows that $c_{19} = 0.7997$.

Making use of (8), (9), (10) and (11), and the values of the angles given in Table 1, we put forward the following explicit representation of the vectors $|A\rangle$ and $|B\rangle$ in $\mathbb{C}^{25}$ representing concepts *Fruits* and *Vegetables*

$$\begin{aligned}
|A\rangle &= (0.1895, 0.2061, 0.1929, 0.2421, 0.2748,\\
&\quad 0.3204, 0.3373, 0.3441, 0.1222, 0.1165,\\
&\quad 0.1252, 0.1291, 0.1002, 0.1182, 0.1059,\\
&\quad 0.0974, 0.1800, 0.2308, 0.2967, 0.2823,\\
&\quad 0.1194, 0.1181, 0.1245, 0.1128, 0)\\
|B\rangle &= (0.1154e^{i83.8854^\circ}, 0.1040e^{-i94.5520^\circ}, 0.1484e^{-i95.3620^\circ},\\
&\quad 0.1640e^{i91.8715^\circ}, 0.1120e^{i57.9533^\circ}, 0.1302e^{i95.8648^\circ},\\
&\quad 0.1302e^{-i113.2431^\circ}, 0.1246e^{i87.6039^\circ}, 0.1580e^{-i105.9806^\circ},\\
&\quad 0.1596e^{i99.3810^\circ}, 0.1798e^{i50.0889^\circ}, 0.2112e^{-i86.4374^\circ},\\
&\quad 0.1734e^{-i57.6399^\circ}, 0.2334e^{i18.6744^\circ}, 0.2565e^{-i69.0705^\circ},\\
&\quad 0.2670e^{i104.7126^\circ}, 0.2806e^{-i95.6518^\circ}, 0.2690e^{i98.0833^\circ},\\
&\quad 0.2606e^{i100.7557^\circ}, 0.2670e^{-i103.4804^\circ}, 0.3584e^{-i99.6048^\circ},\\
&\quad 0.2031e^{-i96.6635^\circ}, 0.1630e^{-i61.1698^\circ}, 0.1716e^{i86.6308^\circ},\\
&\quad 0.1565). \quad (12)
\end{aligned}$$

This proves that we can model the data of [18] by means of a quantum mechanical model, and such that the values of $\mu(A \text{ or } B)_k$ are determined from the values of $\mu(A)_k$ and $\mu(B)_k$ as a consequence of quantum interference effects. For each k the value of ϕ_k in Table 1 gives the quantum interference phase of the exemplar number k.

III. Graphs of the interference patterns

In [25], we worked out a way to 'chart' the quantum interference patterns of the two concepts when combined into conjunction or disjunction. Since it helps our further analysis in the present article, we put forward this 'chart' for the case of the concepts *Fruits* and *Vegetables* and

their disjunction '*Fruits or Vegetables*'. More specifically, we represent the concepts *Fruits*, *Vegetables* and '*Fruits or Vegetables*' by complex valued wave functions of two real variables $\psi_A(x,y), \psi_B(x,y)$ and $\psi_{A\text{or}B}(x,y)$.

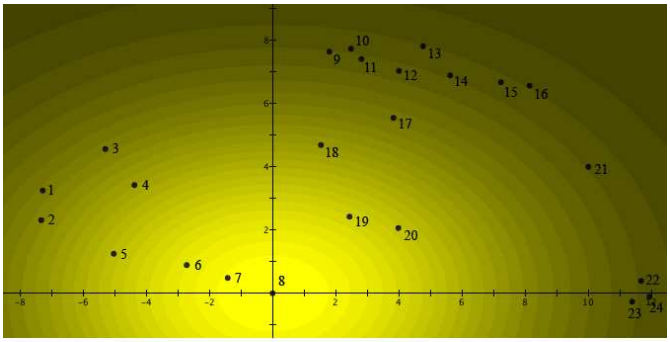

Figure 1. The probabilities $\mu(A)_k$ of a person choosing the exemplar k as a 'good example' of *Fruits* are fitted into a two-dimensional quantum wave function $\psi_A(x,y)$.

We choose $\psi_A(x,y)$ and $\psi_B(x,y)$ such that the real part for both wave functions is a Gaussian in two dimensions, which is always possible since we have to fit in only 24 values, namely the values of ψ_A and ψ_B for each of the exemplars of Table 1. The squares of these Gaussians are graphically represented in Figs. 1 and 2, and the different exemplars of Table 1 are located in spots such that the Gaussian distributions $|\psi_A(x,y)|^2$ and $|\psi_B(x,y)|^2$ properly model the probabilities $\mu(A)_k$ and $\mu(B)_k$ in Table 1 for each one of the exemplars. For example, for *Fruits* represented in Fig. 1, *Apple* is located in the center of the Gaussian, since *Apple* was most frequently chosen by the test subjects when asked *Question A*. *Elderberry* was the second most frequently chosen, and hence closest to the top of the Gaussian in Fig. 1. Then come *Raisin*, *Tomato* and *Pumpkin*, and so on, with *Garlic* and *Lentils* as the least chosen 'good examples' of *Fruits*. For *Vegetables*, represented in Fig. 2, *Broccoli* is located in the center of the Gaussian, since *Broccoli* was the exemplar most frequently chosen by the test subjects when asked *Question B*. *Green Pepper* was the second most frequently chosen, and hence closest to the top of the Gaussian in Fig. 2. Then come *Yam*, *Lentils* and *Pumpkin*, and so on, with *Coconut* and *Acorn* as the least chosen 'good examples' of *Vegetables*. Metaphorically, we could regard the graphical representations of Figs. 1 and 2 as the projections of two light sources each shining through one of two holes in a plate and spreading out their light intensity following a Gaussian distribution when projected on a screen behind the holes. The center of the first hole, corresponding to the *Fruits* light source, is located where exemplar *Apple* is at point $(0,0)$, indicated by 8 in both figures. The center of the second hole, corresponding to the *Vegetables* light source, is located where exemplar *Broccoli* is at point (10,4), indicated by 21 in both figures.

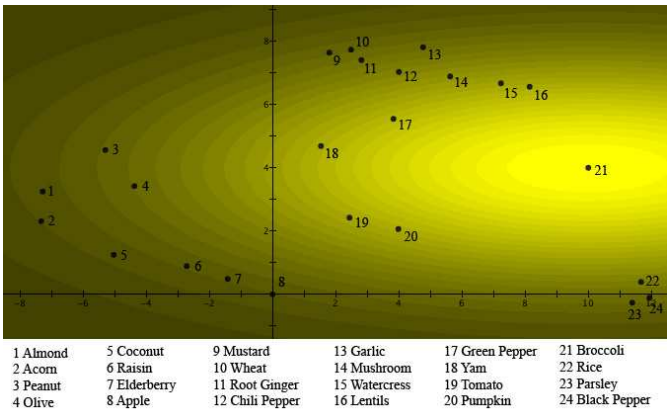

Figure 2. The probabilities $\mu(B)_k$ of a person choosing the exemplar k as an example of *Vegetables* are fitted into a two-dimensional quantum wave function $\psi_B(x,y)$.

In Fig. 3, the data for '*Fruits or Vegetables*' are graphically represented. This is not 'just' a normalized sum of the two Gaussians of Figs. 1 and 2, since it is the probability distribution corresponding to $\frac{1}{\sqrt{2}}(\psi_A(x,y)+\psi_B(x,y))$, which is the normalized superposition of the wave functions in Figs. 1 and 2.

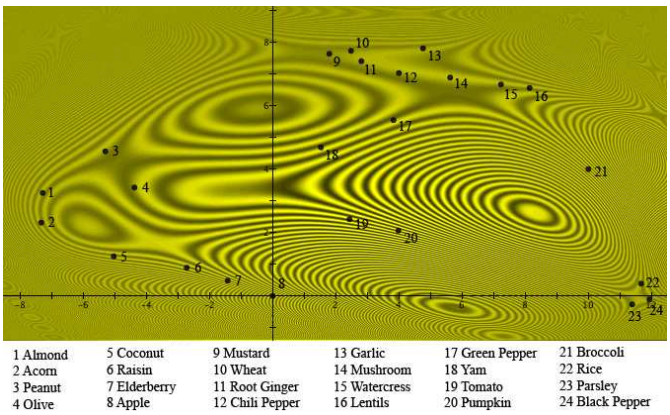

Figure 3. The probabilities $\mu(A \text{ or } B)_k$ of a person choosing the exemplar k as an example of '*Fruits or Vegetables*' are fitted into the two-dimensional quantum wave function $\frac{1}{\sqrt{2}}(\psi_A(x,y)+\psi_B(x,y))$.

The numbers are placed at the locations of the different exemplars with respect to the probability distribution $\frac{1}{2}|\psi_A(x,y)+\psi_B(x,y)|^2 = \frac{1}{2}(|\psi_A(x,y)|^2 + |\psi_B(x,y)|^2) + |\psi_A(x,y)\psi_B(x,y)|\cos\phi(x,y)$, where $|\psi_A(x,y)\psi_B(x,y)|\cos\phi(x,y)$ is the interference term and $\phi(x,y)$ the quantum phase difference at (x,y). The values of $\phi(x,y)$ are given in Table 1 for the locations of the different exemplars.

 ISBN: 978-1-61208-214-1

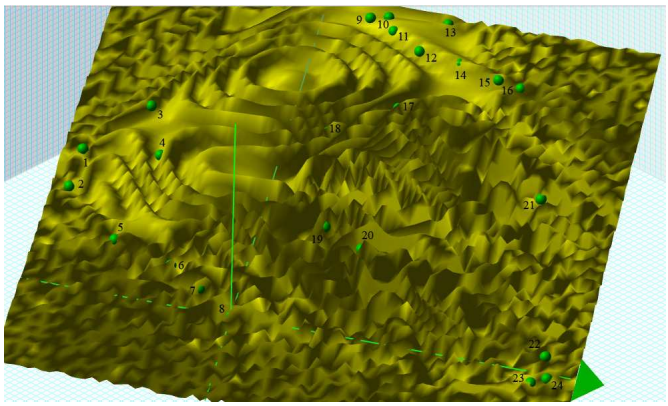

Figure 4. A three-dimensional representation of the interference landscape of the concept '*Fruits* or *Vegetables*' as shown in Fig. 3.

The interference pattern shown in Fig. 3 is very similar to well-known interference patterns of light passing through an elastic material under stress. In our case, it is the interference pattern corresponding to '*Fruits or Vegetables*'. Bearing in mind the analogy with the light sources for Figs. 1 and 2, in Fig. 3 we can see the interference pattern produced when both holes are open.

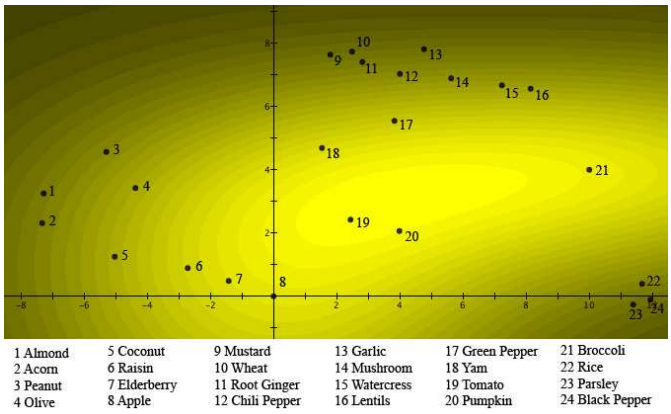

Figure 5. Probabilities $1/2(\mu(A)_k + \mu(B)_k)$, which are the probability averages for *Fruits* and *Vegetables* shown in Figs. 2 and 3.

Fig. 4 represents a three-dimensional graph of the interference pattern of Fig. 3, and, for the sake of comparison, in Fig. 5, we have graphically represented the averages of the probabilities of Figs. 1 and 2, i.e., the values measured if there were no interference. For the mathematical details – the exact form of the wave functions and the explicit calculation of the interference pattern – and for other examples of conceptual interference, we refer to [25].

IV. Explaining Quantum Interference

The foregoing section showed how the typicality data of two concepts and their disjunction are quantum mechanically modeled such that the quantum effect of interference accounts for the measured values. We also showed that it is possible to metaphorically picture the situation such that each of the concepts is represented by light passing through a hole and the disjunction of both concepts corresponds to the situation of the light passing through both holes (see Fig. 6).

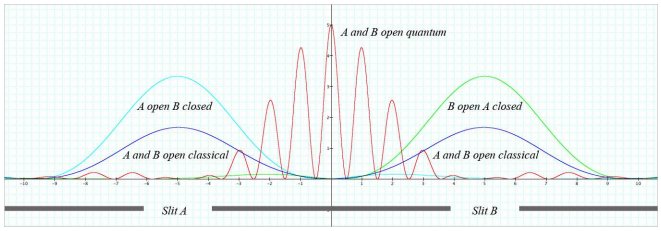

Figure 6. A typical interference pattern of a quantum two-slit situation.

This is indeed where interference is best known from the traditional double-slit situation in optics and quantum physics. If we apply this to our specific example by analogy, we can imagine the cognitive experiment where a subject chooses the most appropriate answer for one of the concepts, e.g., *Fruits*, as follows: 'The photon passes with the *Fruits* hole open and hits a screen behind the hole in the region where the choice of the person is located'. We can do the same for the cognitive experiment where the subject chooses the most appropriate answer for the concept *Vegetables*. This time, the photon passes with the *Vegetables* hole open and hits the screen in the region where the choice of the person is located. The third situation, corresponding to the choice of the most appropriate answer for the disjunction concept '*Fruits or Vegetables*', consists in the photon passing with both the *Fruits* hole and the *Vegetables* hole open and hitting the screen where the choice of the person is located. This third situation is the situation of interference, viz. the interference between *Fruits* and *Vegetables*. These three situations are clearly illustrated in Figs. 1, 2 and 3.

In [9], [26], [27], we analyzed the origin of the interference effects that are produced when concepts are combined, and we provided an explanation that we investigated further in [25].

Let us now take a closer look at the experimental data and how they are produced by interference. The exemplars for which the interference is a weakening effect, i.e. where $\mu(A \text{ or } B) < 1/2(\mu(A) + \mu(B))$ or $90° \leq \phi$ or $\phi \leq -90°$, are the following: *Elderberry*, *Mustard*, *Lentils*, *Pumpkin*, *Tomato*, *Broccoli*, *Wheat*, *Yam*, *Rice*, *Raisin*, *Green Pepper*, *Peanut*, *Acorn* and *Olive*. The exemplars for which interference is a strengthening effect, i.e. where $1/2(\mu(A) + \mu(B)) < \mu(A \text{ or } B)$ or $\phi < 90°$ or $-90° \leq \phi$, are the following: *Mushroom*, *Root Ginger*, *Garlic*, *Coconut*, *Parsley*, *Almond*, *Chili Pepper*, *Black Pepper*, and *Apple*. Let us consider the two extreme cases, viz. *Elderberry*, for which interference is the most weakening ($\phi = -113.2431°$), and *Mushroom*, for which it is the most strengthening

 ISBN: 978-1-61208-214-1

($\phi = 18.6744$). For *Elderberry*, we have $\mu(A) = 0.1138$ and $\mu(B) = 0.0170$, which means that test subjects have classified *Elderberry* very strongly as *Fruits* (*Apple* is the most strongly classified *Fruits*, but *Elderberry* is next and close to it), and quite weakly as *Vegetables*. For *Mushroom*, we have $\mu(A) = 0.0140$ and $\mu(B) = 0.0545$, which means that test subjects have weakly classified *Mushroom* as *Fruits* and moderately as *Vegetables*. Let us suppose that $1/2(\mu(A) + \mu(B))$ is the value estimated by test subjects for '*Fruits or Vegetables*'. In that case, the estimates for *Fruits* and *Vegetables* apart would be carried over in a determined way to the estimate for '*Fruits or Vegetables*', just by applying this formula. This is indeed what would be the case if the decision process taking place in the human mind worked as if a classical particle passing through the *Fruits* hole or through the *Vegetables* hole hit the mind and left a spot at the location of one of the exemplars. More concretely, suppose that we ask subjects first to choose which of the questions they want to answer, *Question A* or *Question B*, and then, after they have made their choice, we ask them to answer this chosen question. This new experiment, which we could also indicate as *Question A* or *Question B*, would have $1/2(\mu(A)+\mu(B))$ as outcomes for the weight with respect to the different exemplars. In such a situation, it is indeed the mind of each of the subjects that chooses randomly between the *Fruits* hole and the *Vegetables* hole, subsequently following the chosen hole. There is no influence of one hole on the other, so that no interference is possible. However, in reality the situation is more complicated. When a test subject makes an estimate with respect to '*Fruits or Vegetables*', a new concept emerges, namely the concept '*Fruits or Vegetables*'. For example, in answering the question whether the exemplar *Mushroom* is a good example of '*Fruits or Vegetables*', the subject will consider two aspects or contributions. The first is related to the estimation of whether *Mushroom* is a good example of *Fruits* and to the estimation of whether *Mushroom* is a good example of *Vegetables*, i.e. to estimates of each of the concepts separately. It is covered by the formula $1/2(\mu(A) + \mu(B))$. The second contribution concerns the test subject's estimate of whether or not *Mushroom* belongs to the category of exemplars that cannot readily be classified as *Fruits* or *Vegetables*. This is the category characterized by the newly emerged concept '*Fruits or Vegetables*'. And as we know, *Mushroom* is a typical case of an exemplar that is not easy to classify as '*Fruits or Vegetables*'. That is why *Mushroom*, although only slightly covered by the formula $1/2(\mu(A) + \mu(B))$, has an overall high score as '*Fruits or Vegetables*'. The effect of interference allows adding the extra value to $1/2(\mu(A)+\mu(B))$ resulting from the fact that *Mushroom* scores well as an exemplar that is not readily classified as '*Fruits or Vegetables*'. This explains why *Mushroom* receives a strengthening interference effect, which adds to the probability of it being chosen as a good example of '*Fruits or Vegetables*'. *Elderberry* shows the contrary. Formula $1/2(\mu(A)+\mu(B))$ produces a score that is too high compared to the experimentally tested value of the probability of its being chosen as a good example of '*Fruits or Vegetables*'. The interference effect corrects this, subtracting a value from $1/2(\mu(A)+\mu(B))$. This corresponds to the test subjects considering *Elderberry* 'not at all' to belong to a category of exemplars hard to classify as *Fruits* or *Vegetables*, but rather the contrary. As a consequence, with respect to the newly emerged concept '*Fruits or Vegetables*', the exemplar *Elderberry* scores very low, and hence the $1/2(\mu(A) + \mu(B))$ needs to be corrected by subtracting the second contribution, the quantum interference term. A similar explanation of the interference of *Fruits* and *Vegetables* can be put forward for all the other exemplars. The following is a general presentation of this. 'For two concepts A and B, with probabilities $\mu(A)$ and $\mu(A)$ for an exemplar to be chosen as a good example of 'A or B', the interference effect allows taking into account the specific probability contribution for this exemplar to be chosen as a good exemplar of the newly emerged concept 'A or B', adding or subtracting to the value $1/2(\mu(A)+\mu(B))$, which is the average of $\mu(A)$ and $\mu(B)$.'

To conclude, we observe that '*Fruits or Vegetables*' is not the only case where quantum interference explains deviations from classically expected reasoning. Various concept combinations have been identified entailing such deviation, for disjunctions, as well as for conjunctions [9].

V. A TWO-LAYERED STRUCTURE IN HUMAN THOUGHT

The detection of quantum structures in cognition has suggested us to put forward the hypothesis that two specifically structured and superposed layers can be identified in human thought as a process [9], as follows.

(i) A *classical logical layer*. The thought process in this layer is given form by an underlying classical logical conceptual process. The manifest process itself may be, and generally will be, indeterministic, but the indeterminism is due to a lack of knowledge about the underlying deterministic classical process. For this reason the process within the classical logical layer can be modeled by using a classical Kolmogorovian probability description.

(ii) A *quantum conceptual layer*. The thought process in this layer is given form under influence of the totality of the surrounding conceptual landscape, where the different concepts figure as individual entities, also when they are combinations of other concepts, at variance with the classical logical layer where combinations of concepts figure as classical combinations of entities and not as individual entities. In this sense one can speak of a *conceptual emergence* taking place in this quantum conceptual layer, certainly so for combinations of concepts. Quantum conceptual thought has been identified in different domains of knowledge and science related to different, often as

 ISBN: 978-1-61208-214-1

paradoxically conceived, problems in these domains. The sorts of measurable quantities being able to experimentally identify quantum conceptual thought have been different in these different domains, depending on which aspect of the conceptual landscape was most obvious or most important for the identification of the deviation of classically expected values of these quantities. For example, in a domain of cognitive science where representations of concepts are studied, and hence where concepts and combinations of concepts, and relations of items, exemplars, instances or features with concepts are considered, measurable quantities such as 'typicality', 'membership', 'similarity' and 'applicability' have been studied and used to experimentally put into evidence the deviation of what classically would be expected for the values of these quantities. In decision theory measurable quantities such as 'representativeness', 'qualitative likelihood', 'similarity' and 'resemblance' have played this role. The quantum conceptual thought process is indeterministic in essence, i.e. there is not necessarily an underlying deterministic process independent of the context. Hence, if analyzed deeper with the aim of finding more deterministic sub-processes, unavoidably effects of context will come into play. Since all concepts of the interconnected web that forms the landscape of concepts and combinations of them attribute as individual entities to the influences reigning in this landscape, and more so since this happens dynamically in an environment where they are all quantum entangled structurally speaking, the nature of quantum conceptual thought contains aspects that we strongly identify as holistic and synthetic. However, the quantum conceptual thought process is not unorganized or irrational. Quantum conceptual thought is as firmly structured as classical logical thought though in a different way. We believe that the reason why science has hardly uncovered the structure of quantum conceptual thought is because it has been believed to be intuitive, associative, irrational, etc., meaning 'rather unstructured'. As a consequence of its basic features, an idealized version of this quantum conceptual thought process can be modeled as a quantum mechanical process.

The assumed existence of a quantum conceptual layer in the human mind fits in with some interesting achievements that have been recently obtained in neuroscience [28], as we will see in the next section.

VI. Quantum cognition and the structure of the brain

A traditional view of the relation between brain and mind is based on the *neuroscience paradigm* [29], according to which the architecture of the brain is determined by connections between neurons, their inibitory/excitatory character, and the strength of their connections. Roughly speaking, the brain can be seen as a *parallel distributed computer* containing many billions of neurons, that is, elementary processors interconnected into a complex neural network. In this architecture, the mind and the brain constitute one single unit, which is characterized by a complementary dualism. The mind is understood as a program carried out by the brain, the program being specified by the neural network architecture. Distributed representations of cognitive structures are studied in such an approach (see, e.g., *holographic reduced representations* [30]–[33]).

Although the holographic approach is inspired by waves and interference, it is not able to model the complex type of interference that quantum entities undergo. It can be seen by considering the values of the interference angles of the interference pattern we obtain (see (12)), that the modeling for the concept *Fruit or Vegetables* is intrinsically quantum mechanical, not able to be reduced to interference of classical waves. This means that, although along the same lines as the holographic memory view [30], our approach can introduce a way to consider and study the brain as a quantum interference producing entity. Concretely we produce a projection of a multi-dimensional complex Hilbert space – 25 dimensional for the *Fruits or Vegetables* case – in the three-dimensional real space, which is the environment where the bio-mass of the brain is located.

In this respect, it is worthy to mention a recent finding [28], where relationships of adjacency and crossing between cerebral fiber pathways in primates and humans were analyzed by using diffusion magnetic resonance imaging. The cerebral fiber pathways have been found to form a rectilinear three-dimensional grid continuous with the three principal axes of development. Cortico-cortical pathways formed parallel sheets of interwoven paths in the longitudinal and medio-lateral axes, in which major pathways were local condensations. Cross-species homology was strong and showed emergence of complex gyral connectivity by continuous elaboration of this grid structure. This architecture naturally supports functional spatio-temporal coherence, developmental path-finding, and incremental rewiring with correlated adaptation of structure and function in cerebral plasticity and evolution [28]. The three-dimensional layered structure schematized above puts at stake the 'neural network' modeling of the brain, together with some aspects of the neuroscience paradigm, and the brain/mind relation. Such a very mathematically structured grid form would be much closer to what one expect as an ideal medium for interference than this is the case for the structure of a traditional network.

At first sight it might seem that the layered structures that have been detected [28] are too simple to give rise to complex cognition, even if interference is allowed to play a prominent role, but that is misleading. Indeed, one should not look upon the brain as 'a container of complex cognition', but rather as 'the canvas for the potentiality of emergence of such complex cognition'. That makes a whole difference. Indeed, we know how the rather simple mathematical structure of superposition in a linear vector space

 ISBN: 978-1-61208-214-1

and tensor product of linear vector spaces give rise to both emergence and entanglement in quantum mechanics. Also there this mathematical structure plays the role of canvas, where the emergent and entangled states can find a seat to be realized. This is exactly what the role of the recently detected grid could be, due to its rather simple mathematical structure, at least compared to the structure of a network, it could make available in a mathematically systematic way the canvas where emergent states of new concepts can find their seat. This is then a mechanism fundamentally different from what one expects in networks, where 'new connections are only made when they are needed'. Structures that have generative power can shape 'empty space' for potentiality, and 'creation of new', hence emergence can take place in a much more powerful way. Of course, there will be a bias coming from the generating structures, which is a drawback compared to the network way. This bias could exactly be an explanation for the functioning of the human brain leading to automated aspects of conceptual reasoning such as 'the disjunction and conjunction effects'. The above analysis is highly relevant for representations of genuine cognitive models in technology, for example as attempted in artificial intelligence and robotics [34]–[36].

We recall, to conclude this section, that the employment of quantum structures in the modeling of cognitive disciplines does not presuppose, though is not incompatible with, the requirement that microscopic quantum processes occur in the human brain. We indeed avoided such a compelling assumption in this paper.

VII. Conclusions

To understand how concepts combine in human thought to form sentences and texts and how meaning flows between human minds using such combinations, is one of the age-old problems of cognitive sciences. Apart from it being a cornerstone for a deeper understanding of human thought and mind, progress in many fields, including psychology, linguistics, artificial intelligence, and cognitive science, depends crucially on this combination mechanism. Also important scientific problems, such as text analysis, information retrieval and human-computer interaction rely directly on insights into a deeper understanding of how concepts combine. Although much investigation effort has been put in this problem, very little substantial results have been obtained. However, models of concepts making use of the mathematical formalisms of quantum theory have been substantially more successful than classical approaches at modeling data generated in studies of combinations of two concepts. In this paper, we have presented an improved and more complete version of our quantum modeling approach, and we have provided a description of the overextension and underextension measured by Hampton in the disjunction *Fruits or Vegetables* as an effect of quantum interference. We have shown that quantum interference patterns naturally appear whenever suitable exemplars of this disjunction are taken into account. We have analyzed the graphs revealing the interference pattern of *Fruits or Vegetables* and compared them with the interference of light in a double-slit quantum experiment. The identification of quantum structures in cognitive disciplines allowed us to derive two relevant insights concerning thought processes and the mind/brain relation. First, it suggests that two superposed and interconnected layers – a classical logical and a quantum conceptual – are present in human thought as a process, as already put forward by ourselves in some previous papers. Second, the three-dimensional grid structure recently discovered in the brain could explain, better than the neural network structure, the emergence of new concepts which we recognized in the present paper as responsible of the quantum effects of superposition and interference in concept combinations. In this new perspective, the brain would not be seen as a container of complex cognition but, rather, as the canvas for the potentiality of emergence of such complex cognition.

The results attained in this paper suggest that quantum models can be useful to operatonally describe the functioning of the human brain without presupposing any microscopic quantum explanation of brain functioning, and can be also interesting for the community of quantum technology researchers.

References

[1] D. Aerts and S. Aerts, "Applications of quantum statistics in psychological studies of decision processes," *Found. Sci.*, vol. 1, pp. 85–97, 1995.

[2] K. van Rijsbergen, *The Geometry of Information Retrieval*, Cambridge, UK: Cambridge University Press, 2004.

[3] D. Aerts and M. Czachor, "Quantum aspects of semantic analysis and symbolic artificial intelligence," *J. Phys. A-Math. Gen.*, vol. 37, pp. L123–L132, 2004.

[4] D. Aerts and L. Gabora, "A theory of concepts and their combinations I & II," *Kybernetes*, vol. 34, pp. 167–191 & 192–221, 2005.

[5] P. D. Bruza and R. J. Cole, "Quantum logic of semantic space: An explanatory investigation of context effects in practical reasoning," in *We Will Show Them: Essays in Honour of Dob Gabbay*, S. Artemov *et al.*, Eds., College Publications, 2005.

[6] D. Widdows, *Geometry and Meaning*, CSLI Publications, IL: University of Chicago Press, 2006.

[7] J. R. Busemeyer, Z. Wang, and J. T. Townsend, "Quantum dynamics of human decision-making," *J. Math. Psych.*, vol. 50, pp. 220–241, 2006.

[8] P. D. Bruza, K. Kitto, D. McEvoy, and C. McEvoy, "Entangling words and meaning," in *Proceedings of the Second Quantum Interaction Symposium*, Oxford, UK, Oxford University Press, 2008, pp. 118–124.

 ISBN: 978-1-61208-214-1

[9] D. Aerts, "Quantum structure in cognition," *J. Math. Psych.*, vol. 53, pp. 314–348, 2009.

[10] D. Aerts, M. Czachor, and B. De Moor, "Geometric analogue of holographic reduced representation," *J. Math. Psych.*, Vol. 53, pp. 389–398, 2009.

[11] P. D. Bruza, K. Kitto, D. Nelson, and C. McEvoy, "Extracting spooky-activation-at-a-distance from considerations of entanglement," in *Proceedings of QI 2009-Third International Symposium on Quantum Interaction*, P. D. Bruza, D. Sofge, W. Lawless, C. J. van Rijsbergen, and M. Klusch, Eds., LNCS vol. 5494, Berlin, Heidelberg: Springer, 2009, pp. 71–83.

[12] E. M. Pothos and J. R. Busemeyer, "A quantum probability explanation for violations of 'rational' decision theory," *Proc. Roy. Soc. B*, vol. 276, pp. 2171–2178, 2009.

[13] A. Y. Khrennikov and E. Haven, "Quantum mechanics and violations of the Sure-Thing Principle: The use of probability interference and other concepts," *J. Math. Psych.*, vol. 53, pp. 378–388, 2009.

[14] D. Aerts and S. Sozzo, "Quantum structure in cognition: Why and how concepts are entangled," in *Proceedings of QI 2011-Fourth International Symposium on Quantum Interaction*, D. Song, M. Melucci, and I. Frommholz, Eds., Berlin, Heidelberg: Springer, 2011, LNCS, vol. 7052, pp. 116–127.

[15] D. Aerts, M. Czachor, and S. Sozzo, "Quantum interaction approach in cognition, artificial intelligence and robotics,"in *Proceedings of the The Fifth International Conference on Quantum, Nano and Micro Technologies (ICQNM 2011)*, V. Privman and V. Ovchinnikov, Eds., IARIA, 2011, pp. 35–40, 2011.

[16] D. Aerts, L. Gabora, S. Sozzo, and T. Veloz, "Quantum interaction approach in cognition, artificial intelligence and robotics," in *Proceedings of the Fifth International Conference on Quantum, Nano and Micro Technologies (ICQNM)*, V. Privman and V. Ovchinnikov, Eds., IARIA, 2011, pp. 57–62, 2011.

[17] D. Aerts and S. Sozzo, "A general modeling scheme for contextual emergent entangled interfering entities," Accepted in the Proceedings of QI 2012-Fifth International Symposium on Quantum Interaction, 2012.

[18] J. A. Hampton, "Disjunction of natural concepts," *Memory & Cognition*, vol. 16, pp. 579–591, 1988.

[19] T. Young, "On the theory of light and colours," *Phil. Trans. Roy. Soc.*, vol. 92, pp. 12–48, 1802. Reprinted in part in: Crew, H. (ed.) The Wave Theory of Light, New York (1990).

[20] L. de Broglie, "Ondes et quanta," *Comptes Rendus*, vol. 177, pp. 507–510, 1923.

[21] E. Schrödinger, "Quantizierung als Eigenwertproblem(Erste Mitteilung)," *Ann. Phys.*, vol. 79, pp. 361–376, 1926.

[22] R. P. Feynman, *The Feynman Lectures on Physics*, New York: Addison–Wesley, 1965.

[23] C. Jönsson, "Electron diffraction at multiple slits," *Am. J. Phys*, vol. 4, pp. 4–11, 1974.

[24] M. Arndt, O. Nairz, J. Vos–Andreae, C. Keller, G. van der Zouw, and A. , Zeilinger, "Wave-particle duality of C_{60} molecules," *Nature*, vol. 401, pp. 680–682, 1999.

[25] D. Aerts, "Quantum particles as conceptual entities. A Possible Explanatory Framework for Quantum Theory," *Found. Sci.*, vol. 14, pp. 361–411, 2009.

[26] D. Aerts, "Quantum interference and superposition in cognition: Development of a theory for the disjunction of concepts," in *Worldviews, Science and Us: Bridging [34]–[36]Knowledge and Its Implications for Our Perspectives of the World*, D. Aerts, B. D'Hooghe, and N. Note, Eds., Singapore: World Scientific, 2011, pp. 169–211.

[27] D. Aerts, "General quantum modeling of combining concepts: A quantum field model in Fock space," Archive reference and link: *http://uk.arxiv.org/abs/0705.1740*, 2007.

[28] V. J. Weeden, D. L. Rosene, R. Wang, G. Dai, F. Mortazavi, P. Hagmann, J. H. Kaas, and W. I. Tseng, "The geometric structure of the brain fiber pathways," *Science*, vol. 335, pp. 1628–1634, 2012.

[29] J. L. M. McClelland, D. E. Rumelhart, and the PDP research group, Eds., *Parallel Distributed Processing: Explorations in the Microstructure of Cognition*, vols. 1 and 2, Cambridge, MA: The MIT Press, 1986.

[30] D. Gabor, "Holographic model for temporal recall," *Nature*, vol. 217, 1288–1289, 1968.

[31] K. H. Pribram, *Languages of the Brain: Experimental Paradoxes and Principles in Neuropsychology*, New York, NY: Prentice Hall, 1971.

[32] P. Kanerva, "Large patterns make great symbols: An example of learning from example," *Hybrid Neural Systems*, pp. 194–203, 1998.

[33] T. Plate, '*Holographic Reduced Representation: Distributed Representation for Cognitive Structures*, Stanford, CA: CSLI Publications, 2003.

[34] R. Penrose, *The Emperor's New Mind*, Oxford, UK: Oxford University Press, 1990.

[35] P. Benioff, "Quantum robots and environments," *Phys. Rev. A*, vol. 58, no. 2, pp. 893–904, 1998.

[36] D. Dong, C. Chen, C. Zhang, and Z. Chen, "Quantum robots: Structure, algorithms and applications," *Robotica*, vol. 24, pp. 513–521, 2006.

 ISBN: 978-1-61208-214-1

Assessment of High-Frequency Peformance Potential of Graphene Field-Effect Transistors

Jyotsna Chauhan, Leitao Liu, Yang Lu and Jing Guo
Department of ECE, University Florida
Florida, Gainesville, FL, 32611-6130, USA
{jyotsna.chauhan, leitaoliu, yanglu, guoj}@ufl.edu

***Abstract*—We assess high frequency performance potential of graphene field-effect transistors (FETs) down to a channel length of 10nm by using self-consistent ballistic and dissipative quantum transport simulations. The results indicate that with a thin high-κ gate insulator, the intrinsic ballistic cut off frequency f_T is above 5THz at a gate length of 10nm. Inelastic phonon scattering in graphene FETs lowers both f_T and the unitary power gain frequency f_{MAX}, mostly due to decrease of the transconductance. f_{MAX} and f_T are severely degrading in presence of source and drain contact resistance. To achieve optimum extrinsic f_{MAX} performance, careful choice of DC bias point in quasi-saturation regime and gate width is needed. Modeling of dissipative quantum transport is based on implementation of parallel simulation algorithms for the self-consistent Born approximation in the non-equilibrium Green's function (NEGF) formalism.**

Keywords-graphene transistors, RF performance, quantum transport simualtion

I. INTRODUCTION

Extraordinary electronic transport properties like high mobility and high saturation velocity make graphene attractive for radio frequency (RF) electronics applications [1]. Although the zero bandgap of 2D graphene leads to a low on-off ratio not desired for digital electronics applications, RF electronics applications do not require a large on-off ratio. Scaling down the channel length plays a critically important role for boosting the RF performance of a field-effect transistor (FET), and aggressive channel length scaling of graphene FET has been experimentally pursued. Recent experiments have demonstrated graphene transistors with intrinsic cut-off frequency projected to be at the hundreds of GHz range at sub 100nm channel scale [2-3]. The issues of the ultimate channel scaling, role of inelastic phonon scattering and performance potential of the unitary power gain frequency of graphene RF transistors, however, remain unclear.

II. APPROACH

Graphene FETs were simulated by solving the quantum transport equation using the non-equilibrium Green's function (NEGF) formalism with the Dirac Hamilton, self-consistently with a two-dimensional Poisson equation. Quasi-static approximations are used to assess its high-frequency performance [4]. Dissipative quantum transport due to inelastic phonon scattering, such as scattering due to polar optical phonons of the gate insulator and the intrinsic optical phonon of graphene, is modeled by using parallel simulation implementation of the self-consistent Born approximation in the NEGF formalism [5].

III. RESULTS AND DISCUSSIONS

We first analyze the small signal parameters of graphene FETs with channel scaling down to 5nm.The ideal performance limits for graphene FETs are studied by running ballistic simulations. The potential profile of the device at V_G =-0.6V and V_D =0.5V is also shown in Fig. 1(c). To model scattering, the effect of optical phonon scattering for $\hbar\omega$=180meV and $\hbar\omega$=55meV on device characteristics is included. The elastic scattering by acoustic phonons and charge impurities in high quality graphene has a much longer mean free path than inelastic phonon scattering. Therefore, elastic scattering is not considered as part of this study, focused on channel length scaling in sub 100nm regime. The small signal equivalent model for graphene FETs is shown in Fig. 1(b) where g_m is the transconductance, g_{ds} is the output conductance, R_g is the gate resistance, R_S (R_d) is the source (drain) contact resistance, C_{gs} is the small signal gate to source capacitance, C_{gd} is the small signal gate to drain capacitance and C_{ps} (C_{pd}) is the parasitic capacitance. The model is similar to that of conventional silicon MOSFETs, however, with the element parameters being determined by device physics of graphene transistors. The small signal parameters are extracted by running quasi static simulations for channel lengths down to 5nm. The small quasi static approximations are valid for graphene FETs when the frequency of interest is lower than the intrinsic cut-off frequency. The channel scaling behaviors of the unity current gain frequency f_T and unity power gain frequency f_{MAX} are studied under ballistic limit as well as in presence of optical phonon scattering. The rest of section addresses the effect of parasitic source and drain contact resistance on f_T and f_{MAX}.

Figure 2(a) shows the I_D-V_D characteristics at V_G=-0.6V. A kink behavior with a quasi-saturation region is observed in graphene FETs even at L_g=20nm.This quasi-saturation behavior is due to the drain Fermi level aligning with the Dirac point profile in the channel , followed by onset of ambipolar regime. The low density of states around the Dirac

 ISBN: 978-1-61208-214-1

point gives rise to decrease in current increment and explains the saturation observed for voltages where drain Fermi level is in vicinity of conduction band in channel. Since the density of states is low in a very small energy range around Dirac point, graphene FETs do not exhibit complete saturation seen in conventional silicon MOSFETs. The minimum output conductance needed for RF performance is exhibited in this quasi-saturation regime. The minimum output conductance simulated for ballistic condition is $g_{ds}\approx 5.96\times10^{3}\mu S/\mu m$. The value of the minimum output conductance is lowered in presence of optical phonon scattering. The minimum output conductance simulated for $\hbar\omega$=180meV and $\hbar\omega$=55meV is $g_{ds}\approx 4.92\times10^{3}\mu S/\mu m$ and $g_{ds}\approx 4.71\times10^{3}\mu S/\mu m$ showing 17.5% and 20.9% decrease respectively from ballistic value. The decrease of the minimal g_{ds} in presence of scattering affects the unity power gain frequency of GFETs.

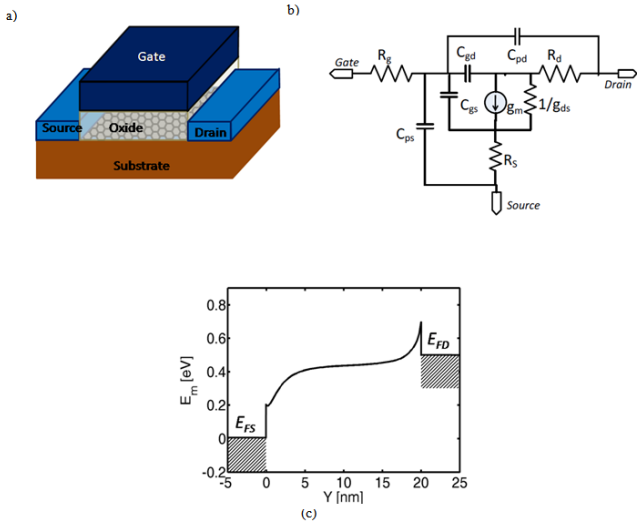

Figure 1. (a) Device structure for the modeled graphene FET. Pd is used as the contact material, Al_2O_3 is used as the insulator material, and its thickness is 2nm. (b) Small-signal equivalent circuit of GFET where g_m is the transconductance, g_{ds} is the output conductance, R_g is the gate resistance, R_s (R_d) is the source (drain) contact resistance, C_{gs} is the small signal gate to source capacitance, C_{gd} is the small signal gate to drain capacitance and C_{ps} (C_{pd}) is the parasitic capacitance . (c) Band profile of the GFET at V_D = -0.5V and V_G = -0.6V. The channel length is 20 nm and E_{FS} (E_{FD}) is the source (drain) Fermi level.

Figure 2(b) shows the I_D-V_G characteristics at V_D=-0.5V. In presence of optical phonon scattering the transconductance is degraded .The maximum simulated transconductance for ballistic condition is $g_m\approx 7.228\times10^{3}\mu S/\mu m$. While, the maximum simulated transconductance for $\hbar\omega$=180meV and $\hbar\omega$=55meV are $g_m\approx 4.669\times10^{3}\mu S/\mu m$ and $g_m\approx 4.3281\times10^{3}\mu S/\mu m$ showing 35.5% and 40.2% degradation respectively from ideal ballistic behavior.

The small signal analyses for graphene FETs is carried out using the equivalent circuit shown in Fig. 1(b) . The effect of parasitic capacitance has already been studied as part of earlier study. The small signal analyses require careful choice of DC bias conditions to get maximum value of f_T and f_{MAX}. Since graphene FETs exhibit quasi-saturation behavior, g_{ds} value is minimum only for very small drain bias voltage range. Therefore, the optimum DC bias point for simulations to ensure maximum f_T and f_{MAX} is chosen by running quantum quasi static simulations for g_{ds} as functions of V_D at different V_G values. Optimum bias point is taken to be a g_{ds} minima point in g_{ds} variation with drain voltage V_D at given gate voltage V_G . It can be extracted from Fig. 2(c). The minima point for g_{ds} is also dependent on V_G value chosen. Fig. 2(c) shows the g_{ds} minima point shifts to right from $V_D\approx$-0.3V at V_G=-0.4V to $V_D\approx$0.45V for V_G=- 0.6V in ballistic simulations. Similar behavior is replicated in presence of phonon scattering. Therefore, bias points are carefully chosen to be V_D=-0.5V and V_G=-0.6V which are optimized bias point values with minimum value of g_{ds} for all channel lengths from 50nm to 5nm under ballistic as well as in presence of scattering .

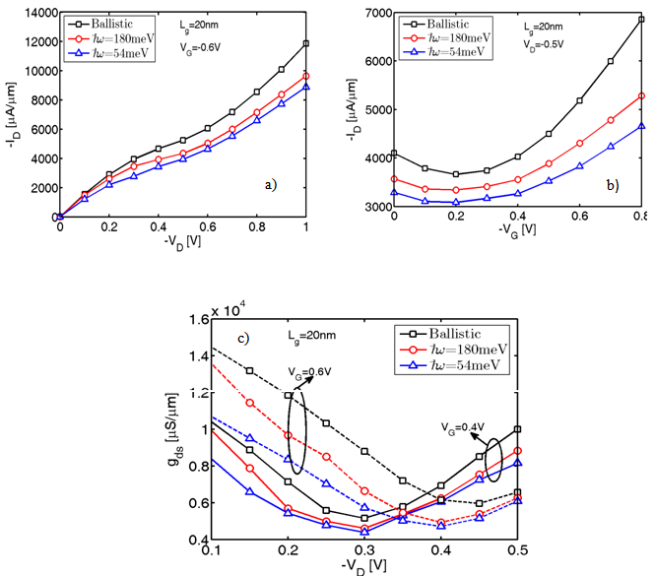

Figure 2. I-V characteristic of the GFET as shown in Fig.1(a) at the ballistic limit and with scattering. Inelastic phonon scattering is modeled for two different phonon energies $\hbar\omega$=54meV and $\hbar\omega$=180meV. The gate length is L_g=20nm. . (a) I_D versus V_D at V_G =-0.6V. (b) I_D versus V_G at V_D = 0.5V. (c) Output Conductance g_{ds} as a function of drain voltage, V_D at V_G =- 0.4V and- 0.6V, respectively.

Next part focuses on studying scaling of the small signal parameters at with the channel length under ballistic and scattering conditions. The gate to drain capacitance, C_{gd} and gate to source capacitances C_{gs} are calculated by running quasi static simulations at V_D=-0.5V and V_G=-0.6V. At a channel length above about 10nm, both C_{gd} as shown in Fig. 3(a) and C_{gs} as shown in Fig. 3(b) approximately linearly increases as the channel length increases. Scattering has a small effect on the values of the intrinsic capacitances compared to its effect on the transconductance. The total gate capacitance is the

 ISBN: 978-1-61208-214-1

serial combination of the gate insulator capacitance and the quantum capacitance, and it is estimated that the gate insulator capacitance is a more dominant factor than the quantum capacitance for the modeled device at this bias point.

The output conductance, g_{ds} increases with decrease of the channel length as shown in Fig. 3(c). The increase of the output conductance is due to the electrostatic short channel effects becoming more prominent at shorter channel lengths. Fig. 3(d) shows the transconductance g_m, as a function of the channel length. As the channel length scales from 50nm to 15nm, the ballistic transconductance only decreases very slightly from the value of about 8118µS/µm. As the channel length scales down to 5nm, the transconductance, however, drops significantly due to electrostatic gate effect already explained as part of earlier study. Similar electrostatic gate affected degradation of g_m below 15nm is observed in even in presence of inelastic phonon scattering. However, at gate lengths above 15nm, g_m decreases in presence of inelastic phonon scattering with increase in gate length. This is attributed to scattering becoming stronger at larger gate lengths. Since f_T as well as f_{MAX} are dependent on g_m, the degradation of g_m due to scattering is not favorable.

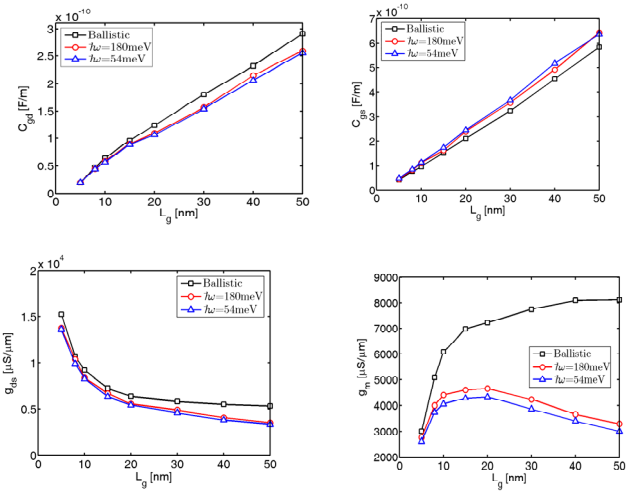

Figure 3. Extracted circuit parameters from quantum device simulations as a function of the gate length at V_D =-0.5V and V_G = -0.6V at the ballistic limit and in the presence of inelastic scattering with two different phonon energies $\hbar\omega$=54meV and $\hbar\omega$=180meV . (a) Small signal gate to drain capacitance C_{gd} (b) small signal gate to source capacitance C_{gs} (c) output Conductance g_{ds} and (d) transconductance g_m as function of channel length L_g.

Next, we examine the dependence of the unity current gain frequency f_T on channel length and scattering. Figure 4(a) shows that the intrinsic f_T increases with decrease in channel length down to 5nm due to smaller intrinsic gate capacitance Since g_m is degraded in presence of scattering, the same effect is manifested in lower f_T values in the presence of inelastic phonon scattering. The decrease in transconductance below 15nm is not reflected in f_T because the decrease in C_{gd} and C_{gs} with channel length outpaces the decrease in transconductance as shown part of earlier study[15]. The intrinsic unity power gain frequency, f_{MAX} as a function of channel length is examined in Fig. 4(b). Below 10nm, f_{MAX} falls off with decrease in channel length. This can be explained due to strong dependence of f_{MAX} on output conductance, g_{ds} and gate resistance R_g, which increase with the decrease in channel length .

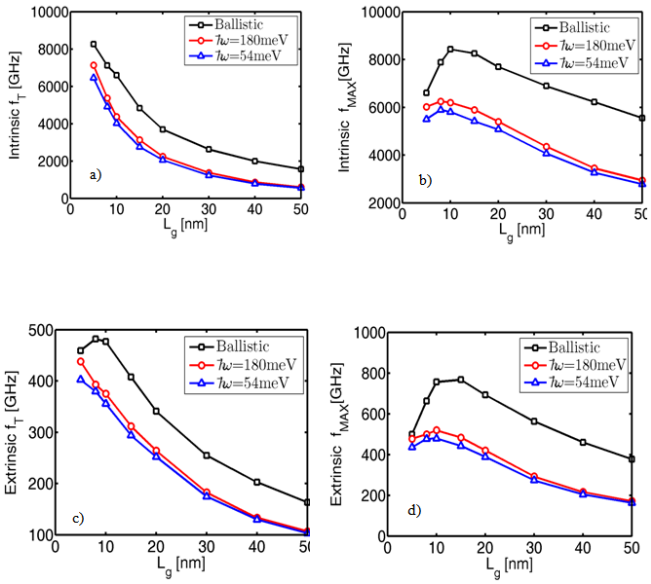

Figure 4. RF figures of merit of GFET vs. the gate length at V_D = -0.5V and V_G= -0.6V at the ballistic limit and in the presence of inelastic phonon scattering with phonon energies of $\hbar\omega$=54meV and $\hbar\omega$=180meV. (a) Intrinsic unity current gain frequency (the cutoff frequency) f_T (b) intrinsic unity power gain frequency (the maximum oscillation frequency) f_{MAX} , which is computed with zero source/drain parasitic capacitance and resistance (c) extrinsic unity current gain frequency f_T and (d) extrinsic unity power gain frequency f_{MAX} as a function of the gate length. The extrinsic frequencies are computed by considering a parasitic source and drain resistance of R_s=R_d = $500\Omega - \mu m$.

The RF performance is also limited by the parasitic contact resistance, which can limit the performance of FETs in real applications. Next, we study the extrinsic performance of graphene FETs including source and drain contact resistances in small signal equivalent model as shown in Fig. 1(b). However, the parasitic capacitance, C_{ps} (C_{pd}) shown in small signal model is assumed to be zero in all simulations. The effect of parasitic capacitance has already been studied as part of earlier study. The contact resistances are taken to be 500Ω-µm. The chosen value for contact resistance is typical for metal-graphene contacts reported in experiments at room temperature. Figure 4(c) shows extrinsic unity current gain frequency f_T in presence of source and drain contact resistances. The extrinsic f_T is less than intrinsic f_T shown in Fig. 4(b) by a factor of 15. Similarly extrinsic f_{MAX} is degraded

 ISBN: 978-1-61208-214-1

by a factor of 10 as shown in Fig. 4(d). Thus, the source and drain parasitic resistance can lower the RF performance of graphene FETs significantly. Therefore, the channel scaling should be complemented with reduced parasitic source and drain resistances to obtain good RF performance of graphene FETs.

It is found that better gate design can also improve f_{MAX} performance. The power gain frequency f_{MAX} is highly sensitive to the width of gate. We next studied graphene FETs performance with metal gate as shown in Fig. 5 for gate widths of 1μm and 10μm. The gate resistance for metal is calculated with R_{sh}=0.33 Ω/□ [24], α=1/3 is a constant for distributed gate resistance[25] and L_g =20nm. Changing gate width from *1*μm to *10*μm degrades the unity power gain frequency values considerably. Thus careful choice of gate width along with DC bias point is necessary to improve extrinsic f_{MAX} performance. In practice, width is limited by drain current and reducing the width is not feasible. The decreased gate resistance to improve extrinsic f_{MAX} performance can be realized by using multi-finger gates.

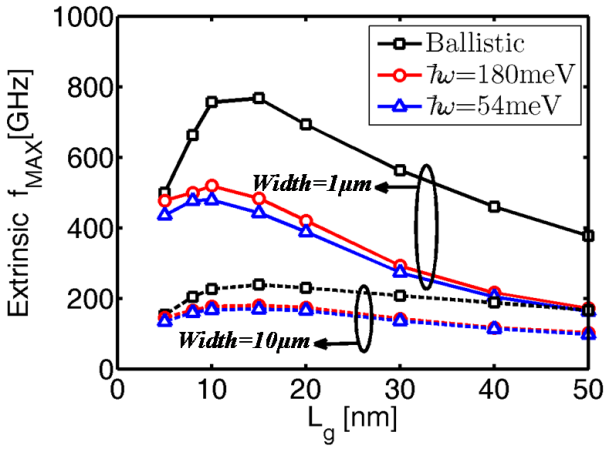

Figure. 5. The extrinsic unity power gain frequency f_{MAX} vs. channel length at the ballistic limit and in the presence of inelastic phonon scattering with phonon energies of $\hbar\omega$=54meV and $\hbar\omega$=180meV for transistor width =*1*μm(solid lines) and *10*μm(dashed lines). The modeled GFET with a channel length of 20nm is biased at V_D = -0.5V and V_G = -0.6V. The length of the gate is fixed at 20nm. The sheet resistivity of metal gate used here is 0.33 Ω/□.

IV. SUMMARY

In summary, the channel length scaling behavior of graphene FETs is studied to analyze RF performance metrics under ideal ballistic conditions and in presence of optical phonon scattering. The simulated intrinsic unity current gain frequency f_T increases to value of 5THz around L_g =10nm . However, the intrinsic power gain frequency, f_{MAX} is less than the unity current gain frequency. Including inelastic phonon scattering lowers both f_T and f_{MAX} due to degradation in g_m . Including the source and drain parasitic resistance lowers both unity current gain frequency as well as power gain frequency by several factors. Since drain and gain contact resistance is always present in real circuits, proper choice of the contact material is necessary to utilize full RF potential of graphene FETs. It is also proposed that careful choice of DC bias point and gate width is needed to get improved power gain frequency performance of graphene FETs.

REFERENCES

[1] K. S. Novoselov et al., "Electric field effect in atomically thin carbon films," *Science*, vol. 306, pp. 666–669, 2004.

[2] L. Liao, J. Bai, R. Cheng, Y. Lin, S. Jiang, Y. Qu, Y. Huang, and X. Duan, "Sub-100nm channel length graphene transistors," *Nano Lett*., vol. 10, pp. 3952-3956, 2010.

[3] Y. Wu et al., "RF perfomance of short channel graphene field-effect transistor," *Tech. Dig. of Int. Electron Device Meeting* (IEDM), pp. 226–228, 2010.

[4] J. Chauhan and J. Guo, "Assessmnet of high frequency performance limits of graphene field-effect transistors," *Nano Research,* Vol. 4, p. 571, 2011.

[5] S. Datta, "Quantum transport: atom to transistor," Cambridge University Press, 2005.

 ISBN: 978-1-61208-214-1

Effects of Microstructure on Fiber-Matrix Debonding of Metal Matrix Composites under Transverse Loading

Mohammad Tahaye Abadi
Aerospace Research Institute
Tehran, Iran
E-mail: abadi@ari.ac.ir

***Abstract*—A micromechanics damage model is presented to examine the effect of microstructures on the fiber–matrix debonding for unidirectional carbon fiber reinforced metal matrix composites under the transverse loading. Microstructure is represented by a repeating unit cell (RUC). Two fiber arrays are considered including ideal square fiber packing and random fiber packing defined by random sequential algorithm. A cohesive zone model is used to predict the onset of fiber–matrix debonding while the non-linear behavior in the matrix phase is modeled using the von-Mises plasticity theory. The micromechanical results show that the damage evolution starts at a lower stress level in the microstructure with random fiber packing compared to the regular microstructure and the transverse stress converges to the same level in both microstructures at high strain value. Micromechanical modeling procedure provides detail viewpoint into the microscopic damage accumulation prior to ultimate failure and highlights the different roles of the fiber–matrix debonding and matrix plasticity in the macroscopic response of the composite.**

Keywords-debonding; micromechanical modeling; transverse loading

I. INTRODUCTION

Metal matrix composites have found many applications as constructional and functional materials in different industries. The presence of reinforcement in metal matrix materials improves the properties such as the tensile strength, creep resistance, fatigue strength, thermal shock resistance, and corrosion resistance. Transverse strength of composite materials is one of the limiting design criteria in composite structures. Fiber-matrix interfaces are subjected to high local stress levels and have a greater propensity to undergo damage nucleation than those in dilute regions [1]. Transverse fracture is a result of fiber–matrix debonding and/or matrix micro-cracking which can induce further damages in laminates such as inter-ply delamination or fiber fracture in adjacent plies through the process of damage accumulation [2, 3]. Due to the complex nature of damage progression, many micromechanical studies have focused on transverse fracture behavior from viewpoint of damage initiation and evolution [4-7].

The micromechanics techniques yield information on both macroscopic and microscopic levels which are used for the prediction of the overall characteristics in view of continuum mechanics as well as the evaluation of the potential failure modes leading to the ultimate failure of heterogeneous materials [8, 9]. The micromechanical model provides an efficient procedure to determine and design the properties of composite materials.

Fiber-matrix interfaces have been modeled in a number of ways including a narrow region of continuum with graded properties, an infinitely thin surface separated by springs, and cohesive zones with specific traction–separation relations [6]. In the spring layer model [7], a stress based criterion for debonding and a frictional resistance based criterion for interfacial sliding have been used to capture debonding and sliding. Debonding is postulated to occur under the combined loading conditions at the interface. The cohesive zone approach is being increasingly used in describing fracture and failure behavior in a number of material systems [4, 5].

The transverse fracture behavior of composite materials depends on numerous contributing factors, such as constituent properties, interfacial strength, process related defects, and local morphological parameters like volume fraction, size, shape and spatial distribution of reinforcements. The present research works determines the influence of microstructure on the elastic-plastic properties of metal matrix composites considering the debonding at the fiber-matrix interface at high transverse loading. A micromechanical modeling procedure is implemented to evaluate the response of unidirectional continuous fiber composites subjected to finite axial deformation. The microstructure of the metal matrix materials is represented by a repeating unit cell (RUC) considering two fiber arrangements including ideal square fiber packing and random fiber packing defined by random sequential algorithm. The Volume averaging scheme is implemented to apply the local macroscopic deformation gradient tensor to the RUC assigned to the microstructure. The micromechanical modeling procedure is implemented for graphite/aluminum metal matrix composite in which the reinforcement behaves as elastic, isotropic solids and the matrix was modeled as an isotropic elastic-plastic solid following the von Mises criterion with isotropic hardening [10] and the Ramberg-Osgood relationship [11] is assumed between equivalent true stress and logarithmic strain. A cohesive zone model is used to predict the onset of fiber–matrix debonding, in which the damage initiation is defined based on the normal and shear strength at the interfacial zone. The damage evolution is model considering a exponential softening curve for the

 ISBN: 978-1-61208-214-1

degradation rate of the cohesive stiffness. The RUC is subjected to uniaxial deformation increased to a considerable value to evaluate both elastic and plastic behaviors of metal matrix composites. The yields strength and true elastic-plastic stress are determined for graphite/aluminum composites.

II. MICROSTRUCURE CONFIGURATION

The microstructures of unidirectional fiber reinforced composites are commonly described by three fiber arrangement including square, hexahedral and random fiber-packing patterns. The micromechanical results for linear anisotropic elastic materials revealed that the calculated elastic stiffness values for axial and shear deformation are dependent on the fiber packing [12]. Since the microstructures with square and hexahedral fiber-packing patterns are idealized geometrical representations for fiber arrangement, the microstructure with random fiber packing yields more accurate results. At large plastic deformation of anisotropic materials, the results highly depends on the fiber packing and for some fiber arrangement, the deformation locking may be observed at lower strain.

Since the heterogeneities are orders of magnitude smaller than the total body, the deformation field in the vicinity of one inclusion is approximately the same as the deformation field near neighboring inclusions [13]. Experimental observations [5-7] have shown that deformation field in the vicinity of a subvolume is approximately the same as deformation field of the near neighboring subvolumes. The size of subvolume is small enough compared to the total microstructure size so that the effective properties computed from the subvolume are independent of its size and position within the microstructure. Therefore, the microstructure is represented by a periodic unit cell that deforms in a repetitive way. The periodic modeling can be quite useful, because it provides rigorous estimations with a priori prescribed accuracy for various material properties.

Microstructure shown in Fig. 1 is considered for the unidirectional continuous fiber composites. The circular fibers with identical radius are dispersed in the microstructure in a random and isotropic manner. It is assumed that the composite material has a periodic microstructure which can be obtained by translating RUC along three orthogonal axes. The fiber distribution in the unit cell is generated using the random sequential adsorption algorithm [14] which ensures a random, isotropic and homogeneous distribution for the fibers within the RUC. The random coordinates in the cross-section of microstructure are generated for the center of circular fibers with specific diameter, denoted by d. When a fiber intersects the boundaries of unit cell, another fiber is generated on the neighboring unit cell in order to obtain periodic unit cell. The new fiber is added to the microstructure when the distance between the center of a given fiber and the closest fibers previously generated is greater than a minimum values ($1.1d$). Such condition prevents overlapping fibers as well as ensuring adequate mesh geometry for the matrix material located between fibers. To prevent element distortion during mesh generation, the fiber surface should not be too close (greater than 0.1d) to the boundary surfaces of the RUC. When such conditions are satisfied, the fiber is added to the unit cell at the generated random coordinates. The procedure is repeated until the fiber volume fraction reaches close to a pre-defined value. The square cross section is considered for unit cell ($b_2 = b_3$) and the ratio of fiber diameter to unit cell dimension ($d / 2b_2$) is set to 0.05.

III. MICROMECHANICAL MODEL

Micromechanical model provides efficient tool to characterize composite materials from known properties of their constituents and the distribution of the reinforcement in the microstructure through the analysis of a RUC. The essence in micromechanical approach is to replace the heterogeneous structure of the composite by a homogeneous medium with anisotropic properties.

A Lagrangian viewpoint is used to describe the material motion and the components of vectors and tensors are described in a fixed rectangular coordinate system. In the reference configuration of RUC, the position of a typical material particle is expressed with vector $\mathbf{X}$ (components X_i). In the deformed configuration at instance t, the particle moves to a position described with vector $\mathbf{x}_{(\mathbf{X},t)}$ (components x_i) corresponding to the displacement vector $\mathbf{u}_{(\mathbf{X},t)}$ (components u_i). The deformation is typically described using the deformation gradient tensor, designated by $\mathbf{F}$, whose components are given by

$$F_{ij} = \frac{\partial x_i}{\partial X_j} \tag{1}$$

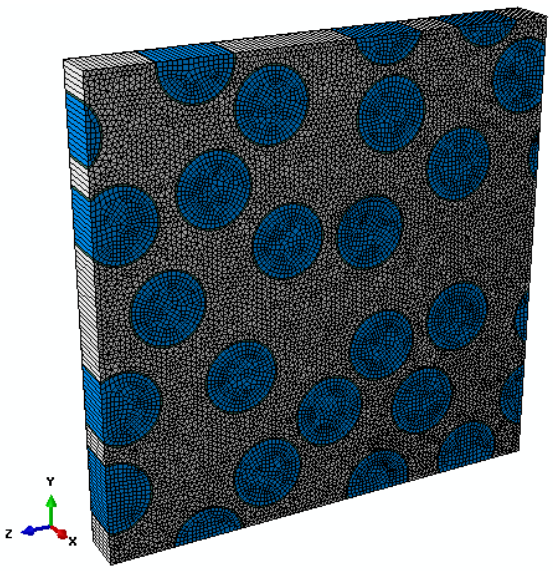

Figure 1. Microstructure of metal matrix composite with random fiber packing.

The reference geometry of RUC is assumed to be a rectangular prismatic volume whose surfaces are parallel to the surfaces defined in a fixed Cartesian coordinate system with origin located at the centre of RUC. The initial dimension of RUC is $2b_1 \times 2b_2 \times 2b_3$. The boundary surfaces of reference geometry perpendicular to *i*-axis are designated with S_i^+ and S_i^- intersecting i-axis at $X_i = +b_i$ and $X_i = -b_i$, respectively. The displacement of the points located on each boundary surface is measured respect to corner points labeled as points P_0, P_1, P_2 and P_3. Such points are called reference points. The current position of points located on surface Si– is measured respect to point P0, while the position of points located on S_1^+, S_2^+ and S_3^+ is measured respect to points P_1, P_2 and P_3, respectively. To enforce the periodicity constraint, the current position of boundary surface is described by [9]:

$$x_{i(-b_1,X_2,X_3,t)} - x_{i(t)}^{(0)} = x_{i(b_1,X_2,X_3,t)} - x_{i(t)}^{(1)} \quad i = \{1,2,3\} \quad (2a)$$

$$x_{i(X_1,-b_2,X_3,t)} - x_{i(t)}^{(0)} = x_{i(X_1,b_2,X_3,t)} - x_{i(t)}^{(2)} \quad i = \{1,2,3\} \quad (2b)$$

$$x_{i(X_1,X_2,-b_3,t)} - x_{i(t)}^{(0)} = x_{i(X_1,X_2,b_3,t)} - x_{i(t)}^{(3)} \quad i = \{1,2,3\} \quad (2c)$$

where $x_{i(t)}^{(j)}$ are the components of current position vector of corner point P_j.

To relate the macrostructure deformation to the microstructure deformation, it is assumed that the local macroscopic deformation gradient tensor at a given point to be equal the volume average deformation gradient tensor of RUC assigned at that point. Using the periodicity constraining equations (1), it can be shown [9] that the macroscopic deformation gradient tensor is a function of current position of corner points P_0, P_1, P_2 and P_3 as follows:

$$F_{ij} = \frac{x_i^{(j)} - x_i^{(0)}}{2b_j} = \frac{u_i^{(j)} - u_i^{(0)}}{2b_j} + \delta_{ij} \quad (3)$$

It should be noted that no summation is considered on *j* superscript in Eq. (3).

An energy balance is considered to relate stress tensor in the macroscopic and microscopic scales. The internal power at macroscopic level at a given point is set equal to the internal power in RUC assigned at the corresponding point in a given deformed configuration. It was shown [9] that the energy balance results in

$$\sum_{j=1}^{3}\sum_{i=1}^{3} \dot{F}_{ji} P_{ij} = \sum_{j=1}^{3}\sum_{i=1}^{3} \frac{1}{S_i^+} \dot{F}_{ji} \int_{s_i^+} t_j ds \quad (4)$$

where the dot superscript denotes to the time derivative, P_{ij} are the components of nominal stress tensor defined in macroscopic levels, t_j are the components of traction force and s_i^+ is the deformed geometry of boundary surface S_i^+.

IV. MATERIAL BEHAVIOR

Aluminum alloy reinforced with stiff graphite fibers is considered. The fibers behaved as elastic, isotropic solids characterized by the elastic modulus $E_f = 250$ GPa and the Poisson's ratio $\upsilon_f = 0.2$. The matrix is modeled as an isotropic elastic-plastic solid following the von Mises criterion with isotropic hardening [10]. The matrix elastic constants are $E_m = 70$ GPa and $\upsilon_m = 0.33$, and the Ramberg-Osgood relationship [11] is assumed between equivalent true stress, σ_m^{eq}, and logarithmic strain, ε_m, i.e.,

$$\varepsilon_m = \left(\frac{\sigma_m^{eq}}{K} \right)^{1/n} \quad (5)$$

where $K = 400$ MPa is the strength coefficient and $n = 0.1$ is the matrix strain hardening exponent [14]. Regarding these data, an initial yield stress of 225.3 MPa is obtained. The aluminum material is reinforced with 0.4 fiber volume fraction.

The damage initiation is defined based on the normal and shear strengths of the cohesive zone in the fiber-matrix interface. Damage is assumed to initiate when the maximum nominal stress ratio reach to a unit value, namely,

$$\max\left(\frac{\langle t_n \rangle}{t_n^0} + \frac{t_s}{t_s^0} + \frac{t_t}{t_t^0} \right) = 1 \quad (6)$$

where symbol < > is Macaulay brackets [15] to signify that a pure compressive deformation or stress state does not initiate damage, t_n^0 and t_s^0 are the normal and shear strengths of the fiber-matrix interfacial zone, respectively. The damage evolution law describes the degradation rate of the cohesive stiffness when the criterion of damage initiation is reached. A scalar damage variable, *D*, is introduced to characterize the stiffness degradation as follows:

$$t_n = \begin{cases} (1-D)K_n\delta_n & \delta_n \geq 0 \\ K_n\delta_n & \delta_n < 0 \end{cases} \quad (7a)$$

$$t_s = (1-D)K_s\delta_s \quad (7b)$$

$$t_t = (1-D)K_t\delta_t \quad (7c)$$

The initial value of scalar damage variable is zero before the damage initiation and it is continuously increased up to a unit value as the debonding occurs in the fiber-matrix interface. The damage evolution is modeled based on the level of applied traction or displacement. To describe the evolution of damage under a combination of

 ISBN: 978-1-61208-214-1

normal and shear deformation across the interface, it is useful to introduce an effective displacement defined as [15]

$$\delta_{eq} = \sqrt{\langle \delta_n \rangle^2 + \delta_s^2 + \delta_t^2} \quad (8)$$

A exponential softening curve is considered to model damage evolution at the interface once the maximum stress ratio becomes greater than unit value. The element stiffness reduces until complete failure when the effective displacement reaches to a specific value (δ^f), as shown in Fig. 2. The area under the traction separation determines the fracture energy of cohesive material.

V. RESULTS

Based on the fiber volume fraction of 0.4, the radius of fiber for microstructure with square fiber packing is $0.714b_2$. The fiber-matrix interaction is assumed to be a ring with negligible thickness set to $0.01b_2$ and the internal surface of ring is tied to the external surface of fiber. The behavior of the fiber–matrix interface is modeled using cohesive elements introducing a displacement discontinuity at the interface when the local stress reaches to the debonding critical condition. A traction–separation law is considered for the fiber-matrix interface to relate the displacement between the top and bottom faces of the cohesive element to the applied normal and shear traction vectors. An initial elastic stiffness was used to ensure the displacement continuity at the interface in the absence of damage. Based on the elastic stiffness values for axial and shear deformation of matrix material and the initial thickness of fiber-matrix interface, the axial and shear stiffness values are set to 70.0×10^{14} Pa/m and 26.3×10^{14} Pa/m, respectively.

A. Transverse Loading without Damge Evolution

To validate the number of cohesive elements and the corresponding properties of the fiber-matrix interface, the elastic-plastic response is examined before damage initiation for the microstructure with cohesive elements having a perfect bonding between the fiber and matrix materials. The material behavior should be the same in both microstructures before damage evolution. The RUC is subjected to axial transverse strain up to 5% to observe the elastic-plastic behavior of metal matrix composites. The micromechanical modeling procedure is used to apply axial transverse strain to the RUC of the microstructures with random and ideal square fiber packing patterns. The perfect bonding between the fiber and matrix causes considerable distortion in matrix elements at the vicinity of fibers. The presence of cohesive elements considered in the fiber-matrix interface permits radial or tangential separations between fiber and matrix material as the traction vectors exceed a specific critical value. Since no damage evolution criterion is considered in the cohesive elements, the cohesive elements are deformed without decreasing stiffness. When lower axial and shear stiffness values are selected for cohesive elements, negligible strain is observed in the matrix and fiber materials and the deformation is limited to the cohesive elements and low stress value is determined for composite material. More axial and shear stiffness values considerably reduce the deformation of cohesive elements and simulate perfect bonding at the fiber-matrix interface. The higher stiffness of cohesive elements causes that the numerical procedure tends to diverge when the damage evolution is considered. Fig. 3 illustrates the Cauchy stress-strain curves obtained for RUC with cohesive elements in the microstructures with square and random fiber packing patterns. Since negligible difference is observed between graphs obtained for each microstructure, the presence of cohesive elements predicts the response of perfect microstructure. Both microstructures predict the same yield strength for composite materials. Since the fibers can move between each other in axial deformation of the microstructure with random fiber packing, lower stress requires applying plastic strain compared to microstructure with square fiber-packing.

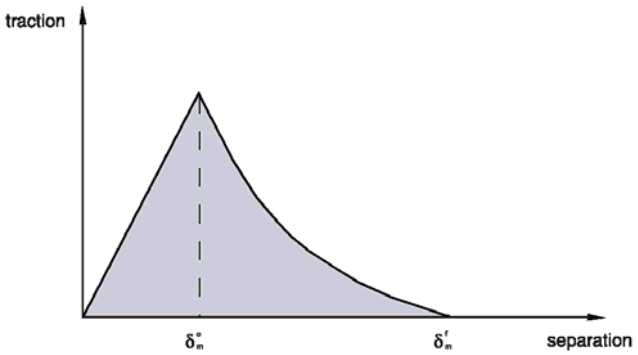

Figure 2. Traction–separation behaviour of cohesive elements.

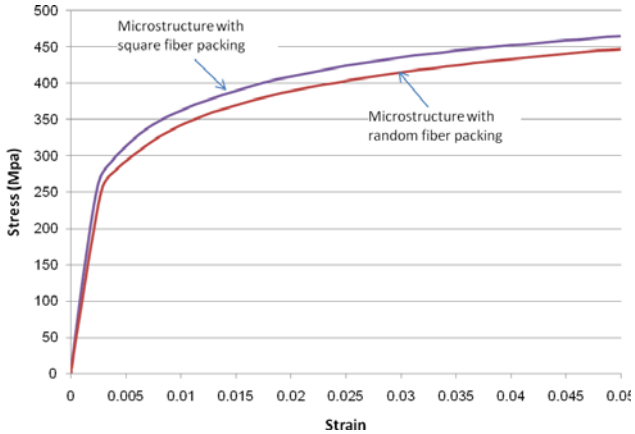

Figure 3. Cauchy stress required to applied elastic-plastic tensile transverse deformation to graphite/aluminum composite with different microstructures.

 ISBN: 978-1-61208-214-1

B. Transverse Loading with Damge Evolution

The damage initiation is defined based on the normal and shear strengths of the cohesive elements considered at the fiber–matrix interface in graphite/aluminum metal matrix composite. The shear strength is related to the normal strength as $t_s^0 = t_t^0 = t_n^0/\sqrt{3}$ and the normal strength is varied to evaluate the effects of bonding strength on stress-strain graph of composite material. The fiber-matrix debonding is assumed to be occurred when the effective displacement reaches to 100 μm. The interfacial fracture energy in Mode I and II can be calculated based on the area under the traction-separation curve. Fig. 4 illustrates the deformed geometry of RUC considered for microstructures with square and random fiber packing patterns, in which the normal strength of cohesive zone is 200 MPa. The deformation of RUC corresponds to the local macroscopic transverse strain of 0.02 which leads to the dobonding in the fiber-matrix interface considering normal strength of t_n=100 MPa. In the microstructure with regular square packing, the applied tensile strain causes that lateral compressive stress is observed in the cohesive zones at the plane normal to the loading direction. Since the cohesive failure is insensitive to compressive stress, no separation is observed at this region, as shown in Fig. 4a. On the other hand, the interface starts to separate at the plane parallel to the loading direction located on the lines at the top and bottom surfaces of fiber because of cohesive failure at the tensile loading. After the separation at top and bottom surface of fiber, combined tensile and shear loadings are applied to the cohesive elements causing to propagate the separation toward the plane normal to the transverse loading. In the microstructure with random fiber packing, there is no symmetry for loading condition of fibers and the fiber-matrix separation may be observed at different points, as observed in Fig. 4b.

The stress-strain curves of the graphite/aluminum metal matrix composite are shown in Fig. 5 considering the damage evolution in the fiber-matrix interface. The graphs start with a linear elastic region with the same transverse elastic modulus. Based on the normal strength of cohesive elements, nonlinear plastic deformation is observed at different stress levels. As shown in Fig. 5a, the stress-strain graphs of RUC with regular fiber packing have abrupt stress falls as the debonding occurs, because the applied stress to the fiber drops and the matrix should carry the transverse loading. Since the matrix is the only material subjected to the transverse loading when the complete debonding occurs in the fiber-matrix interface, the stress level decreases to the same level in different values for cohesive strength. The transition between ideal stress-strain graph to stress level in the matrix material is observed in more strain for cohesive material with higher strength. The multiple stress drops are observed for the microstructure with random fiber packing, as shown in Fig. 5b. Each stress drop corresponds to the initiation of matrix separation from the fibers distributed in the microstructure. Since progressive damage correlates with the experimental observation, the micromechanical modeling yields accurate results for microstructure with random fiber packing

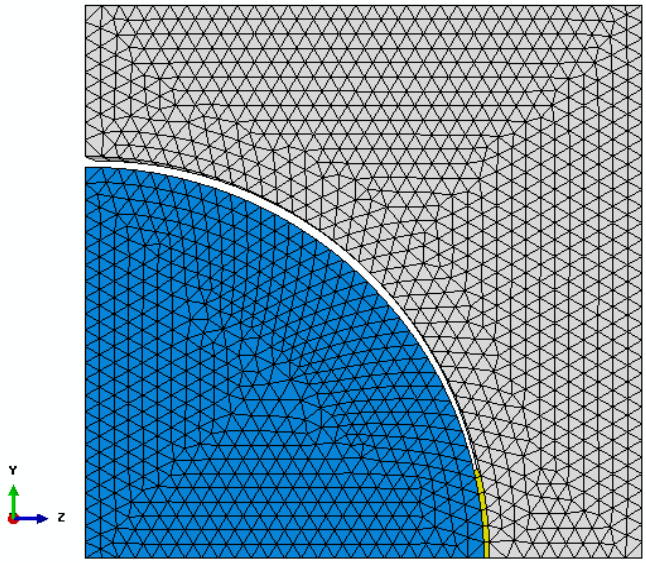

(a)

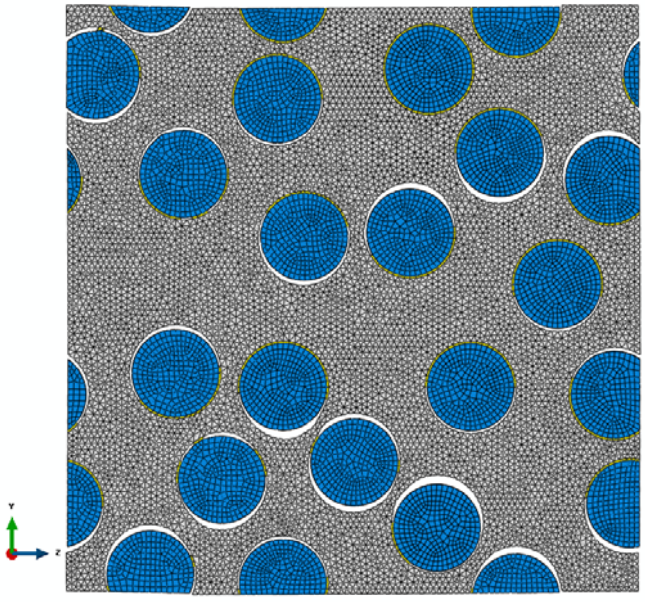

(b)

Figure 4. Deformed geometries of matrix, fiber and cohesive elemets subjected to tensile axial deformation normal to fiber direction in the RUC of graphite/aluminum composite having 0.4 fiber volume fraction and tn=100 MPa and microstructures with a) square fiber packing b) random fiber packing.

 ISBN: 978-1-61208-214-1

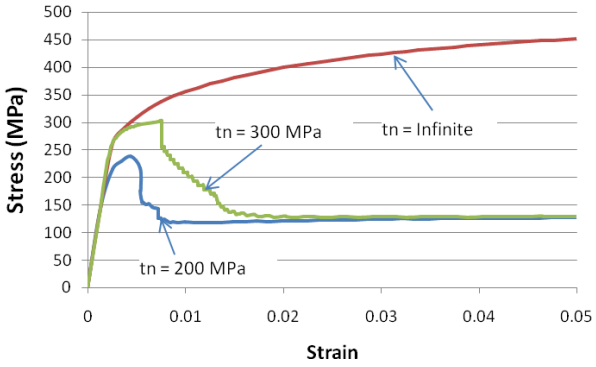

Figure 5. Cauchy stress required to applied elastic-plastic tensile transverse deformation to graphite/aluminum composite in different strength of fiber-matrix interface for microstructures with a) square fiber packing b) random fiber packing.

VI. CONCLUSIONS

The local fiber distribution significantly affects the interfacial stress state and the onset and evolution of fiber–matrix debonding. As the local damage is initiated at the fiber-matrix interface of the microstructure with ideal square fiber packing, it propagates to the total interfacial zone for a negligible strain increase. In the microstructures with ideal square fiber packing, the stress drop is observed in the stress-strain curve due to stress releasing in the fiber materials. As the complete debonding occurs in the fiber-matrix interface, the matrix is the only material subjected to the transverse loading. Therefore, the stress level decreases to the same level for microstructures having cohesive elements with different strength values. Progressive damage evolution is observed in the fiber-matrix interfaces of the microstructure with random fiber packing, in which each stress drop corresponds to the initiation of matrix separation from the fibers distributed in the microstructure. The transition between ideal stress-strain curves to stress levels in the matrix material is observed in more strain for cohesive material with higher strength. The damage evolution starts at lower stress level in the microstructure with random fiber packing compared to the regular microstructure and the transverse stress converges to the same level in both microstructures at high strain value.

REFERENCES

[1] S. Ghosh, Y. Ling, B. Majumdar, and R. Kim, “Interfacial debonding analysis in multiple fiber reinforced composites”, Mechanics of Materials, vol. 32, pp. 561-591, October 2000

[2] T. Hobbiebrunken, M. Hojo, T. Adachi, C. De Jong, and B. Fiedler, "Evaluation of interfacial strength in CF/epoxies using FEM and in-situ experiments", Composite Part A – Applied Science, vol. 37(12), pp. 2248–56, December 2006.

[3] EK. Gamstedt and BA. Sjögren, “Micromechanisms in tension–compression fatigue of composite laminates containing transverse plies”, Composite Science Technolgy, vol. 59(2), pp. 167–78, February 1999.

[4] T.J. Vaughan and C.T. McCarthy, “Micromechanical modelling of the transverse damage behavior in fiber reinforced composites”, Composite Science Technolgy, vol. 71, pp. 388–396, February 2011.

[5] E. Totry, C. González, and J. Llorca. “Failure locus of fiber-reinforced composites under transverse compression and out-of-plane shear”, Composite Science Technolgy, vol.68(3–4), pp. 829-39, March 2008.

[6] N. Chandra, H. Li, C. Shet, and H. Ghonem, “Some issues in the application of cohesive zone models for metal–ceramic interfaces”, Int J Solids Structure, vol. 39, pp. 2827–2855, May 2002.

[7] N. Chandra and H. Ghonem, “Interfacial mechanics of push-out tests: theory and experiments”. Composite Part A – Applied Science, vol. 32 (3–4), pp. 575–584, March–April 2001.

[8] M-J. Pindera, H. Khatam, A.S. Drago, and Y. Bansal, “Micromechanics of spatially uniform heterogeneous media: A critical review and emerging approaches”, Composite Part B, vol. 40, pp. 349–378, July 2009.

[9] M.T. Abadi, “Micromechanical modeling of heterogeneous materials at finite strain,” in Wiley Encyclopedia of composite, Nicolais, A. Borzacchiello, Wiley, 2012, pp. 1778–1791.

[10] R. von Mises, "Mechanik der festen Körper im plastisch deformablen Zustand. Göttin", Nachr. Math. Phys., vol. 1, pp. 582–592, 1913.

[11] W. Ramberg and W. R. Osgood, "Description of stress-strain curves by three parameters". Technical Note No. 902, National Advisory Committee For Aeronautics, Washington DC, 1943.

[12] A. A. Gusev, P. J. Hine, and I. M. Ward, “Fiber packing and elastic properties of a transversely random unidirectional glass/epoxy composite”, Composite Science Technology, Vol. 60 (4), pp. 535-541, March 2000.

[13] R.J.M. Smit, W.A.M. Brekelmans, and H.E.H.Meijer, “Prediction of the mechanical behavior of nonlinear heterogeneous system by multi-level finite element modeling”, Computer Methods Applied Mechanic. Eng. vol. 155, pp. 181-192, March 1998.

[14] J.S. Wang, “Random sequential adsorption, series expansion and Monte Carlo simulation”, Physics A, vol. 254, pp. 179–184, May 1998.

[15] P.P. Camanho and C.G. Davila, Mixed-mode decohesion finite elements for the simulation of delamination in composite materials, NASA/TM-2002-211737, Langley Research Center, Hampton, Virginia, June 2002.

 ISBN: 978-1-61208-214-1

The Evaluation Polymeric Nanocomposites from Nuclear Magnetic Resonance Relaxometry

Maria Inês B. Tavares, Paulo Sérgio Rangel C. da Silva, Emerson Oliveira da Silva, Cíntia Legramanti, Adriano Alves Passos, Roberto P. Cucinelli Neto
Universidade Federal do Rio de Janeiro, Instituto de Macromoléculas Professora Eloisa Mano
UFRJ - IMA
Rio de Janeiro, Brasil
e-mail: mibt@ima.ufrj.br; rangel@ima.ufrj.com; eos@ima.ufrj.br; cintia.legramanti@gmail.com; adriano.passos@clariant.com; robertoneto@ima.ufrj.br

Abstract— **Solid-state Nuclear Magnetic Resonance (NMR) has many techniques that include hydrogen nuclear relaxation times, such as: spin-lattice relaxation time in the laboratory frame (T_1H) and spin-lattice relaxation in the rotating frame ($T_1\rho H$). These relaxation parameters involve changes in thermal equilibrium of spin systems and the hydrogen relaxation times can be measured directly, using low-field NMR. The efficiency of the process can be correlated with the structure and the value is intrinsically related to the system's morphology; consequently, the relaxation times can be used to evaluate the nanoparticles' dispersion in the polymer matrix; the interaction between both nanocomposite components; the molecular dynamic of the hybrid compounds and also the molecular domains formation in an organic material. This feature makes these techniques good tool to analyze the molecular dynamics of polymer systems, as well as the nanocomposites. In this work, we want to show the evaluation of polymeric nanocomposites formation employing the determination of proton spin-lattice relaxation time, using low-field nuclear magnetic resonance. The nanocomposites were mainly characterized by solid state nuclear magnetic resonance relaxometry through the determination of proton spin-lattice relaxation time. The determination of this parameter was carried out to evaluate the organoclay exfoliation and intercalation process in the polymeric matrix, for samples using organoclay as a nanoparticle, as well as the dispersion and distribution of them along the macromolecular chains; this parameter was also used to detect the dispersion and distribution of the spherical and tubular nanoparticles in the polymeric matrix. The proton NMR relaxation data showed that the polymeric nanomaterials investigated presented good nanoparticle dispersion and the distribution, as well as the intermolecular interactions between hybrids components.**

Keywords - polymeric nanocomposites; nanoparticles; rexalation times; nuclear magnetic resonance

I. INTRODUCTION

The solid-state nuclear magnetic resonance [1] is a spectroscopy that comprehends many techniques, one of them is the hydrogen nuclear relaxation times, such as: spin-lattice relaxation time in the laboratory frame, promotes evaluation of the samples in the MHz scale and spin-lattice relaxation in the rotating frame is sensitive to the movements in the tens of kilohertz [1-3]. Both relaxation parameters involve changes in thermal equilibrium of spin systems and the responses of them are intrinsically related to the system's molecular dynamic that is derived from the morphology [4-6]. Consequently, the relaxation measurements can be used to evaluate the nanoparticles' dispersion in the polymer matrix, the interaction between both nanocomposite components, the molecular dynamic of the hybrid compound and also the molecular domains formation in an organic material [7-9]. This feature makes these techniques a good tool to analyze the molecular dynamics of polymer systems, as well as the nanocomposites [8-11].

In this work, we want to show the evaluation of polymer nanocomposites employing proton spin-lattice relaxation time, using the proton relaxation parameter employing low-field nuclear magnetic resonance.

This work will present the evaluation of different nanostructured materials based on synthetic and biopolymers as well distinct nanoparticles by the use of nuclear magnetic resonance relaxometry to obtain responses on the intermolecular interactions and the dispersion and distribution of the nanoparticles in the polymer matrix

II. EXPERIMENTAL

A. NMR relaxation measurements

The relaxation time was analyzed in a MARAN Ultra low-field NMR (LF-NMR) spectrometer (Oxford Instruments, Oxford, UK), using an 18 mm NMR tube, operating at 23 MHz for the hydrogen nucleus. The pulse sequence used to obtain the spin lattice relaxation time data was inversion-recovery (recycle delay - 180° - τ - 90° - acquisition data) and the 90° pulse of 4.5μs was calibrated automatically by the instrument's software. The amplitude of the FID was sampled for twenty τ data points, ranging from 0.01 to 5000 ms, using 40 data points and 4 scans for each point. The same sample was analyzed at 27 ºC. The relaxation values and relative intensities were obtained by fitting the exponential data with the aid of the WINFIT program. Distributed exponential fittings as a plot of relaxation amplitude versus relaxation time were performed by using the WINDXP software. Both WINFIT and

 ISBN: 978-1-61208-214-1

WINDXP are commercial programs and come with the low-field NMR spectrometer.

All solid-state NMR spectra were obtained on a VARIAN spectrometer, UNIT-Plus, 9.4 Tesla, operating at 104 MHz for ^{13}C nuclei and 79.49 MHz ^{29}Si. The samples were packed in a 7mm zirconia rotor that was spun in the magic angle at about 6 kHz for the carbons-13 nucleus. The ^{13}C cross polarization magic angle spinning (CPMAS) were first done to obtain the conditions to apply the variable contact time experiment (VCT), which were carried out using 2 s of recycle delay with the increase of contact-times varying from 100 to 8000μs, the hydrogen decoupling field strength was 40 KHz. From this experiment it was also determined the values of proton spin-lattice relaxation time in the rotating frame ($T_1\rho H$), which is indirectly determined from the intensity decay of each resolved carbon. Hexamethyl benzene (HMB) was used as external standard; the methyl carbons were assigned as 17.3 ppm.

III. RESULTS AND DISCUSSION

A. *Evaluation of PHB-organoclay systems obtained by solution*

Low-field NMR analyses were used to determine the proton spin-lattice relaxation time for the PHB/viscogel B8 nanocomposites. Table I shows the proton T_1 relaxation values of the PHB/viscogel B8 nanocomposites, the nanostructure materials were obtained through intercalation solution method.

TABLE I. HYDROGEN NUCLEAR RELAXATION VALUES FOR THE NANOCOMPOSITES OF PHB/VISCOGEL B8

PHB/Viscogel B8	T_1H (ms)
0/100	683
99/1	654
97/3	570
95/5	**440**
93/7	489
90/10	487

A decreased in the proton relaxation value with the increased of organoclay comes from the exfoliation process that occurs predominantly comparing to intercalation process. This statement is confirmed by the presence of metals in the clay lamellae that are agent that promotes the proton relaxing acceleration as the polymer chains are around the clay lamellae, confirming the for changes occurred the in polymer and clay structures after a polymeric nanocomposite being formed. Up to 5% a decreased in the T_1H is due to the exfoliation process, after this proportion the values are still lower than the polymer matrix, due to the same effect, but they began to increase, because some intercalation process is being done due to the large amount of organoclay to be exfoliated, dispersed and distribution in the polymer matrix.

The proton NMR relaxation data showed that the polymer nanomaterials investigated presented good nanoclay dispersion in the polymeric matrix, promoting a formation of mixed nanocomposite structure containing part exfoliated and part intercalated.

B. *Evaluation of HIPS-organoclay systems obtained by solution*

The nanocomposites obtained were mainly characterized by solid state nuclear magnetic resonance relaxometry, through T_1H measurements. The determination of proton spin-lattice relaxation time was carried out to evaluate the clay exfoliation and intercalation. The relaxation determination was done in a low-field NMR spectrometer. Tables II and III show the T_1H data for the polymer system containing S4 and S7, respectively, as nanoparticles. S4 contains Bis (Hydrogenated Tallow Alkyl) Dimethyl Ammonium (BHTADMA) as a surfactant and S7 contains Dimethyl Benzil Hydrogenated Tallow Ammonium (DMBHTA) as a surfactant.

TABLE II. PROTON SPIN-LATTICE RELAXATION FOR HIPS AND THEIR NANOCOMPOSITES WITH S4

Samples	T_1H (ms)
HIPS	504
HIPS41	483
HIPS42	**463**
HIPS43	479
HIPS45	507

TABLE III. PROTON SPIN-LATTICE RELAXATION FOR HIPS AND THEIR NANOCOMPOSITES WITH S7

Samples	T_1H (ms)
HIPS	504
HIPS71	503
HIPS72	**434**
HIPS73	468
HIPS75	449

According to the relaxation time values listed in both Tables II and III, independently of organoclay type used, the best quantity of nanoparticle to be well dispersed and distributed in the polymer matrix was 2%, in this proportion higher degree of exfoliation process occurred, due to the decrease in the relaxation time, because of the relaxing effect of the paramagnetic metal present in the clay structure. These metals influence direct in the protons relaxation decreasing it, which confirms the exfoliation process.

 ISBN: 978-1-61208-214-1

C. Evaluation of PLA-silica systems obtained by solution

Two silica types A200 (hydrophilic) and R972 (hydrophobic) were incorporated in the PLLA matrix [11] and both silica types caused changes in T_1H values due to the changes in the molecular mobility, as a consequence of nanoparticle dispersion and distribution in the polymer matrix. Table IV shows the T_1H values for the PLLA (pellet), 5% PLLA and their nanocomposites with A200 and R972 silica.

TABLE IV. T_1H VALUES FOR THE PLLA (PELLET), 5% PLLA AND THEIR NANOCOMPOSITES WITH A200 AND R972 SILICA.

Sample	T_1H
5% PLLA	630
5% PLLA + 0.5 mg A200	657
5% PLLA + 1mg A200	671
5% PLLA – 0.5mg R972	681
5% PLLA - 1mg R972	660

The effects of 0.5mg of both silica type A200 and R972 were comparable. However, comparing the addition of the samples with 1mg of A200 or R972, the effect of this quantity of silica in the system containing A200 was stronger than the system with 1mg of R972.

For film formed from 5% PLLA an increase in the quantity of R972 decreased the T_1H, which is derived from the dispersion of the silica, this system has an opposite behavior compared to A200 addition.

Therefore, both silica types had promoted changes in the relaxation time as a consequence of silica dispersion and distribution in the polymer matrix. This confirms that the relaxation time parameter was effective to show the effect of nanoparticles with spherical form, such as silica.

D. Evaluation of EVA-silica systems obtained by melting processing

The evaluation of EVA-silica system was evaluated by the determination of proton spin-lattice relaxation time in the rotating frame, $T_1\rho H$, it was determined through the decay of the resolved carbons with the increasing of the contact-times, obtained during the VCT experiment. The values of this parameter are listed in Table V.

TABLE V. $T_1\rho H$ VALUES FOR EVA AND THE MEMBRANES WITH SiO_2 5% AND SiO_2 20%, FOR THE CARBON LOCATED AT 34 PPM (CH_2 FROM EVA MATRIX)

Samples	$T_1\rho H$ (ms) 34 ppm
EVA	2
EVA/SiO_2 5%	**1**
EVA/SiO_2 20%	2

The decrease of 50% in the $T_1\rho H$ value for the EVA chains in the EVA/SiO_2 5% nanocomposite shows that the EVA chains are interacting intimately with SiO_2, as a consequence of the silica oxide has being well dispersed and distributed in the polymer matrix, which causes a decreases in the $T_1\rho H$ parameter due to the decrease in the spatial proximity, promoting a strong intermolecular interaction. Analyzing the EVA/SiO_2 20% $T_1\rho H$ value, no change in the parameter value was found comparing to EVA itself, indicating an occurrence of phase separation, because the quantity of silica is high to be well dispersed and distributed in the polymer matrix, as a consequence an agglomeration of silica particles occurs.

E *Evaluation of EVA-carbon nanotubes system obtained by solution method*

The relaxation parameter was also used to evaluate the polymer nanocomposite when the nanoparticle has a tubular form, such as carbon nanotubes.

Table VI shows the proton spin-lattice relaxation time evolution of EVA-carbon nanotubes modified with carboxylic acid system, varying the proportion of carbon nanotubes; these systems were prepared by solution dispersion method.

TABLE VI. PROTON SPIN-LATTICE RELAXATION TIME FOR EVA-CARBON NANOTUBES SYSTEMS

Samples	CNT (% w/w)	T_1H (MS)
EVA	0.00	60
EVA/NTC001	0.01	57
EVA/NTC010	0.10	56
EVA/NTC100	1.00	57

According to the relaxation data, the addition of small quantity of carbon nanotubes modified with acid does not influence sufficiently the molecular dynamic of the EVA matrix, the very low decreased in the relaxation value could be associated to some dispersion/distribution of the CNT in the EVA matrix.

These systems were also evaluated by the domain distribution curves (Figure 1). The distribution curves show some displacement for the systems that contains 0.1 % w/w of modified carbon nanotubes, which is in accordance with the relaxation data observed in the Table VI.

 ISBN: 978-1-61208-214-1

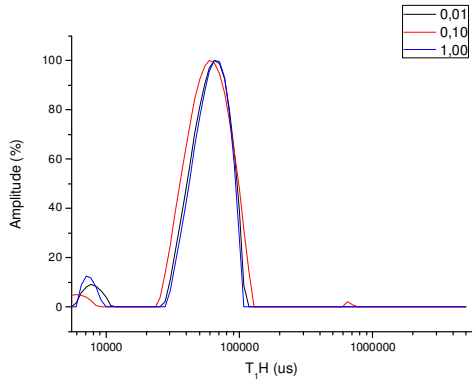

Figure 1. Domain distribution curves determined for the nanomaterials formed by EVA and modified carbon nanotubes.

IV. CONCLUSIONS

According to the relaxation data presented for the systems that using biopolymer and distinct nanoparticles we can see that independently of nanoparticles form their dispersion and distribution in the polymer matrix, as well as the intermolecular interaction can be accompanied by the proton spin-lattice relaxation time values.

For the EVA systems the nanostructured materials formed present a good nanoparticle dispersion and distribution, as a consequence of the preparation mode and the polymer matrix nanoparticle pair.

The evaluation of polymer nanomaterials was clearly obtained according to the changes in the relaxation time values comparing to the polymer matrix before the nanoparticles being incorporated to them. The NMR data showed to be a good alternative technique to be used to evaluate these type of materials.

ACKNOWLEDGMENT

The author would like to thank you the CAPES, CNPQ and FAPERJ for the financial support of this work and for the student's scholarships.

REFERENCES

[1] F A. Bovey, NMR Applied to Polymer Bulk, 1st Ed, vol 1, Oxford 1986, pp 1-6

[2] M. I. B. Tavares, R. F. Nogueira, R. A. S. San Gil, M. Preto, E. O. Silva, M. B. R. Silva, E. Miguez, Polypropylene-Clay Nanocomposite Structure probed by HNMR Relaxometry, Polym. Test, vol. 26, pp.1100 - 1102, may 2007

[3] D. L.Vanderhart, A. Asano, J. W Gilman, Hybrid materials: synthesis, characterization, and applications" Chemistry of Materials, vol 13, pp 3796- 3818, october 2001.

[4] C. Zeng, N. Hossieny, C. Zhang, B. Wang, Effects of charge density on the recognition properties of molecularly imprinted polyampholyte hydrogels, Polymer, vol 51, pp 655- 670, february 2010.

[5] S. Kuster, E. Danieli, B. Blumich, F. Casanova, High-resolution NMR spectroscopy under the fume hood, Physical Chemistry Chemical Physics, vol. 477, pp 231- , 2009.

[6] R. F. Nogueira, M. I. B. Tavares, R. A. S. San Gil, N. M. S. Ruiz, Solid state NMR investigation of polypropylene/ brazilian clay blending process, Polymer Testing, vol 24, pp 358 - 362, may 2005

[7] M. I. B. Tavares, NMR molecular dynamic study of high crystalline polymers, Polymer Testing, vol 19, pp 899- 904, september 2000

[8] T. Rodrigues, M. I. B. Tavares, M. Preto, I. L. Soares, L. A. Moreira, T. Rodrigues, Evaluation of Polyethylene/ Organoclay Nanocomposites by Low-field Nuclear Relaxation, Int. J. of Polymeric. Materials. vol. 57, pp 1119-1123, december 2008

[9] A. A. Passos, M. I. B. Tavares, R. P. Cucinelli Neto, L. A. Moreira, A. G. Ferreira, Obtenção de Nanocompósito de EVA/SÍLICA e Caracterização por Ressonância Magnética Nuclear no Estado Sólido, Polímeros: Ciência e Tecnologia, vol 21, pp 1- 5 , maio 2011

[10] P. P. Merat, M. I. B. Tavares, E. O. Silva, Preparation of Polycarbonate/clay Nanocomposite and Characterization by X-Ray, Thermal Analyzes and Low-field Nuclear Magnetic Resonance , Journal of Materials Science and Engineering vol A 1, pp 671- 679, november 2011

.A.S. Almeida, M.I.B. Tavares, E. O. Silva, R. P. Cucinelli Neto, L. A. Moreira, Development of Hybrid Nanocomposites based on PLLA and Low-Fiedl NMR Characterization, Polymer Testing, vol. 31, pp. 267- 275, april 2012

 ISBN: 978-1-61208-214-1

Tunable Plasmonic Nanogap Resonators

Tiziana C. Bond, Mihail Bora, Allan S.-P. Chang,
Center of Micron and Nano Technology
Lawrence Livermore National Laboratory
Livermore, USA
e-mail: bond7@llnl.gov, bora1@llnl.gov, chang@llnl.gov

***Abstract*—We present a new class of plasmonic substrates based on two-dimensional rectangular array of nanopillars over very large areas (4" wafers). The gap between each pair of neighboring nanopillars is small enough (< 100 nm) that highly confined plasmonic cavity resonances are supported in between such pairs. The resonant structures are tunable in the 400-800nm visible range with strong field enhancements and antireflective performance, up to 80% of incident light due to a highly efficient coupling and trapping. Because of their design and fabrication flexibility, these nanotemplates they can impact various fields, from detection and spectroscopy to energy harvesting to photovoltaic.**

Keywords- plasmonics; resonant cavity; tunability; nanolithography.

I. INTRODUCTION

Plasmonic nanostructures are widely investigated due to their strong controllability potential which suite their exploitation in disparate fields from bio-molecular detection [1-3] to sub-wavelength optics [4-6] and photovoltaic technology [7-9]. A plethora of 2D particle geometries have been employed but typically offer enhancements over narrow wavelength and incident angle ranges [10, 11]. There are currently new efforts in overcoming this inherent limitation of plasmonic nanostructures exploring also the third dimension [12-15]. Here, we propose a controllable broadband, tunable platform in which vertical plasmon resonant nanocavities are arranged in uniform and dense arrays of coupled metallic nanowires [16]. Tuning and broadening of the plasmonic multiple resonances is obtained by controlling the geometrical dimensions of the cavity, i.e interpillar gaps and heights, or the optical properties of the environment, i.e., the dielectric constant. In particular, the vertical dimension dictates the total number of supported wavelength resonances, whereas the horizontal dimension is responsible for the quality factor Q of the cavities. Using such knobs, UV to IR spectrum could be covered at once with less or more resonant plasmonic features favoring the conditions for either specific wavelength alignment with high Q as needed in spectroscopy or widely absorbing plasmons more critical in energy harvesting applications. Furthermore, because of the square lattice arrangement of the pillars, the platform is also polarization independent which can be advantageous as it reduces requirements of the available sources (i.e., Light Emitting Diodes or LEDs). In the following we will discuss about the technology providing high density tunable plasmonic paired nanopillars with excellent control of the cavity size over 4" wafers. Tuning of the plasmon resonance in the 400-800 nm range is demonstrated by controlling the geometrical dimensions of the cavity and the dielectric environment. The reflectivity and absorbance of the arrays of cavities for gold, silver and aluminum metals are presented. The limitations for the implementation of such a structure are discussed nevertheless showing that the averaged absorbance can be increased above 80%, a remarkable feature considering that these metals are used to fabricate highly reflective optical mirrors.

The paper is structured as follows: we will provide first a description of the experimental work, including the fabrication details, the principle of operation, the characterization setup , along with data derivation and model validation. Discussion of the results will follow. Finally, the conclusion and future outlook are presented.

II. EXPERIMENTS

A. Fabrication of Nanopillr Templates

The plasmonic substrate is composed of a rectangular array of vertical nanopillars coated with either gold, silver or he fabrication steps are reported in Fig. 1

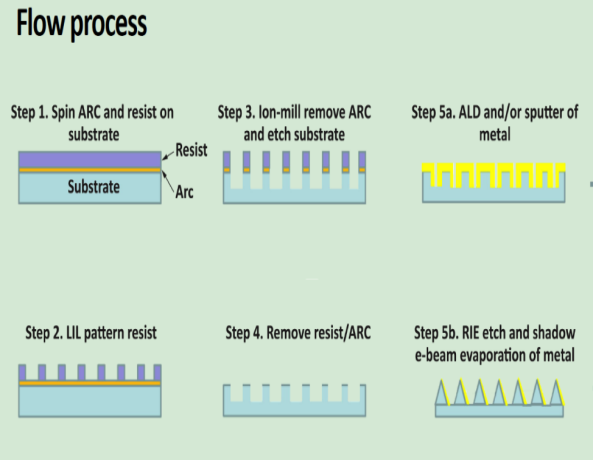

Figure 1. Fabrication steps details.

The period of the array is 360 nm, chosen such that insignificant diffraction grating effects take place in the visible spectrum. The nanopillar array template is patterned

 ISBN: 978-1-61208-214-1

using laser interference lithography [17] over 4" wafers that are coated with half-micron thick photoresist. The laser wavelength for the holography is 413 nm and the dose ~ 40 mJ/cm^2. The resultant photoresist structure is a periodic array of pillars with pitch of 360 nm and diameter ranging between 130 - 150 nm due to source dose variation. The patterned photoresist acts as the etching mask in a subsequent step of ion beam milling which enables the transfer of the geometry into a silicon or fused silica substrate. Further, the structure is either sputtered with conformal metallic films or coated first with a thick layer of Al_2O_3 by Atomic Layer Deposition (ALD) followed by a subsequent step of conformal sputtering of thinner metal layers. In this context we will discuss only the results obtained with the former as it gives more flexibility in controlling the aspect ratio of height vs. gap (or diameter of the pillars) due to the different vertical vs. sidewall deposition rates, eventually resulting more amenable to achieve the desired tunability. In fact, the height and diameter of the pillars are determined by the etch time and sputtering time respectively as shown in Figs. 2a and 2b. Incidentally, the combined ALD/sputtering process becomes more appealing for applications that require much smaller gaps (< 10 nm) such as Surface Enhanced Raman Spectroscopy, as it helps in refining the dimensions at the atomic level [18]. Pairs of vertically aligned nanopillars form a metal-dielectric-metal (MDM) waveguide when the edge to edge separation is closer than 100 nm (Fig. 2c). Plasmon modes are excited by normal incident light waves in the transverse magnetic (TM) polarization mode as exemplary polarization; for the transverse electric (TE) results would be just the same given the lattice symmetry.

B. Plasmonic Resonance Cavity Model

The resonant modes of the cavity are formed by the interference of forward and backward propagating waves and are determined by the dispersion relation of the waveguide and the phase shifts at each end

$$2k_{sp}h + \varphi_1 + \varphi_2 = 2m\pi, \quad (1)$$

where k_{sp} is the wavevector of the surface plasmon wave, h is the length of the cavity, φ_1 and φ_2, are the phase changes at the top and bottom boundaries and m is the resonance order. The dispersion relation, $k_{sp}(\omega)$ can be approximated with that of a semi-infinite planar MDM waveguide or calculated nuemrically. Fig. 2d shows the electric field amplitude profile for a resonant mode of order m = 4, as seen from three orthogonal cross sections. The node and anti-node conditions at each end are assumed to correspond to phase shifts of *0* (matched dielectric) and *π/2* (metal interface). In Fig. 2e we highlight the tangential power flow for the m = 4 mode. A net power flow occurs in the horizontal directions only at the rounded tapered region corresponding to a lateral flow convergent into the inter-wire waveguide. The curved ending acts as a sub-wavelength electromagnetic antenna that effectively increases the absorbance cross section of the cavity.

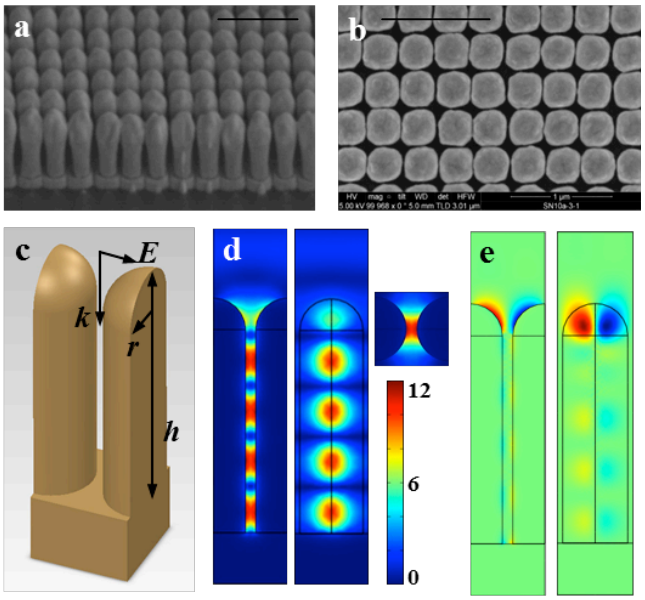

Figure 2. Fabrication: SEMs of the vertical metallic nanopillars viewed from side (a) and top (b); bar = 1 μm. Simulation: (c) Unit cell of the rectangular array centered on the plasmon nanocavity. (d) Electric field amplitude in the resonator seen from front, side and top when excited by noramlly incident TM mode. (e) Power flow in the vertical symmetry planes of the cavity channeled into the inter-pillar region from the top of the cavity.

C. Characterization and Model Validation

The frequency response of the resonator shows strong absorbance peaks that correspond to excitation of high electric field amplitude modes. The overall absorbance can be increased by adjusting the length of the resonator such that additional higher order modes are excited. Fig. 3 represents the simulated and experimentally measured reflectance of an array with 360 nm pitch made of silver nanopillars of 310 nm diameter and 1000 nm height. The electric field amplitude profile of the mode on the vertical symmetry axis of the unit cell is plotted as a function of wavelength. The plasmon cavity shows the strongest field enhancements for the modes that extend further into the free space and have a better overlap with the incident photon field. However, weak plasmon modes at other wavelengths, suggesting that stronger absorbance of the array over the whole spectrum can be achieved by engineering the ends. The directionality of the antenna is shown in Fig. 3c.

Array reflectivities were calculated for nanopillar arrays of variable height made of gold, silver and aluminum which arranged in the increasing order of their bulk plasma frequency [19]. The gold is significant for bio-molecular sensing, while silver and aluminum are relevant for photovoltaic applications since resonances have a better overlap with the solar spectrum.

In Fig. 4 we show the simulated reflectance spectrum of 360 nm pitch array of vertical nanowires of diameter 310

 ISBN: 978-1-61208-214-1

nm, variable height *h*, and capped by a hemisphere of diameter 310 nm. In the case of gold only a fraction of the visible spectrum is covered by plasmon resonances as the cut off frequency corresponds to an excitation wavelength of 550 nm, while for silver and aluminum the entire visible spectrum is covered. As the height of the pillar is increased the spacing between consecutive modes is decreasing enabling the cavity to have a strong absorbance at more excitation wavelengths. The simulations for the aluminum structures suggest that past a certain height, an increase in the length of the resonator causes a decrease in the absorbance strength. This can be explained by the higher losses of aluminum combined with longer paths of the plasmon at the interfaces. Alternatively, the effective length of the resonator can be changed by increasing the refractive index of the dielectric core as shown in Fig. 4g.

The effectiveness of the resonant array as a broadband absorber was assessed by calculating the average absorbance of the array in the 400-800 nm spectral range as a function of nanopillar height (Fig. 5). A stepwise decrease in absorbance is observed each time an additional resonance is added to the reflectance spectrum of the array.

The averaged absorbance becomes larger than the values calculated in Fig. 5 when restricted to a frequency range above common semiconductor bandgaps and when weighted by the photon energy and the solar irradiance spectrum. If the refractive index of the inter-pillar dielectric core is increased, the cutoff plasma frequency and the plasmon resonance locations are red shifted and the spacing between resonances becomes smaller as the optical length of resonator is increased. Based on these arguments, aluminum nanopillar dielectric hybrid structures have a better spectral coverage than any other metal considered. Silver on the other hand has the lowest losses in the visible and it is most efficient for transferring energy from the plasmon modes into

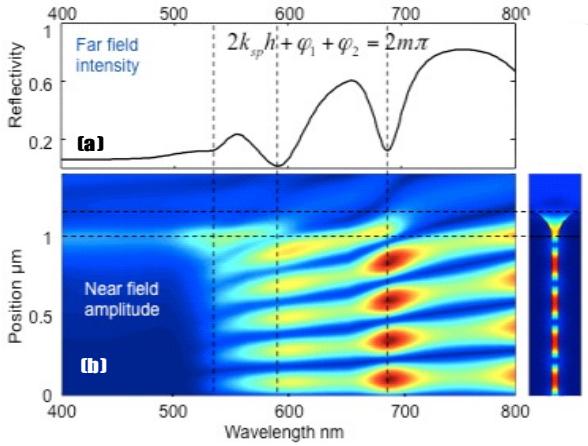

Figure 3. (a) Normal incidence reflectance (simulation and experiment) for a gold nanocavity 1000 nm long, 60 nm wide, showing full resonances of order 4, and 5. (b) Electric field amplitude of the plasmon mode in the center of the cavity plotted as a function of position and excitation wavelength. (c) Radar mapping showing directionality of the nanopillar antennae.

the absorptive dielectric material. The gold nanowire arrays have a significant potential for biological sensing.

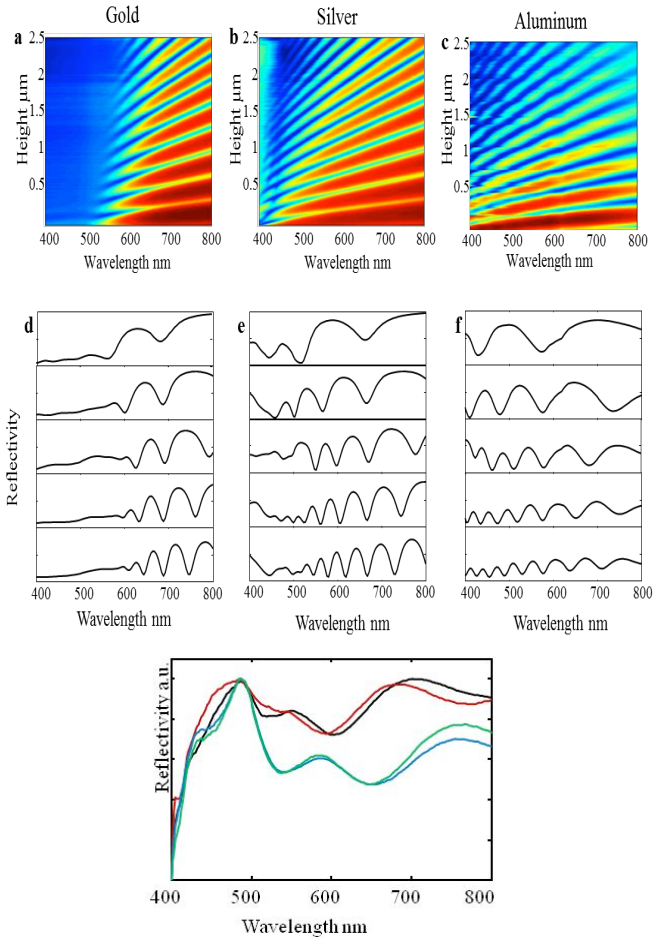

Figure 4. Simulations of the normal incidence reflected power for gold (a), silver (b) and aluminum (c) as a function of wavelength and pillar height. Multiple resonances can be excited bellow the plasmon cutoff frequency. Experimental plots of reflectivity for flat metallic films and arrays of height equal to 0.5, 1, 1.5, and 2 µm for gold (d), silver (e) and aluminum (f). (g) red-shift effect of dielectric. In all plots the reflectivity scale is 0 to 1.

III. CONCLUSIONS AND FUTURE WORK

We demonstrated multiresonant plasmonic nanocavities in vertical metallic nanopillar arrays with strong overlap and coupling between incident light and the plasmon modes. The absorbance of nanostructured metallic surfaces has been engineered to cover multiple wavelengths by increasing the longitudinal dimensions of the plasmon resonant nano-cavities. For large cavity sizes for aluminum and longer for silver and gold, the benefit of multiple resonances is offset by the weaker coupling into plasmons as the round trip

 ISBN: 978-1-61208-214-1

losses in the cavity become significant enough to decrease the electric field amplitude of the modes. Using geometry dependent tuning, the resonances can be further optimized for renewable energy applications for a better overlap with the absorbance of semiconductor materials. Most of the incident light is reflected in the red side of the spectrum, as the resonance spacing is increased at longer wavelengths.

Finally, in terms of application, it needs to be mentioned that the nano-cavities are envisioned for high sensitivity Raman spectroscopy that requires high local electromagnetic fields and alignment between the plasmon resonance and excited and scattered light [18]. Currently, besides Surface Enhanced Raman Spectroscopy which relies on visible resonant structures, we are also extending the cavity resonances to IR as source and detector platforms for enhanced IR spectroscopy. Furthermore, the tunable nanocavity are of particular relevance for fabrication of plasmonic lasers which use surface plasmons instead of light to pump the lasing medium [20], which we are also currently embarking on. Since the device structure relies on vertical free standing nano-pillars the plasmonic cavity region can be filled with any material of choice. Therefore, in addition to the high confinement factors shown, the cavity plasmon resonance can be adjusted for maximum overlap with the absorbance of the active material.

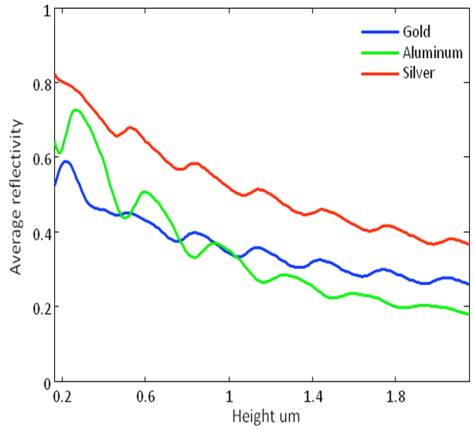

Figure 5. Average absorbance calculated over 400-800nm range.

ACKNOWLEDGMENTS

The authors thank Cindy Larson and Jerry Britten for helping on patterning the samples, Nick Teslich and Ed Sedillio on performing the SEM and/or FIB.. This work was performed under the auspices of the U.S. Department of Energy by Lawrence Livermore National Laboratory under Contract DE-AC52-07NA27344. LLNL- JRNL- 560591.

REFERENCES

[1] Hirsch, L. R., Jackson, J. B., Lee, A., Halas, N. J., and West, J. , Analytical Chemistry , vol. 75, Jan. 2003, , pp. 2377-2381.

[2] Rich, R. L. and Myszka, D. G., Current Opinion in Biotechnology , vol. 11, Oct. 2000 , pp. 54-61.

[3] Bora, M., Celebi, K., Zuniga, J., Watson, C., Milaninia, K. M., and Baldo, M. A., Optics Express, vol. 17, Jul. 2009, pp. 329-336.

[4] Barnes, W. L., Dereux, A., and Ebbesen, T. W., Nature, vol. 424, Jun. 2003 ,pp. 824-830.

[5] Ghaemi, H. F., Thio, T., Grupp, D. E., Ebbesen, T. W. and Lezec, H. J., Physical Review B, vol. 58, Nov. 1998, pp. 6779-6782.

[6] Lezec, H. J., Degiron, A., Devaux, E., Linke, R. A., Martin-Moreno, L., and Garcia-Vidal, F. J.; Ebbesen, T. W., Science, vol. 297, May 2002, pp. 820-823.

[7] Morfa, A. J., Rowlen, K. L., Reilly, T. H., Romero, M. J., and van de Lagemaat, Applied Physics Letters, vol. 92, Aug. 2008, pp. 013504-1-3.

[8] Tvingstedt, K., Persson, N. K., Inganas, O., Rahachou, A.;, and Zozoulenko, I. V., Applied Physics Letters, vol. 91, Mar. 2007, pp. 123514-1-3.

[9] Westphalen, M., Kreibig, U., Rostalski, J., Luth, H., and Meissner, D., Solar Energy Materials and Solar Cells, vol. 61, Jan. 2000, pp. 97-105.

[10] Anker, J. N., et al., Nature Materials, vol. 7, Jul.. 2008, pp. 442-453.

[11] Halas, N.J., Nanoletters, vol. 10, Oct. 2010, pp. 3816-3822.

[12] Zhou, W. and Odom, T., Nature Nanotechnolgy, vol. 6, Jun. 2011, pp. 423-427.

[13] Zhang Z., Weber-Bargioni, A., Wu, S. W., Dhuey, S., Cabrini, S., and Schuck, P.J., Nano Letters, vol. 9, Sept. 2009, pp. 4505-4509.

[14] Zhang J..Z., Optical properties and spectroscopy of nanomaterials, World Scientific Publishers, 2009.

[15] Kubo, N. and Fujikawa S., Nanoletters 2011, 11, pp. 8-15.

[16] Bora, M., et al., Nanoletters, vol. 10, Oct. 2010, pp. 2832-2837.

[17] Fernandez, A., et al., Journal of Vacuum Science Technology B, vol. 15, Apr. 1997, pp. 729-735.

[18] Chang, A. S.-P., et al., unpublished.

[19] Blaber, M.G, Arnold, M.D, and Ford, M. J., Journ Physical Cheminstry C, vol. 113, Dec. 2009, 3041-3046.

[20] Bora, M., et al., unpublished.

 ISBN: 978-1-61208-214-1

Security of Entanglement Swapping QKD Protocols against Collective Attacks

Stefan Schauer, Martin Suda
Department Safety and Security
AIT Austrian Institute of Technology GmbH
Vienna, Austria
stefan.schauer@ait.ac.at, martin.suda.fl@ait.ac.at

***Abstract*—We discuss the security of quantum key distribution protocols based on entanglement swapping against collective attacks. Therefore, we apply a generic version of a collective attack strategy on the most general entanglement swapping scenario used for key distribution. Further, we focus on basis transformations, which are the most common operations performed by the legitimate parties to secure the communication. In this context, we show that the angles, which describe these basis transformations can be optimized compared to an application of the Hadamard operation. As a main result, we show that the adversary's information is reduced to a new minimum of about 0.45, which is about 10% lower than in other protocols.**

Keywords-quantum key distribution; entanglement swapping; security analysis; optimal basis transformations.

I. INTRODUCTION

Quantum key distribution (QKD) is an important application of quantum mechanics and QKD protocols have been studied at length in theory and in practical implementations [1], [2], [3], [4], [5], [6], [7], [8]. Most of these protocols focus on prepare and measure schemes where single qubits are in transit between the communication parties Alice and Bob. The security of these prototcols has been discussed in depth an security proofs have been given for example in [9], [10], [11]. In addition to these prepare and measure protocols, several protocols based on the phenomenon of entanglement swapping have been introduced [12], [13], [14], [15], [16]. In these protocols, entanglement swapping is used to obtain correlated measurement results between the legitimate communication parties, Alice and Bob. In other words, each party performs a Bell state measurement and due to entanglement swapping their results are correlated and further on used to establish a secret key.

Entanglement swapping has been introduced by Bennett et al. [17], Zukowski et al. [18] as well as Yurke and Stolen [19], respectively. It provides the unique possibility to generate entanglement from particles that never interacted in the past. In detail, Alice and Bob share two Bell states of the form $|\Phi^+\rangle_{12}$ and $|\Phi^+\rangle_{34}$ such that afterwards Alice is in possession of qubits 1 and 3 and Bob of qubits 2 and 4 (cf. Figure 1). Then Alice performs a complete Bell state measurement on the two qubits in her possession, which results in

$$|\Phi^+\rangle_{12} \otimes |\Phi^+\rangle_{34} = \frac{1}{2}\Big(|\Phi^+\rangle|\Phi^+\rangle + |\Phi^-\rangle|\Phi^-\rangle + |\Psi^+\rangle|\Psi^+\rangle + |\Psi^-\rangle|\Psi^-\rangle\Big)_{1324} \quad (1)$$

After the measurement, the qubits 2 and 4 at Bob's side collapse into a Bell state although they originated at completely different sources. Moreover, the state of Bob's qubits depends on Alice's measurement result. As presented in eq. (1) Bob always obtains the same result as Alice when performing a Bell state measurement on his qubits.

The security of QKD protocols based on entanglement swapping has been discussed on the surface so far. It has only been shown that these protocols are secure against intercept-resend attacks and basic collective attacks (cf. for example [12], [13], [15]). Therefore, we analyze a general version of a collective attack where the adversary tries to simulate the correlations between Alice and Bob [20]. A basic technique to secure these protocols is to use a basis transformation, usually a Hadamard operation, similar to the prepare and measure schemes mentioned above, to make it easier to detect an adversary. Hence, we analyze the security with respect to a general basis transformation about an angle θ_A applied by Alice and a transformation about an angle θ_B applied by Bob. In the course of that, we are going to identify, which values for θ_A and θ_B are optimal such that an adversary has only a minimum amount of information on the secret key.

In the next section, we are going to shortly review the simulation attack, a generic collective attack strategy where an adversary applies a six-qubit state to eavesdrop Bob's measurement result. A detailed discussion of this attack strategy can be found in [20]. In Section III, we discuss the security of entanglement swapping based QKD protocols agains the simulation attack. Here, we are focussing on the application of one and two basis transformations and define the optimal angles for these transformations. At the end, we summarize the results and give a short outlook on our next steps into this topic.

II. THE SIMULATION ATTACK STRATEGY

In entanglement swapping based QKD protocols like [12], [13], [14], [15], [16] Alice and Bob rest their security check

 ISBN: 978-1-61208-214-1

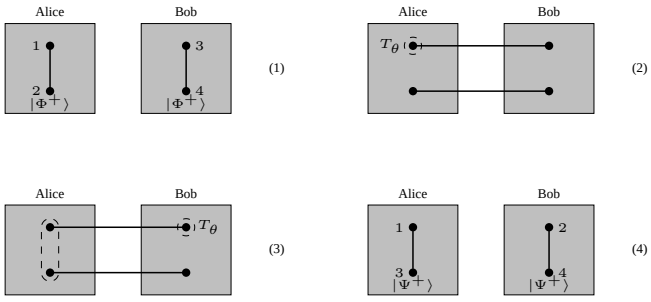

Figure 1. Illustration of a standard setup for an entanglement swapping based QKD protocol using a basis transformation T_x.

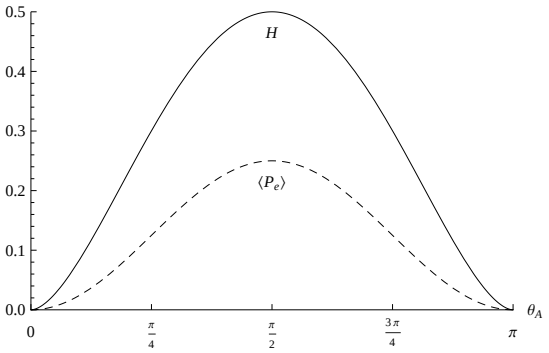

Figure 2. Alice's and Bob's Shannon entropy H and the according average error probability $\langle P_e \rangle$ if either Alice or Bob applies a basis transformation.

onto the correlations between their respective measurement results coming from the entanglement swapping (cf. eq. (1)). If these correlations are violated, Alice and Bob have to assume that an eavesdropper is present. Hence, a general version of a collective attack has the following basic idea: the adversary Eve tries to find a multi-qubit state, which preserves the correlation between the two legitimate parties. Further, she introduces additional qubits to distinguish between Alice's and Bob's respective measurement results. If she is able to find such a state Eve stays undetected during her intervention and is able to obtain a certain amount of information about the key. In a previous article [20], we already described such a collective attack called *simulation attack* for a specific protocol [16]. The generalization is straight forward as described in the following paragraphs. It has been pointed out in detail in [20] that Eve uses 4 qubits to simulate the correlations between Alice and Bob and she introduces additional systems, i.e., $|\varphi_i\rangle$, to distinguish between Alice's different measurement results. This leads to the state

$$|\delta\rangle = \frac{1}{2}\Big(|\Phi^+\rangle|\Phi^+\rangle|\varphi_1\rangle + |\Phi^-\rangle|\Phi^-\rangle|\varphi_2\rangle \\ |\Psi^+\rangle|\Psi^+\rangle|\varphi_3\rangle + |\Psi^-\rangle|\Psi^-\rangle|\varphi_4\rangle\Big)_{PRQSTU} \quad (2)$$

which is a more general version than described in [20]. This state preserves the correlation of Alice's and Bob's measurement results coming from the entanglement swapping (cf. eq. (1)). To be able to eavesdrop Alice's and Bob's measurement results Eve has to choose the auxiliary systems $|\varphi_i\rangle$ such that

$$\langle\varphi_i|\varphi_j\rangle = 0 \qquad i,j \in \{1,...,4\} \;\; i \neq j \quad (3)$$

This allows her to perfectly distinguish between Alice's and Bob's respective measurement results and thus gives her full information about the classical raw key generated out of them.

In detail, Eve distributes qubits P, Q, R and S between Alice and Bob such that Alice is in possession of qubits P and R and Bob is in possession of qubits Q and S. When Alice performs a Bell state measurement on qubits P and R the state of qubits Q and S collapses into the same Bell state, which Alice obtained from her measurement (compare eq. (1) and eq. (2)). Hence, Eve stays undetected when Alice and Bob compare some of their results in public to check for eavesdroppers. The auxiliary system $|\varphi_i\rangle$ remains at Eve's side and its state is completely determined by Alice's measurement result. Therefore, Eve has full information on Alice's and Bob's measurement results and is able to perfectly eavesdrop the classical raw key.

There are different ways for Eve to distribute the state $|\delta\rangle_{P-U}$ between Alice and Bob. One possibility is that Eve is in possession of Alice's and Bob's source and generates $|\delta\rangle_{P-U}$ instead of Bell states. This is a rather strong assumption because the sources are usually located at Alice's or Bob's laboratory, which should be a secure place. Nevertheless, Eve's second possibility is to intercept the qubits 2 and 3 flying from Alice to Bob and vice versa and to perform entanglement swapping to distribute the state $|\delta\rangle$. This is a straight forward method as already described in [20].

We want to stress that the state $|\delta\rangle$ is generic for all protocols where 2 qubits are exchanged between Alice and Bob during one round of key generation as, for example, the QKD protocols presented by Song [15], Li et al. [16] or Cabello [12]. As already pointed out in [20], the state $|\delta\rangle$ can also be used for different initial Bell states. For protocols with a higher number of qubits the state $|\delta\rangle$ has to be extended accordingly.

III. Security Against Collective Attacks

In the following paragraphs we discuss Eve's intervention on an entanglement swapping QKD protocol performing a simulation attack, i.e., using the state $|\delta\rangle_{P-U}$. To detect Eve's presence either Alice or Bob or both parties apply a basis transformations as depicted in Figure 1.

A. General Basis Transformations

Similar to the prepare and measure schemes mentioned in the introduction most of the protocols based on entanglement swapping apply basis transformations to make it easier to

detect the presence of an eavesdropper. The basis transformation most commonly used in this case is the Hadamard operation, i.e., a transformation from the Z- into the X-basis. In general, a basis transformation from the Z-Basis into the X-basis can be described as a combination of rotation operations, i.e.,

$$T(\theta,\phi) = e^{i\phi} R_z(\phi) R_x(\theta) R_z(\phi) \tag{4}$$

where R_x and R_z are the rotation operations about the X- and Z-axis, respectively. For reasons of simplicity we take $\phi = \pi/2$ in our further discussions and therefore denote the transformation is described solely by the angle θ, i.e., T_θ. From eq. (4) we can directly see that the Hadamard operation equals T_θ for $\theta = \pi/2$. To keep the security analysis as generic as possible we discuss a setup where a general basis transformation about an angle θ_A is applied by Alice and a transformation about an angle θ_B is applied by Bob (cf. Figure 1).

For our further discussions we will assume that Alice and Bob prepared the initial states $|\Phi^+\rangle_{12}$ and $|\Phi^+\rangle_{34}$ as described above to make calculations easier. As already described in [20] if Alice and Bob choose $\theta_A = \theta_B = 0$, i.e., they perform no transformation, the protocol is completely insecure. Hence, we will focus on the scenarios where either T_{θ_A} or T_{θ_B} or both transformations are applied. For all scenarios we assume that Alice applies T_{θ_A} on qubit 1 and Bob applies T_{θ_B} on qubit 4.

B. Application of a Single Transformation

For the first scenario where only Alice applies the basis transformation the overall state of the system after Eve's distribution of the state $|\delta\rangle_{P-U}$ can simply be described as

$$|\delta'\rangle = T^{(1)}_{\theta_A} |\delta\rangle_{1QR4TU} \tag{5}$$

where the superscript "(1)" indicates that T_{θ_A} is applied on qubit 1. When Eve sends qubits R and Q to Alice and Bob, respectively, the state after Alice's Bell state measurement on qubits 1 and R is

$$\cos\frac{\theta_A}{2}\,|\Phi^-\rangle_{Q4}|\varphi_2\rangle_{TU} + \sin\frac{\theta_A}{2}\,|\Psi^+\rangle_{Q4}|\varphi_3\rangle_{TU} \tag{6}$$

assuming Alice obtained $|\Phi^+\rangle_{1R}$ (for Alice's other three possible results the state changes accordingly). This leads to the assumption that in this case Bob's transformation back into the Z-basis does not re-establish the correlations between Alice and Bob properly. Performing the calculations we see that Bob's operation T_{θ_A} brings qubits Q, 4, T and U into the form

$$\begin{aligned}&\cos^2\frac{\theta_A}{2}\,|\Phi^+\rangle_{Q4}|\varphi_2\rangle_{TU} + \sin^2\frac{\theta_A}{2}\,|\Phi^+\rangle_{Q4}|\varphi_3\rangle_{TU}\\ &-\frac{\sin\theta_A}{2}\,|\Psi^-\rangle_{Q4}|\varphi_2\rangle_{TU} + \frac{\sin\theta_A}{2}\,|\Psi^-\rangle_{Q4}|\varphi_3\rangle_{TU}\end{aligned} \tag{7}$$

When Bob performs a Bell state measurement we can directly see from this expression that Bob obtains either the correlated result $|\Phi^+\rangle_{Q4}$ with probability

$$\left(\cos^2\frac{\theta_A}{2}\right)^2 + \left(\sin^2\frac{\theta_A}{2}\right)^2 = \frac{3+\cos(2\theta_A)}{4} \tag{8}$$

or an error, i.e., the state $|\Psi^-\rangle_{Q4}$, otherwise. Hence, Eve introduces an error with probability $(\sin^2\theta_A)/2$, which yields an expected error probability

$$\langle P_e\rangle = \frac{\sin^2\theta_A}{4} \tag{9}$$

Nevertheless, as long as the results are correlated Eve obtains from her Bell state measurement on qubits T and U the state $|\varphi_2\rangle_{TU}$ with probability $(1+\cos(\theta_A))^2/(3+\cos(2\theta_A))$ and knows that Bob obtained $|\Phi^+\rangle_{Q4}$. Consequently, we obtain the expected collision probability

$$\langle P_c\rangle = \frac{1}{8}\Big(7+\cos(2\theta_A)\Big). \tag{10}$$

This directly leads to the Shannon entropy

$$H = \frac{1}{2}\,h\Big(\cos^2\frac{\theta_A}{2}\Big) \tag{11}$$

where $h(x) = -x\log_2 x - (1-x)\log_2(1-x)$ is the binary entropy. Looking at $\langle P_e\rangle$ and H in Figure 2 we see that the optimal angle for a single basis transformation is $\pi/2$, i.e., the Hadamard operation. If only Bob applies the basis transformation the claculations run analogous to this scenario and therefore provide the same results.

C. Application of Combined Transformations

When both Alice and Bob apply their basis transformation the overall state changes to

$$|\delta'\rangle = T^{(1)}_{\theta_A} T^{(4)}_{\theta_B} |\delta\rangle_{1QR4TU} \tag{12}$$

and after Alice's Bell state measurement on qubits 1 and R and Bob's application of T_{θ_B} on qubit Q the state of the remaining qubits is

$$\begin{aligned}&\cos^2\frac{\theta_A-\theta_B}{2}\,|\Phi^+\rangle_{Q4}|\varphi_1\rangle_{TU}\\ &+\sin^2\frac{\theta_A-\theta_B}{2}\,|\Phi^+\rangle_{Q4}|\varphi_4\rangle_{TU}\\ &-\frac{\sin(\theta_A-\theta_B)}{2}\,|\Psi^-\rangle_{Q4}\Big(|\varphi_1\rangle_{TU}-|\varphi_4\rangle_{TU}\Big)\end{aligned} \tag{13}$$

Consequently, Bob obtains a correlated result with probability $(3+\cos(2\theta_A-2\theta_B))/4$ and following the argumentation from scenario described in Section III-B above this yields an average error probability (cf. Figure 3 for a plot of this function)

$$\langle P_e\rangle = \frac{1}{16}\Big(3-\cos 2\theta_A - 2\cos^2\theta_A\cos 2\theta_B\Big) \tag{14}$$

When the results are correlated Eve obtains either $|\varphi_1\rangle_{TU}$ or $|\varphi_4\rangle_{TU}$, as it is easy to see from eq. (13). Hence, Eve's

 ISBN: 978-1-61208-214-1

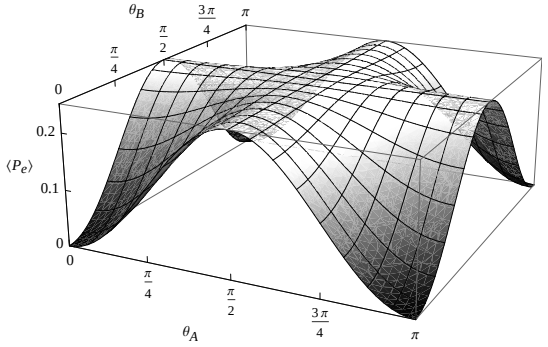

Figure 3. Eve's expected error probability $\langle P_e \rangle$ if both parties apply a basis transformation with the respective angles θ_A and θ_B.

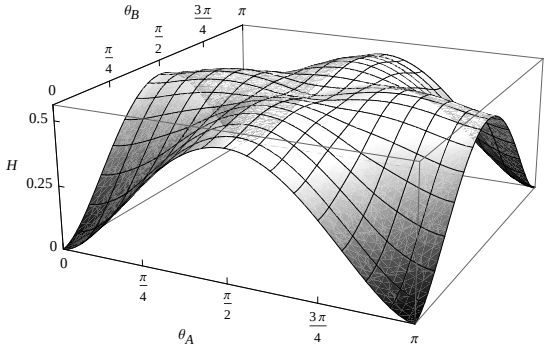

Figure 4. Alice's and Bob's Shannon entropy H if both parties apply a basis transformation with the respective angles θ_A and θ_B.

information on the Alice's and Bob's result is lower compared to the first scenario, i.e., Alice's and Bob's Shannon entropy is higher:

$$H = \frac{1}{4}\, h\Big(\cos^2\frac{\theta_A}{2}\Big) + \frac{1}{4}\, h\Big(\cos^2\frac{\theta_B}{2}\Big) + \frac{1}{8}\, h\Big(\cos^2\frac{\theta_A+\theta_B}{2}\Big) + \frac{1}{8}\, h\Big(\cos^2\frac{\theta_A-\theta_B}{2}\Big) \tag{15}$$

This is due to the fact that it is more difficult for Eve to react on two separate basis transformations with different angles θ_A and θ_B and is easy to see from the plot of the Shannon entropy H in Figure 4.

IV. Results

For the scenarios where either Alice or Bob applies a basis transformation at random, the optimal value for θ_A and θ_B, respectively, is $\pi/2$. Therefore, the Hadamard operation is the optimal choice in this scenario for protocols using only one basis transformation, as it is already known from literature [13], [20]. In this case the average error probability as well as the Shannon entropy are maximal at $\langle P_e \rangle = 0.25$ and $H = 0.5$ (cf. Figure 2). Further, Eve's information on the bits of the secret key is given by the mutual information

$$I_{AE} = 1 - H = 1 - \frac{1}{2} = \frac{1}{2} \tag{16}$$

which means that Eve has 0.5 bits of information on every bit of the secret key. Using error correction and privacy amplification Eve's information can be brought below 1 bit of the whole secret key as long as the error rate is below $\sim 11\%$ [11]. This is more or less the standard threshold value for the prepare and measure QKD protocols.

A combined application of the Hadamard operation by both parties would indicate at a first glance that the security is further increased. But when we look at Figure 4 we see that a random application of the Hadamard operation by both Alice and Bob gives the same result as the application on just one side. This is due to the fact that in case both parties apply the Hadamard operation at the same time the operations cancel out each other. But as we can further see from Figure 4, the Shannon entropy for a combined application of basis transformations is much higher for some regions. In detail, the maximum of the function plotted in Figure 4 is

$$H \sim 0.55 \quad \text{and thus} \quad I_{AE} \sim 0.45 \tag{17}$$

for $\theta_A = \pi/4$ and $\theta_B = \pi/2$ or vice versa. Hence, if just one of the parties applies a Hadadmard operation and the other one a transformation about an angle of $\pi/4$ Eve's mutual information is about 10% lower. At the same time we see from Figure 3 that for these two values of θ_A and θ_B the error probability is still maximal with $\langle P_e \rangle = 0.25$. This means Alice and Bob are able to further reduce Eve's information about the raw key by the combined application of two basis transformations, one about $\theta = \pi/2$ and the other about $\theta = \pi/4$.

V. Conclusion and Further Research

In this article, we discussed the optimality of basis transformations to secure entanglement swapping based QKD prototcols. Starting from a generic entanglement swapping scenario we used a collective attack strategy to analyse the amount of information an adversary is able to obtain. We showed that in case only one party applies a basis transformation the operation T_θ reduces to the Hadamard operation, i.e., the angle $\theta = \pi/2$ allows a maximal mutual information of $I_{AE} = 0.5$. Whereas, if both parties apply a transformation the optimal choice for the angles θ_A and θ_B describing the basis transformations is $\theta_A = \pi/4$ and $\theta_B = \pi/2$. This decreases the mutual information of an adversary further to $I_{AE} \sim 0.45$.

The next questions arising directly from these results are how, if at all, the results change if basis transformations from the Z- into the Y-basis are applied. A first inspection shows that such basis transformations can not be plugged in direclty into this framework. Besides the transformation from the Z- into the Y- basis we are going to insepct the effects of the simpler rotation operations on the results. Since basis transformations can be described in terms of rotation operations it could be easier to apply rotation

 ISBN: 978-1-61208-214-1

operations in this framework. Due to the similar nature of basis transformations and rotation operations we assume that the results will be the same as presented here.

To keep the setting as general as possible the main goal is to allow Alice and Bob to use arbitrary unitary operations instead of just basis transformations to secure the protocol. This should make it even more difficult for Eve to gain information about the raw key.

ACKNOWLEDGMENTS

We would like to thank Christian Kollmitzer, Oliver Maurhart as well as Beatrix Hiesmayr and Marcus Huber for fruitful discussions and interesting comments.

REFERENCES

[1] C. H. Bennett and G. Brassard, "Public Key Distribution and Coin Tossing," in *Proceedings of the IEEE International Conference on Computers, Systems, and Signal Processing*. IEEE Press, pp. 175–179, 1984.

[2] A. Ekert, "Quantum Cryptography Based on Bell's Theorem," *Phys. Rev. Lett.*, vol. 67, no. 6, pp. 661–663, 1991.

[3] C. H. Bennett, G. Brassard, and N. D. Mermin, "Quantum Cryptography without Bell's Theorem," *Phys. Rev. Lett.*, vol. 68, no. 5, pp. 557–559, 1992.

[4] D. Bruss, "Optimal Eavesdropping in Quantum Cryptography with Six States," *Phys. Rev. Lett*, vol. 81, no. 14, pp. 3018–3021, 1998.

[5] A. Muller, H. Zbinden, and N. Gisin, "Quantum Cryptography over 23 km in Installed Under-Lake Telecom Fibre," *Europhys. Lett.*, vol. 33, no. 5, pp. 335–339, 1996.

[6] A. Poppe, A. Fedrizzi, R. Usin, H. R. Böhm, T. Lorünser, O. Maurhardt, M. Peev, M. Suda, C. Kurtsiefer, H. Weinfurter, T. Jennewein, and A. Zeilinger, "Practical Quantum Key Distribution with Polarization Entangled Photons," *Optics Express*, vol. 12, no. 16, pp. 3865–3871, 2004.

[7] A. Poppe, M. Peev, and O. Maurhart, "Outline of the SECOQC Quantum-Key-Distribution Network in Vienna," *Int. J. of Quant. Inf.*, vol. 6, no. 2, pp. 209–218, 2008.

[8] M. Peev, C. Pacher, R. Alléaume, C. Barreiro, J. Bouda, W. Boxleitner, T. Debuisschert, E. Diamanti, M. Dianati, J. F. Dynes, S. Fasel, S. Fossier, M. Fürst, J.-D. Gautier, O. Gay, N. Gisin, P. Grangier, A. Happe, Y. Hasani, M. Hentschel, H. Hübel, G. Humer, T. Länger, M. Legré, R. Lieger, J. Lodewyck, T. Lorünser, N. Lütkenhaus, A. Marhold, T. Matyus, O. Maurhart, L. Monat, S. Nauerth, J.-B. Page, A. Poppe, E. Querasser, G. Ribordy, S. Robyr, L. Salvail, A. W. Sharpe, A. J. Shields, D. Stucki, M. Suda, C. Tamas, T. Themel, R. T. Thew, Y. Thoma, A. Treiber, P. Trinkler, R. Tualle-Brouri, F. Vannel, N. Walenta, H. Weier, H. Weinfurter, I. Wimberger, Z. L. Yuan, H. Zbinden, and A. Zeilinger, "The SECOQC Quantum Key Distribution Network in Vienna," *New Journal of Physics*, vol. 11, no. 7, p. 075001, 2009.

[9] N. Lütkenhaus, "Security Against Eavesdropping Attacks in Quantum Cryptography," *Phys. Rev. A*, vol. 54, no. 1, pp. 97–111, 1996.

[10] ——, "Security Against Individual Attacks for Realistic Quantum Key Distribution," *Phys. Rev. A*, vol. 61, no. 5, p. 052304, 2000.

[11] P. Shor and J. Preskill, "Simple Proof of Security of the BB84 Quantum Key Distribution Protocol," *Phys. Rev. Lett.*, vol. 85, no. 2, pp. 441–444, 2000.

[12] A. Cabello, "Quantum Key Distribution without Alternative Measurements," *Phys. Rev. A*, vol. 61, no. 5, p. 052312, 2000.

[13] ——, "Reply to "Comment on "Quantum Key Distribution without Alternative Measurements"","," *Phys. Rev. A*, vol. 63, no. 3, p. 036302, 2001.

[14] ——, "Multiparty Key Distribution and Secret Sharing Based on Entanglement Swapping," *quant-ph/0009025 v1*, 2000.

[15] D. Song, "Secure Key Distribution by Swapping Quantum Entanglement," *Phys. Rev. A*, vol. 69, no. 3, p. 034301, 2004.

[16] C. Li, Z. Wang, C.-F. Wu, H.-S. Song, and L. Zhou, "Certain Quantum Key Distribution achieved by using Bell States," *International Journal of Quantum Information*, vol. 4, no. 6, pp. 899–906, 2006.

[17] C. H. Bennett, G. Brassard, C. Crepeau, R. Jozsa, A. Peres, and W. K. Wootters, "Teleporting an Unknown Quantum State via Dual Classical and EPR Channels," *Phys. Rev. Lett.*, vol. 70, no. 13, pp. 1895–1899, 1993.

[18] M. Zukowski, A. Zeilinger, M. A. Horne, and A. K. Ekert, ""Event-Ready-Detectors" Bell State Measurement via Entanglement Swapping," *Phys. Rev. Lett.*, vol. 71, no. 26, pp. 4287–4290, 1993.

[19] B. Yurke and D. Stoler, "Einstein-Podolsky-Rosen Effects from Independent Particle Sources," *Phys. Rev. Lett.*, vol. 68, no. 9, pp. 1251–1254, 1992.

[20] S. Schauer and M. Suda, "A Novel Attack Strategy on Entanglement Swapping QKD Protocols," *Int. J. of Quant. Inf.*, vol. 6, no. 4, pp. 841–858, 2008.

 ISBN: 978-1-61208-214-1

Reservoir Rock Microstructure Evaluation by X-ray Microtomography

Alessandra de Castro Machado, Inaya Lima, Ricardo Tadeu Lopes
Nuclear Engineering Program, Nuclear Instrumentation Laboratory, Federal University of Rio de Janeiro. POBox.: 68509, Zip code: 21941-972, Rio de Janeiro, Brasil.
e-mail: alessandra_fisica@hotmail.com, inaya@lin.ufrj.br, ricardo@lin.ufrj.br

***Abstract*—The objective of this study is to evaluate the quantification process of geometric parameters such as material volume, when different computed microtomography spatial resolutions are employed. To this end, two reservoir rock samples were scanned with a three-dimensional high energy computed microtomography system. The results show a strong difference in the acquisition, reconstruction and image processing times, but do not present a significant loss of information on the micro structural parameters such as porosity between the two resolutions.**

Keywords-X-ray; microtomography; rock.

I. INTRODUCTION

High resolution 3D computed microtomography (microCT) is a powerful technique used to visualize and characterize the internal structure of objects. It is a non-destructive method that produces images of the internal structure of an object which does not need to be previously modified, i.e., the object inspected does no need to be subjected to a preparation method such as impregnation, thinning or polishing [1]. In this technique, contiguous sequential images are compiled to create 3D representations that may be digitally processed to obtain relevant quantitative geometric and/or morphologic parameters, depending on the focus of the investigation [2]. The great advantage of microtomography is that quantitative information such as volume, size, shape, distribution and connectivity of the rock pores can be obtained through the entire 3D volume of the samples, from micro-scale to nano-scale.

MicroCT physical principle is based on the attenuation of X-rays when they interact with the object. The intensity of the photons crossing the object depends on the number of atoms by volume unit (density) and on the type of the atoms throughout the beam. In order to obtain the image of a section of a test specimen it is necessary to obtain many projections in constant angular steps [3]. Beam hardening artifacts in gray level, which may show up in the images, manifest due to the preferential attenuation of low energy photons. This process can be minimized using metallic filters to eliminate low energy photons from the incident radiation. When the object is a rock sample it is common to insert a combination of two metallic filters such as aluminum and copper [4].

It is know that the better the spatial resolution of the images in microCT the better the visualization of small details. However, the quantification of structural parameters in microCT is extremely dependent on image resolution, which may affect final data interpretation [5-7].

The objective of this study is to evaluate the changes that occur in the entire quantification process (acquisition, reconstruction and processing) of geometric parameters, such as porosity, of reservoir rocks when different image resolutions are employed. For that purpose it will be used high resolution microCT equipment and several holes in two rocks will be the focal point of this investigation.

In the next sections it will be described all the experimental conditions that the carbonates were submitted, as well as the methodology used to characterize the rocks. The geometric parameters used in this study were the total volume of the binary-converted objects within the volume of interest, the percentage of the volume of interest occupied by binary, the total porous space volume and total porosity. After that section, for each experimental condition and imaging processing, the results are analyzed and discussed and the 3D microCT visualization will be presented together.

II. MATERIALS AND METHODS

The reservoir rocks used in this study are of the carbonated type and were named samples 1 and 2 (Fig. 1). Five holes were made in the sample 1 and nine holes in sample 2, in a way that their dimensions are known. Thus, it is possible to evaluate the accuracy and precision of 3D quantification by microCT.

MicroCT's were obtained in a high energy microtomography system (Skyscan/Bruker, model 1173). The samples were placed in the experimental equipment inside an acrylic cylinder with a 1.0mm thickness for sample 1 and a 3.1mm thickness for sample 2. This ensured that the samples would not move during the entire acquisition process, which lasted about 1 or 2 hours, depending on the resolution used.

The system was calibrated to operate at 130kV of energy and a current of 61 μA. The microCT system has 2 built-in metallic filter options: aluminum (with a thickness of

 ISBN: 978-1-61208-214-1

1.0mm) and brass (0.15mm thick). The intention of these filters is to reduce the contribution of low energy photons to minimize the effects of beam hardening. In the present study, a combination of two filters was used: copper (0.15mm thick) and aluminum (1.0mm thick).

The spatial resolutions used in this study were 10 µm and 20 µm. In these conditions the distances source- sample and source- detector were of 72.8mm and 291.2mm for the 10µm resolution and of 148.3mm and 215.7mm for the 20µm resolution, respectively. A flat panel detector was used (2240 x 2240 pixels) to register the cone X-ray beam transmission. The projection images were taken 360º at each step of 0.50º rotation.

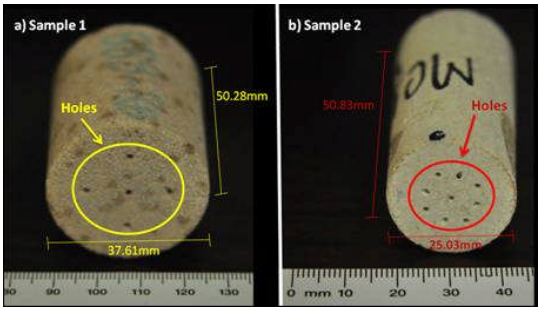

Figure 1. (a) photograph of sample 1 with their dimensions and the holes in the spotlight and (b) photograph of sample 2, also with their dimensions and the holes in the spotlight.

After the acquisition process, the radiographic images were rebuilt. For such, Nrecon ® [08] - version 1.6.4.1 and InstaRecon [09] - version 1.3.5.0 softwares were used, the algorithm of which is based on the works of Feldkamp [10]. The reconstruction software used allows the selection of many parameters thus creating a better quality image. Artifact corrections can be made in the image such as correction of the ring artifact that shows up as total or partial rotation-axis centered circles, caused by changes on the output of individual detectors or set of detectors. Corrections of beam hardening can also be made, which turns the object borders shinier than the center even in homogeneous materials since low energy X-rays are attenuated more promptly than high energy X-rays.

The most important parameters are the use of smoothing filters in different degrees (1 to 10), reduction of ring artifacts in different levels (1 to 20) and beam hardening correction in different levels (1% to 100%). In this study, Gaussian smoothing filters with degree 1, a ring artifact reduction with level 15 for sample 1 and level 10 for sample 2 and a beam hardening artifact correction with a degree of 20% for sample 1 and of 25% for sample 2 were used. The Kernel Gaussian smoothing filter is characterized as a smoothing applied to projections. It smoothes each pixel with a MxN neighborhood, where M is the horizontal dimension and N the vertical dimension. It reduces noise and searches for a proper smoothing level. Ring artifact reduction is also applied to projection before image pre-processing so that the average projection is used for this purpose. It is possible to select the depth of this correction in a 1 to 20 pixel gap. Beam hardening can be obtained through linear transformation and depth correction can be chosen according to the material density. A high order in the polynomial function can also be used for this purpose.

The Skyscan, CTAn ® [11] (v.1.11.8.0) software was used for image processing and analysis. In this stage the objective was to quantify geometric parameters related to the holes created in each of the samples at the laboratory. These holes were made with a 0.9 mm wide drill in sample 1 and a 1.0 mm wide drill in sample 2. Thus, the final dimension of the holes drilled were of 9.3 mm, 3.7 mm, 3.4 mm, 3.0 mm and 4.1 mm depth for sample 1 and of 9.0 mm, 4.9 mm, 3.5 mm, 4.5 mm, 4.0 mm, 4.4 mm, 4.1 mm, 4.35 mm and 4.3 mm depth for sample 2. Considering a cylindrical geometry and disregarding the narrowing obtained at the end of each hole it is possible to say that the volume of the holes were 14.92 ±0.02 mm^3 in sample 1 and 33.75±0.02 mm^3 in sample 2. The quantified parameters were: total volume of the binary-converted objects within the volume of interest, VOI, (BV, mm^3), percentage of VOI occupied by binary objects (BV/TV, %), total porous space volume (Po. V(tot), mm^3) and total porosity percentage (Po.(tot), %).

A region of interest (ROI) that contemplates both holes in each sample and in each resolution was defined to conduct the quantifications. All objects inside the ROI were analyzed. In this study, circular ROIs with a diameter equal to 23.16mm and 14.48mm for samples 1 and 2, respectively, were used.

It is important to highlight that a threshold (TH) value separating both objects comprised in the ROI must be chosen for the quantification process. There is no standard method to determine the TH value. In this study a global TH value equal to 30 was used, considering a 0 to 256 gap. Thus, we could separate the pores (white) from the rock matrix (black). Then, the parameters where quantified directly in 3D based on a model of the rendered surface volume. All objects in the selected region were analyzed together and the integrated results were calculated as the total volume of all objects.

III. RESULTS AND DISCUSSIONS

The acquisitions generated data matrixes of 4224 x 4224 pixels and of 2240 x 2240 pixels for the 10 µm and 20 µm resolutions, respectively. Such matrix sizes have the disadvantage of being too difficult to be processed; especially by microCT once their files can reach a 34.7GB size (1200 images for each microCT test). Aiming to

 ISBN: 978-1-61208-214-1

improve the time for image processing the images passed through a resize process before they were quantified. This process allows reducing the size of an image and of a data set by the average of voxel gray levels in a cube of specified size. For example, resizing in a 2 factor opens a version of the data set with 8 times less voxels (2x2x2). This allows a very quick handling, geometric measuring and the construction of models of lower spatial resolution. In this study resizes of 2 and 4 were used.

Tables I-IV show the time for image processing obtained in each condition used. The quantifications showed in Tables III-IV were made based on the values of the matrixes presented in Tables I-II. These numbers take into consideration the entire volume of the holes, which are the objects of interest in this study.

TABLE I. MICROCT DIFFERENCE IN IMAGING ACQUISITION AND RECONSTRUCTION TIMES

Samples	**Acquisition Resolution**	**Acquisition**	**Reconstruction**
		Scan duration	***Duration per slice***
Sample 1	10 µm	02:02:40 h	2.0 s
	20 µm	00:59:12 h	0.4 s
Sample 2	10 µm	01:55:48 h	1.5 s
	20 µm	00:59:44 h	0.3 s

TABLE II. MICROCT DIFFERENCE IN IMAGING PROCESSING II

Samples	**Acquisition Resolution**	**Processing**		
		Original Matrix	***Quantified Matrix***	***Slice Numbers***
Sample 1	10 µm	4224 x 4224	(resize 2x) 625 x 625	145
	20 µm	2000 x 1932	(resize 3x) 614 x 614	143
Sample 2	10 µm	4224 x 4224	(resize 3x) 829 x 829	224
	20 µm	1356 x 1296	(resize 2x) 612 x 612	221

TABLE III. MICROCT RESULTS - SAMPLE 1

Parameters	**Resolutions**		
	20 µm (Original)	***Resize 2x***	***Resize 3x***
Matrix quantified (pixels)	2000X1932	625x625	614x614
Object binarised Volume (mm^3)	23.34	16.2	14.25
Percent object volume (%)	0.64	0.40	0.39
Total volume of pores (mm^3)	3623.2	3599.8	3613.5
Total porosity (%)	99.4	99.6	99.6

TABLE IV. MICROCT RESULTS - SAMPLE 2

Parameters	**Resolutions**		
	20 µm	***Resize***	***Resize***
	(Original)	***2x***	***3x***
Matrix quantified (pixels)	1356X1296	829x829	612x612
Object binarised Volume (mm^3)	27.59	36.50	27.19
Percent object volume (%)	1.91	2.50	1.86
Total volume of pores (mm^3)	1416.8	1423.2	1427.3
Total porosity (%)	98.1	97.5	98.1

As expected, this table shows that the higher the spatial resolution the higher the time required for the data to be obtained. However, when resize is used there is the need to consider the change in the pixel's size, which may impair the quantification of small structures. In this case, the size of the pixel is increased, making us 'see' only the structures from this new value, which leads us to analyze the cost/benefit of this procedure.

Tables III-IV show the results of the geometric quantifications for 20 µm resolutions in both samples with different pixel sizes obtained through the resize process and without resize. Being the real volumes of the holes 14.92 ±0.02 mm^3 in sample 1 and 33.75 ±0.02 mm^3 in sample 2 there is no significant difference in relation to the values quantified in the 3D analysis.

The difference of less than 1% in the results of the percentages of each parameter calculated in the 3D analysis, of each sample between resolutions, is noticeable. Thus, when necessary to characterize objects with the dimension of the holes assessed in this study, a microCT test in the quickest acquisition and image processing conditions can be used since losses in the data obtained wee not significant. Obviously, the smaller the size of the pixel the more detail can be visualized in the image, generating more precise and accurate quantitative results.

The tridimensional models built after the 3D analysis of the holes may be observed in Fig. 2 and Fig. 3.

 ISBN: 978-1-61208-214-1

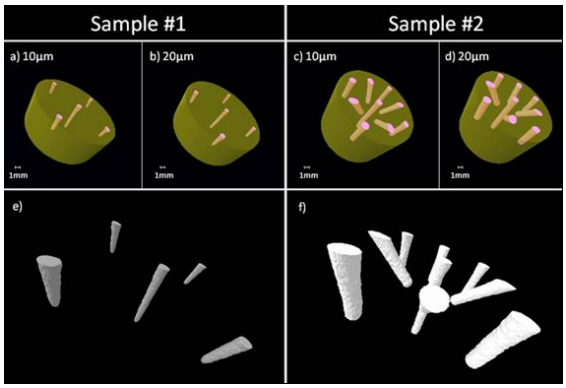

Figure 2. 3D models of sample 1 in the resolution of 10µm (a) and of 20µm (b) and of sample 2 in the resolution of 10µm (c) and of 20 µm (d). Better views of the holes for sample 1 (e) and sample 2 (f).

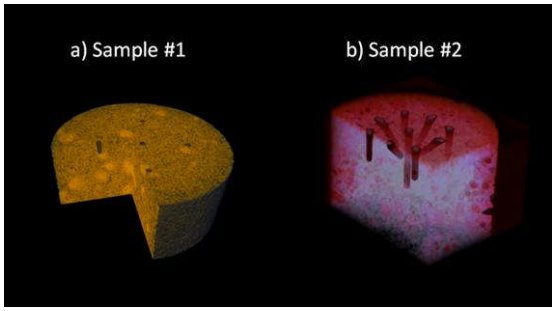

Figure 2. 3D models of sample 1 in the resolution of 20µm (a) and of sample 2 in the resolution of 20µm (b).

IV. CONCLUSION AND FUTURE WORK

The 3D Computed Microtomography technique is adequate for the characterization of reservoir rocks, supplying internal micro structural parameters that allow the petrophysical study of these materials. The differences presented in all stages (acquisition, reconstruction, processing and analysis) show that for a high resolution long acquisition and reconstruction periods are needed and processing is difficult, demanding the use of resize. This pixel size reduction tool proved to be very useful since it optimizes the analysis process not causing a significant loss of information. The next stages of this work is to analyze all the pore space of rocks, not only the created holes and further investigate the metrology associated with parameters related to the porosity space.

ACKNOWLEDGMENT

The authors would like to thanks CNPQ, FAPERJ and Petrobras/CENPES.

REFERENCES

[1] K. Remeysen and R. Swennen, “Application of Microfocus computed tomography in carbonate reservoir characterization: Possibilities and limitations”. Marine and Petroleum Geology, pp. 486-499, 2008.

[2] R. Ketcham and W Carlson, “Acquisition, optimization and interpretation of x-ray computed tomographic imagery: applications to the geosciences”. Computers & Geoscience, pp. 381-400, 2001.

[3] E. N. Lanis and D. T. Keane. “X-ray microtomography”. Materials Characterization., vol. 61, pp. 1305-1316, 2010.

[4] R. Muller, B. Koller, T. Hildebrand, A. Laib, S. Gianolini and P. Ruegsegger, “Resolution dependency of microstructural properties of cancellous bone based on three-dimensional mutomography”, Technol Health Care. vol. 4, pp. 113–119, 1996.

[5] D. G. Kim, G. T. Christopherson, X. N. Dong, D. P. Fyhrie, and Y. N. Yeni, “The effect of microcomputed tomography scanning and reconstruction voxel size on the accuracy of stereological measurements in human cancellous bone”. Bone, vol. 35, pp. 1375–1382, 2004.

[6] S.R. Stock, “Microcomputed tomography, methodology and applications”, CRC Press, 2008, pp. 145–170.

[7] M.F.S. Oliveira, I. Lima, P.L Ferrucio, C.J. Abreu, L. Borghi and R.T. Lopes, “Petrophysical analysis of limestone rocks by nuclear logging and 3D high-resolution X-ray computed microtomography”, Nuclear Instruments & Methods in Physics Research A, vol.652, pp. 905-910, 2011.

[8] NRecon, SkyScan/Bruker micro-CT, Kartuizerweg 3B 2550 Kontich, Belgium; 2011.

[9] InstaRecon,®, CBR Premium 12-8K™, InstaRecon, Champaign, IL, USA, 2011.

[10] L.A. Feldkamp, L.C. Davis, and J.W. Kress, “Practical cone beam algorithm”, J Opt Soc Am A, vol.1, pp. 612–619, 1984.

[11] CT Analyser, "The user's guide", Skyscan/Bruker micro-CT, Kartuizerweg 3B 2550 Kontich, Belgium, 2012.

 ISBN: 978-1-61208-214-1

An Analytical Study of Short-Channel Effects of Strained-Si on Silicon-Germanium-on-Insulator (SGOI) MOSFETs Including Interface Charges

Mirgender Kumar, Sarvesh Dubey, Satyabrata Jit
Department of Electronics Engineering
Indian Institute of Technology (BHU)
Varanasi, India
e-mails: mkumar.rs.ece@itbhu.ac.in,
sdubey.rs.ece@itbhu.ac.in, sjit.ece@itbhu.ac.in

Abirmoya Santra, Pramod Kumar Tiwari
Department of Electronics and Communication
Engineering, National Institute of Technology
Rourkela, India
e-mails: tiwarip@nitrkl.ac.in

***Abstract*—In this paper, an analytical threshold voltage model is developed for short-channel Strained-Si (s-Si) on Silicon-Germanium-on-insulator (SGOI) MOSFET including the effects of interface charges. The two-dimensional Poisson's equation is solved in the undamaged and damaged strained-Si and relaxed $Si_{1-x}Ge_x$ regions to find out the surface potential minimum for calculating the threshold voltage. The results obtained from the developed model have been compared with the numerical simulation results obtained using ATLAS™ from Silvaco. The extent of influence of hot carriers induced effects in terms of interface charges and damaged s-Si/front gate oxide interface on threshold voltage roll-off and drain induced barrier lowering (DIBL) have been studied.**

Keywords-strained-Si; SGOI; short-channel effects; inteface charges

I. INTRODUCTION

The use of strained silicon channel has become an unavoidable feature for sub 100nm regime CMOS technology, to maintain the expected performance improvements through scaling [1]. Among various proposed strained channel MOS structures, strained-Si on silicon-germanium-on-insulator (SGOI) MOSFET has received considerable attention because of providing more flexibility to control the strain in channel [2]. At such nanometer scaled devices, hot-carrier induced interface charges grievously affect the device performance, [3]. Besides this, downscaling of device also makes the short-channel effects (SCEs) severe [4]. It has been reported that the performance of the nanometer strained-Si devices is significantly dependent on the interface state charges near the Si/SiO_2 interface [5]. Thus, it becomes obligatory to investigate the depth up to which the interface charges can affect the short-channel device performance. A number of researchers have reported the study including interface charges for strained-Si SOI MOSFETs [3, 6]. Recently, a threshold voltage model is presented for strained-Si on SGOI MOSFETs [7]; however the effects of localized charges on short-channel effects are not investigated.

In this paper, a threshold voltage model is presented for strained-Si on SGOI MOSFETs including the effects of interface charges. Effects of the interface charges on the drain induced barrier lowering (DIBL) and threshold voltage roll-off are discussed. A uniform distribution of localized charges has been taken into consideration. In Section II, the device structure is briefed in terms of various device parameters. Section III deals with the modeling approach carried out while deriving the surface potential and threshold voltage of the device. All the theoretical results have been compared with the 2D simulation results, obtained by ATLAS™ 2D device simulator [8], and discussed in Section IV. The paper has been concluded in Section V.

II. DEVICE STRUCTURE

Fig. 1 shows the schematic cross sectional view of the strained-Si on SGOI MOSFET structure with induced localized charges. A layer of Si is grown pseudomorphically on the relaxed $Si_{1-x}Ge_x$ layer, where x is the Ge mole fraction, which causes the strain in the Si layer due to lattice mismatching with $Si_{1-x}Ge_x$.

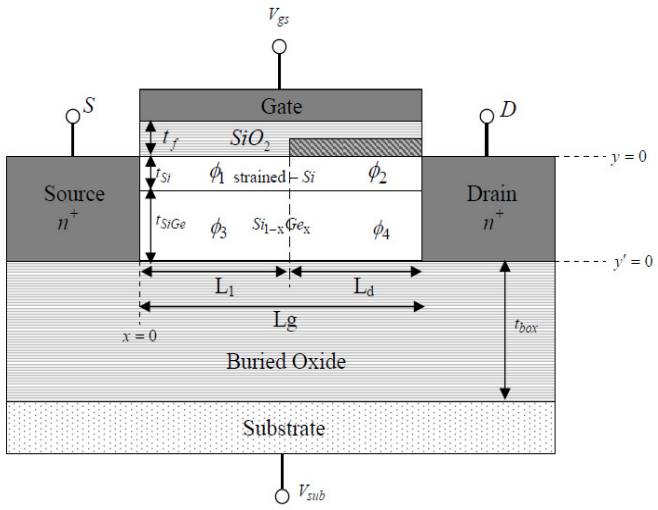

Figure 1. Cross sectional view of Strained-Si on SGOI MOSFET

L_d and L_1 are damaged and undamaged region lengths, respectively, along the channel connected in a non-overlapping way. The interface charge density in the damaged oxide region is assumed to be $N_I\,\mathrm{cm}^{-2}$. The

symbols t_{Si} , t_f , t_{box} and t_{SiGe} represent the thicknesses of the strained-Si, front gate oxide, buried oxide and $Si_{1-x}Ge_x$ layers, respectively.

III. MODELING APPROACH

Fig. 2 displays the change in silicon energy band structure because of strain in the silicon channel. The device simulator model library of ATLAS™, thus, has been modified according to the effects of strain on Si band structure [9].

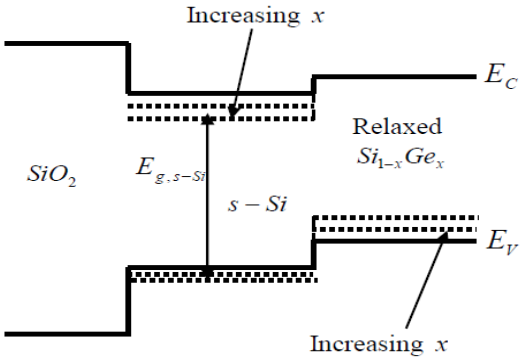

Figure 2. Effect of strain on band structure of Silicon

A. Surface Potential Formulation

First, To find out the potential distribution ($\phi(x,y)$) in the channel region, the 2D Poisson's equations has been solved in all the four regions of strained-Si and relaxed $Si_{1-x}Ge_x$ layers as shown in Fig. 1. The equations are

$$\frac{\partial^2\phi_{i,j}(x,y)}{\partial x^2}+\frac{\partial^2\phi_{i,j}(x,y)}{\partial y^2}=\frac{qN_A}{\varepsilon_{Si,SiGe}} \quad (1)$$

For $Si_{1-x}Ge_x$ layer, y -coordinate should be considered as y' . Subscripts denote the channel region as i stands for 1 and 2 whereas j stands for 3 and 4; N_A is the body doping concentration; q is the electronic charge; ε_{Si} and ε_{SiGe} are the permittivity of strained-Si film and relaxed $Si_{1-x}Ge_x$. The potential distributions in all the four regions are approximated by parabolic approximation [10] as

$$\phi_i(x,y)=\phi_{si}(x)+C_{i1}(x)y+C_{i2}(x)y^2 \quad (2)$$

$$\phi_j(x,y')=\phi_{bj}(x)+C_{j1}(x)y'+C_{j2}(x)y'^2 \quad (3)$$

Here, the coefficients $C_{i(j)1,2(3,4)}$ are the functions of x only; ϕ_{si} is the surface potential at SiO_2/s-Si interface for both damaged and undamaged regions, ϕ_{bj} is potential along buried-SiO_2/$Si_{1-x}Ge_x$ interface for both damaged and undamaged regions. The continuity of potential and electric field across the interface of undamaged and damaged regions are [6]:

$$\phi_1(L_1,0)=\phi_2(L_1,0) \quad (4)$$

$$\left[\frac{\partial\phi_1(x,y)}{\partial x}\right]_{x=L_1}=\left[\frac{\partial\phi_2(x,y)}{\partial x}\right]_{x=L_1} \quad (5)$$

$$\phi_3(L_1,0)=\phi_4(L_1,0) \quad (6)$$

$$\left[\frac{\partial\phi_3(x,y')}{\partial x}\right]_{x=L_1}=\left[\frac{\partial\phi_4(x,y')}{\partial x}\right]_{x=L_1} \quad (7)$$

Electric flux at SiO_2/s-Si interface should be continuous in the undamaged and damaged regions [7]:

$$\left[\frac{\partial\phi_1(x,y)}{\partial y}\right]_{y=0}=\frac{\varepsilon_f}{\varepsilon_{Si}}\frac{\phi_{s1}(x)-V'_{gs}}{t_f} \quad (8)$$

$$\left[\frac{\partial\phi_2(x,y)}{\partial y}\right]_{y=0}=\frac{\varepsilon_f}{\varepsilon_{Si}}\frac{\phi_{s2}(x)-V''_{gs}}{t_f} \quad (9)$$

where, ε_f is the permittivity of the SiO_2, t_f is the thickness of front gate oxide; $V'_{gs}=V_{gs}-(V_{FB,f})_{s-Si}$ with V_{gs} as the gate to source voltage, $(V_{FB,f})_{s-Si}$ is the front channel flat-band voltage of strained-Si film and $V''_{gs}=V_{gs}-(V_{FB,f})_{s-Si}+qN_I/C_f$.

Electric flux at $Si_{1-x}Ge_x$/buried oxide interface is continuous, we may write [7];

$$\left[\frac{\partial\phi_3(x,y')}{\partial y'}\right]_{y'=0}=\frac{\varepsilon_{box}}{\varepsilon_{SiGe}}\frac{\phi_{b3}(x)-V'_{sub}}{t_{box}} \quad (10)$$

$$\left[\frac{\partial\phi_4(x,y')}{\partial y'}\right]_{y'=0}=\frac{\varepsilon_{box}}{\varepsilon_{SiGe}}\frac{\phi_{b4}(x)-V'_{sub}}{t_{box}} \quad (11)$$

where $V'_{sub}=V_{sub}-(\Phi_{sub}-\Phi_{SiGe})$, V_{sub} being the substrate voltage and t_{box} is the buried oxide thickness; Φ_{SiGe} is the work-function of relaxed $Si_{1-x}Ge_x$ layer; Φ_{sub} is the work-function of the silicon substrate under buried oxide.

The potential and electric field at the Si/$Si_{1-x}Ge_x$ interface should be continuous as [6];

$$\phi_1(x,t_{Si})=\phi_3(x,t_{SiGe}) \quad (12)$$

$$\left[\frac{\partial\phi_1(x,y)}{\partial y}\right]_{y=t_{Si}}=-\frac{\varepsilon_{SiGe}}{\varepsilon_{Si}}\left[\frac{\partial\phi_3(x,y')}{\partial y'}\right]_{y'=t_{SiGe}} \quad (13)$$

$$\phi_2(x,t_{Si})=\phi_4(x,t_{SiGe}) \quad (14)$$

$$\left[\frac{\partial\phi_2(x,y)}{\partial y}\right]_{y=t_{Si}}=-\frac{\varepsilon_{SiGe}}{\varepsilon_{Si}}\left[\frac{\partial\phi_4(x,y')}{\partial y'}\right]_{y'=t_{SiGe}} \quad (15)$$

The potentials at the source and drain end can be given by [7];

$$\phi_1(0,0)=V_{bi,s-Si} \quad (16)$$

$$\phi_3(0,0)=V_{bi,SiGe} \quad (17)$$

$$\phi_2(L,0)=V_{bi,s-Si}+V_{ds} \quad (18)$$

$$\phi_4(L,0)=V_{bi,SiGe}+V_{ds} \quad (19)$$

where, $V_{bi,s-Si}$ is the built-in voltage for strained-Si and $V_{bi,SiGe}$ is the built-in voltage for $Si_{1-x}Ge_x$; V_{ds} is drain-to-source voltage.

With the help of the boundary conditions described by (5)-(19), the final expression of surface potential can be written as [10];

$$\phi_{s1} = A_1 \exp(\lambda x) + B_1 \exp(-\lambda x) - \sigma_1 \quad (20)$$

$$\phi_{s2} = A_2 \exp(\lambda(x - L_1)) + B_2 \exp(-\lambda(x - L_1)) - \sigma_2 \quad (21)$$

where,

$$B_1 = \frac{(V_{bi,s-Si} - \sigma_1)(\exp(\lambda L) - 1) - (\sigma_2 - \sigma_1)(1 - \cosh(\lambda L_d)) - V_{ds}}{2\sinh(\lambda L)}$$

$$A_1 = V_{bi,s-Si} + \sigma_1 - B_1$$

$$A_2 = A_1 \exp(\lambda L_1) + (\sigma_2 - \sigma_1)/2$$

$$B_2 = B_1 \exp(-\lambda L_1) + (\sigma_2 - \sigma_1)/2$$

λ, σ_1 and σ_2 are the constants obtained from the boundary conditions mentioned above.

The position $(x_{1(2),\min})$ of the minimum surface potential for both negative and positive interface charges under the undamaged and damaged regions respectively can be determined by solving $\left.\frac{d\phi_{s1(2)}}{dx}\right|_{x=x_{1(2),\min}} = 0$ [6] and hence be given as;

$x_{1,\min} = \ln(B_1/A_1)/2\lambda$ and

$x_{2,\min} = L_1 + \ln(B_2/A_2)/2\lambda$

By substituting the values of the minima position into (20) and (21), the minimum surface potentials can be expressed

$$\phi_{s1,\min} = 2\sqrt{A_1 B_1} - \sigma_1 \quad (22)$$

$$\phi_{s2,\min} = 2\sqrt{A_2 B_2}\cosh(\lambda L_1) - \sigma_2 \quad (23)$$

B. Threshold Voltage Formulation

The Because of the coexistence of the damaged and the undamaged regions in our device structure, the minimum surface potential of device is determined by the magnitude and polarity of the charge present in the damaged region. Thus, depending on the polarity of interface charges, threshold voltage, say $V_{th+(-)}$, for positive (negative) type of interface charges can be found as follows as [7]:

$$\left.\phi_{s1(2),\min}\right|_{Vgs=V_{th}+(-)} = 2\Phi_{F,Si} + \Delta\Phi_{s-Si} = \Phi_{th} \quad (24)$$

where, $\Phi_{F,Si}$ is the difference between the Fermi potential and the intrinsic Fermi level in the bulk region, $\Delta\Phi_{s-Si}$ is the change in the work-function of silicon due to strain, Φ_{th} is the value of surface potential at which the volumetric inversion electron charge density in the strained-Si device is the same as that in the unstrained-Si at threshold, i.e., equal to the body doping.

Solving (24), we obtain the final expression of threshold voltages as

$$V_{th+(-)} = \frac{-\eta_{1(2)} + \sqrt{\eta_{1(2)}^2 - 4\rho\xi}_{1(2)}}{2\rho} \quad (25)$$

where,

$$\rho = N^2\left[2(\cosh(\lambda L) - 1) - \sinh^2(\lambda L)\right]$$

$$\eta_1 = N\left[2(\Phi_{th} + M_1)\sinh^2(\lambda L) - R_1(\exp(\lambda L) - 1) - S_1(1 - \exp(\lambda L))\right]$$

$$\xi_1 = R_1 S_1 - (\Phi_{th} + M_1)^2 \sinh^2(\lambda L)$$

$$R_1 = (V_{bi,s-Si} + M_1)(1 - \exp(-\lambda L)) + V_{ds} + (\sigma_2 - \sigma_1)(1 - \cosh(\lambda L_d))$$

$$S_1 = (V_{bi,s-Si} + M_1)(\exp(-\lambda L) - 1) - V_{ds} - (\sigma_2 - \sigma_1)(1 - \cosh(\lambda L_d))$$

$$u_2 = \frac{qN_A}{\varepsilon_{Si}} + \frac{C_{box}V'_{sub}}{(C_{Si} + C_{SiGe})t_{Si}^2} + \frac{C_f(2C_{SiGe} + C_{Si})\left((V_{FB,f})_{s-Si} + (qN_I/C_f)\right)}{C_{Si}(C_{Si} + C_{SiGe})t_{Si}^2}$$

$$\nu_1 = \frac{C_f(2C_{SiGe} + C_{Si})}{C_{Si}(C_{Si} + C_{SiGe})t_{Si}^2}$$

$$u_1 = \frac{qN_A}{\varepsilon_{Si}} + \frac{C_{box}V'_{sub}}{(C_{Si} + C_{SiGe})t_{Si}^2} + \frac{C_f(2C_{SiGe} + C_{Si})(V_{FB,f})_{s-Si}}{C_{Si}(C_{Si} + C_{SiGe})t_{Si}^2}$$

$$u_3 = \frac{qN_A}{\varepsilon_{SiGe}} + \frac{C_{box}(C_{SiGe} + 2C_{s-Si})V'_{sub}}{C_{SiGe}(C_{Si} + C_{SiGe})t_{SiGe}^2} + \frac{C_f(V_{FB,f})_{s-Si}}{(C_{Si} + C_{SiGe})t_{SiGe}^2}$$

$$u_4 = \frac{qN_A}{\varepsilon_{SiGe}} + \frac{C_{box}(C_{SiGe} + 2C_{Si})V'_{sub}}{C_{SiGe}(C_{Si} + C_{SiGe})t_{SiGe}^2} + \frac{C_f\left((V_{FB,f})_{s-Si} + (qN_I/C_f)\right)}{(C_{Si} + C_{SiGe})t_{SiGe}^2}$$

$$\nu_2 = \frac{C_{ox}}{(C_{SiGe} + C_{Si})t_{SiGe}^2}$$

$$\sigma = \frac{\beta_1(u_4 - u_3) - \alpha_2(u_2 - u_1)}{\alpha_1\alpha_2 - \beta_1\beta_2}$$

$$\eta_2 = N\left[\begin{array}{r} 2(\Phi_{th} + M_2)\sinh^2(\lambda L) - R_2(\exp(\lambda L_d) - \exp(-\lambda L_1)) \\ - S_2(\exp(\lambda L_1) - \exp(-\lambda L_d)) \end{array}\right]$$

$$\xi_2 = R_2 S_2 - (\Phi_{th} + M_2)^2 \sinh^2(\lambda L)$$

$$R_2 = \left[\begin{array}{r} (V_{bi,s-Si} + M_1)(\exp(\lambda L_1) - \exp(-\lambda L_d)) + V_{DS}\exp(\lambda L_1) \\ + (\sigma_2 - \sigma_1)(\exp(\lambda L_1) - \cosh(\lambda L_1)\exp(-\lambda L_d)) \end{array}\right]$$

$$S_2 = \left[\begin{array}{r} (V_{bi,s-Si} + M_1)(\exp(\lambda L_d) - \exp(-\lambda L_1)) - V_{DS}\exp(-\lambda L_1) \\ - (\sigma_2 - \sigma_1)(\exp(-\lambda L_1) - \cosh(\lambda L_1)\exp(\lambda L_d)) \end{array}\right]$$

$C_f = \frac{\varepsilon_f}{t_f}$, $C_{Si} = \frac{\varepsilon_{Si}}{t_{Si}}$, $C_{SiGe} = \frac{\varepsilon_{SiGe}}{t_{SiGe}}$ and $C_{box} = \frac{\varepsilon_{box}}{t_{box}}$ are front gate oxide, strained-Si, relaxed $Si_{1-x}Ge_x$ layer and buried oxide capacitances respectively and M, M_1 and N are constants. It may be pointed out that the threshold voltage of strained-Si SGOI MOSFETs significantly depends on the polarity of the interface charge density.

 ISBN: 978-1-61208-214-1

IV. RESULTS AND DISCUSSION

This section contains the comparison between the analytical results obtained from our proposed model with the numerical simulation data extracted from simulating the device structure under consideration with a commercially available 2D device simulator ATLAS™ [8]. The threshold voltage is extracted from the ATLAS simulation by maximum transconductance method. Fig. 3 shows the variation of threshold voltage roll-off with positive and negative interface charge densities for different damaged region length, L_d. It is found that threshold voltage roll-off increases for both positive and negative interface charge densities but rate of increment is higher for negative charge density. However, the nature of variation is different in both of the cases. In the case of positive interface charge density, there is an increase in threshold voltage roll-off with L_d whereas for negative interface charges, roll-off decreases with L_d. Fig. 4 discusses the impact of drain voltage on device characteristics in terms of drain induced barrier lowering (DIBL) variation with respect to interface charge density. It can be observed that that DIBL increases very sharply with increasing negative interface charge density but very slightly decreases with positive interface charge density.

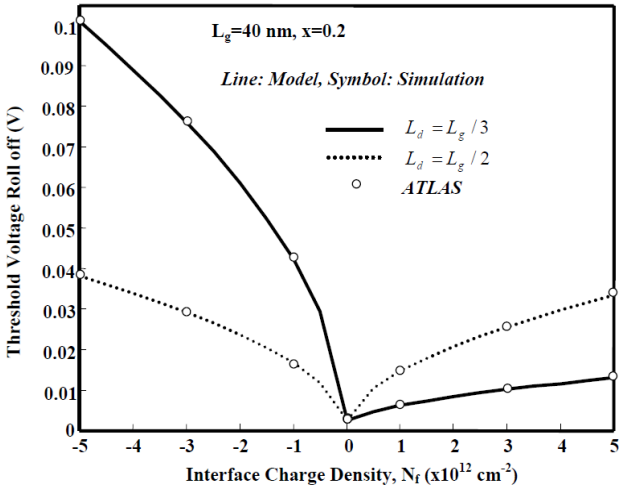

Figure 3. Threshold voltage roll-off versus interface charge density of strained-Si on SGOI MOSFET for different damaged length

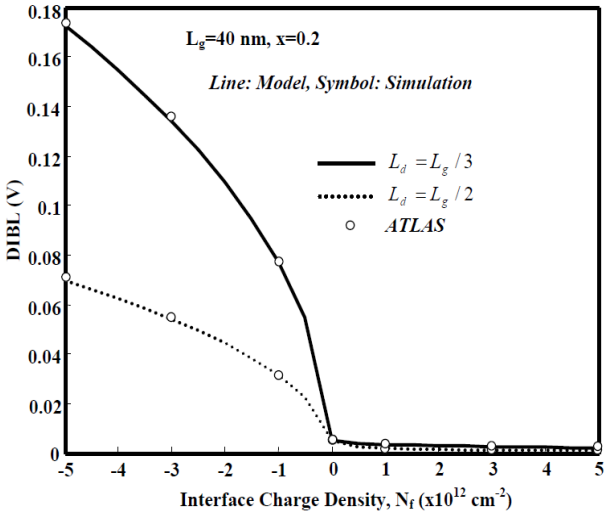

Figure 4. DIBL versus interface charge density of strained-Si on SGOI MOSFET for different damaged length with $V_{ds} = 0.1$V and 1V

DIBL is large for smaller damaged length for negative interface charge density. Finally, Fig. 5 compositely illustrates the effect of damaged region length on threshold voltage roll-off and DIBL for different Ge mole fraction (x). It is observed that larger x, which also corresponds to the higher strain in the channel region, suppresses the threshold voltage roll-off and drain induced barrier lowering effectively. However, with respect to the length of damaged region, the trend of variation becomes reverse i.e., the threshold voltage roll-off decreases whereas DLBL increases with the increases in L_d.

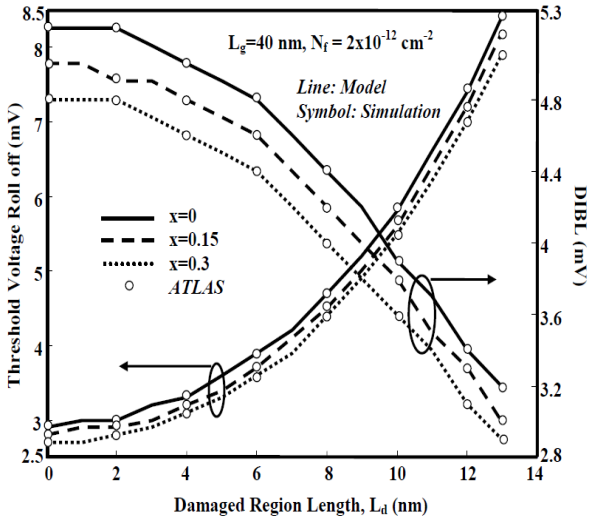

Figure 5. DIBL and Threshold Voltage Roll-off versus damaged region length of strained-Si on SGOI MOSFET for different Ge mole fraction (x) in SiGe layer on a fixed positive interface charge density

 ISBN: 978-1-61208-214-1

V. CONCLUSION

An analytical threshold voltage model is derived including the effect both positive and negative interface charges. It is observed that the negative interface charge density has more severe effect than the positive interface charge density on the DIBL and threshold voltage roll-off of the strained-Si on SGOI MOSFETs. However, it is found that strain in the silicon channel suppresses short-channel effects. The proposed model results are in good agreement with the numerical simulation results.

REFERENCES

[1] M. L. Lee, E. A. Fitzgerald, M. T. Bulsara, M. T. Currie, and A. Lochtefeld, "Strained Si, SiGe, and Ge channels for high-mobility metal-oxide semiconductor field-effect transistors," J. Appl. Phys., vol. 97, 011101 (2005), pp. 1-27.

[2] F. Gamiz, P. C. Cassinello, J. B. Roldan, and F. J. Molinos, "Electron transport in strained Si inversion layers grown on SiGe-on-insulator substrates," J. Appl. Phys., vol. 92, no. 1, Jul. 2002, pp. 288–295.

[3] Y. Leblebici and S-M Kang, "Modeling of nMOS Transistors for Simulation of Hot-Carrier-Induced Device and Circuit Degradation," IEEE Trans. Computer-Aided Design, vol. 11 , no. 2, February 1992, pp. 235-246.

[4] A. Chaudhry and M. Jagadesh Kumar, Controlling Short-Channel Effects in Deep-Submicron SOI MOSFETs for Improved Reliability: A Review, IEEE Transactions on Device and Materials Reliability, vol. 4, 2004, pp. 99-109.

[5] P. S. Jack, J.-Y. Kuo, "On the Enhanced Impact Ionization in Uniaxial Strained p-MOSFETs," IEEE Electron Dev. Lett, vol. 28, no. 7, 2007, pp. 649-52.

[6] Eleftherios G. Ioannidis, Andreas Tsormpatzoglou, Dimitrios H. Tassis, Effect of Localized Interface Charge on the Threshold Voltage of Short-Channel Undoped Symmetrical Double-Gate MOSFETs, IEEE Trans. Electron Devices, vol. 58, no. 2, Feb 2011, pp. 433-440.

[7] V. Venkataraman, S. Nawal, and M. J. Kumar, "Compact Analytical Threshold-Voltage Model of Nanoscale Fully Depleted Strained-Si on Silicon–Germanium-on-Insulator (SGOI) MOSFETs," IEEE Trans. Electron Devices, vol. 54, no. 3, March 2007, pp. 554-562.

[8] ATLAS Users Manual, Silvaco International, Santa Clara, CA, 2000.

[9] Numata, T., Mizuno, T., Tezuka, T., Koga, J., Takagi, S.: Control of threshold-voltage and short-channel effects in ultrathin strained-SOI CMOS devices. IEEE Trans. Electron Devices, Vol. 52, 2005, pp. 1780–1786.

[10] K. K. Young, Short-channel effect in fully depleted SOI MOSFETs IEEE Trans. Electron Devices, Vol. 36, 1989, pp. 399–402.

 ISBN: 978-1-61208-214-1